SPIN POLARIZED CURRENT PHENOMENA IN MAGNETIC TUNNEL JUNCTIONS

A DISSERTATION

SUBMITTED TO THE DEPARTMENT OF APPLIED PHYSICS

AND THE COMMITTEE ON GRADUATE STUDIES

OF STANFORD UNIVERSITY

IN PARTIAL FULFILLMENT OF THE REQUIREMENTS

FOR THE DEGREE OF

DOCTOR OF PHILOSOPHY

Li Gao

September 2009

I certify that I have read this dissertation and that, in my opinion, it is fully adequate in scope and quality as a dissertation for the degree of Doctor of Philosophy.

_____

(James S. Harris) Principal Advisor

I certify that I have read this dissertation and that, in my opinion, it is fully adequate in scope and quality as a dissertation for the degree of Doctor of Philosophy.

_____

(Stuart S. P. Parkin) co-Principal Advisor

I certify that I have read this dissertation and that, in my opinion, it is fully adequate in scope and quality as a dissertation for the degree of Doctor of Philosophy.

_____

(Walter A. Harrison)

Approved for the University Committee On Graduate Studies.

_____

Abstract

Spin polarized current is of significant importance both scientifically and technologically. Recent advances in film growth and device fabrication in spintronics make possible an entirely new class of spin-based devices. An indispensable element in all these devices is the magnetic tunnel junction (MTJ) which has two ferromagnetic electrodes separated by an insulator barrier of atomic scale. When electrons flow through a MTJ, they become spin-polarized by the first magnetic electrode. Thereafter, the interplay between the spin polarized current and the second magnetic layer manifests itself via two phenomena:

i.) Tunneling magnetoresistance (TMR) effect. The relative alignment of the electrode moments determines the resistance and its change. This TMR effect is largely determined by the spin polarized density states of the electrodes, interface states, tunneling matrix, and so on. However, despite extensive experimental and theoretical efforts, many aspects of TMR remain poorly understood. In my research, it is shown that thin CoFe alloy can be made amorphous by sandwiching the normally crystalline CoFe electrode between two amorphous layers. Incorporating amorphous CoFe with Al_2O_3 to form MTJs, both the TMR and the tunneling spin polarization are significantly enhanced when the alloy is amorphous. The tunneling anisotropic magnetoresistance effect in both MgO and Al_2O_3 based MTJs is also investigated.

ii.) Spin transfer torque (STT) effect. The spin polarized current exerts a torque on the local moments and can thereby induce steady-state precessional excitation modes or complete switching of a nanomagnet. This effect has mostly been studied, to date, in metallic structures where the spin-valve magnetoresistance is small so that the output power is limited. However, the giant TMR effect in MgO based MTJs, which also have much higher resistance than spin-valves, can give rise to much higher rf power output. It is also found that the spectrum is very sensitive to small variations in device structures, even among devices which exhibit similarly high TMR (~120%) and have similar resistance-area product (~4-10 $\Omega\mu m^2$).

Acknowledgements

First of all, I am deeply grateful for Stuart Parkin's supervision and support of my Ph.D. work at the IBM Almaden Research Center. What I learned from him is far beyond knowledge and skills, and I am greatly impressed by his intelligence, passion, and innovation. I also really appreciate lots of help from him in my personal life. An excellent physicist, a great man, I luckily worked with in one important phase of my life.

I would like to sincerely thank Coach for admitting me to Harris group, and introducing me to the exciting field of spintronics. I especially appreciate his generous support at the beginning of my studies at Stanford. I thank Coach for his kind and persistent encouragement and help throughout all my Ph.D. years.

Special acknowledgements to Xin Jiang, without him many of my achievements are impossible. Thanks to other members of Parkin group for various help, I am honored of working with them: Masamitsu Hayashi, Rai Moriya, See-Hun Yang, Brian Hughes, Mahesh Samant, Kevin Roche, Luc Thomas, Hyunsoo Yang, Christian Kaiser, Nagaphani Aetukuri, Justin Brockman, Cheng-Han Yang, Guenole Jan, Andreas Ney, Ruisheng Liu, Bastiaan Bergman, Roger Wang, Rekha Rajaram, and Joanna Lankester. I thank Jonathan Sun for many stimulating discussions.

I acknowledge the help of Andrew Kellock for many RBS results, Philip Rice, Teya Topuria, and Leslie Krupp for TEM images, Dolores Miller for XPS measurements, and Charles Rettner for ebeam lithography.

I appreciate all the theoretical discussions with Dr. Don Nicholson, Prof. Evgeny Tsymbal, Dr. John Burton, Prof. Walter Harrison, Prof. William Butler, Dr. Mairbek Chshiev, and thank them for their calculations on my experimental results.

I also thank Prof. Walter Harrison for his willingness to be my reading committee member, Prof. David Goldhaber-Gordon for chairing my oral defense, and Prof. Ian Fisher for serving as an examiner.

All the administrative supports from Paula Perron, Gail Chun-Creech, Yvonne Paxton, and Claire Nicholas are invaluable. Many thanks are also extended to all the members in Harris group.

Finally, I would like to thank my parents, my wife, my parents-in-law, and my sister's family for years of support and encouragement. I am greatly indebted to them.

Table of Contents

List of Figures

Chapter 1

INTRODUCTION: SPIN POLARIZED CURRENT AND SPINTRONICS

As well as mass and charge, an electron has another intrinsic property, i.e. spin angular momentum, or simply spin. In quantum mechanics, spin is a fundamental property of atomic nuclei and elementary particles, and is an important intrinsic degree of freedom. Although as the name indicates spin was originally thought of particles spinning around their own axis, it had been shown by Dirac that electron spin arises naturally within relativistic quantum mechanics. The component of electron spin measured along any direction can only take on the values,

$$\hbar s_z, \quad s_z = \pm 1/2$$

Namely, in a classical picture, electron spin can only point to up or down along a magnetic field which can be vividly illustrated by a small magnet with its north pole pointing to up or down as shown in Fig. 1.1. The intrinsic magnetic dipole moment associated with such a spin in an electron is very close to a universal constant called the Bohr magneton, $\mu_B = \frac{e\hbar}{2m_e} = 0.927\times10^{-23}\left(J/T \text{ or } A\cdot m^2\right) = 0.927\times10^{-20}\left(erg/Oe\right)$.

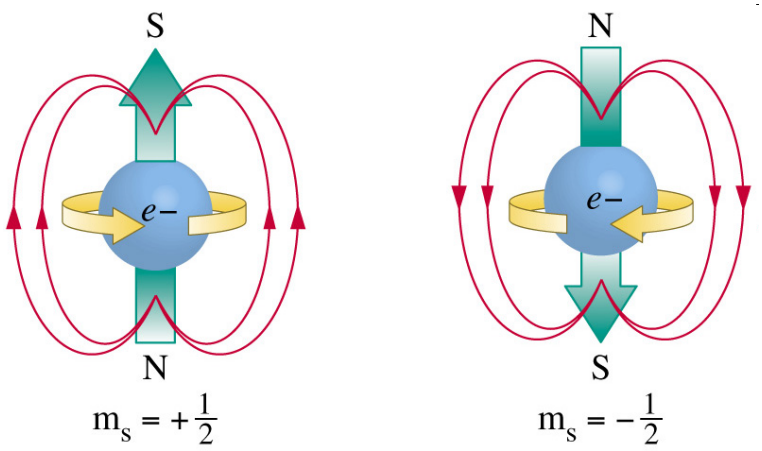

Fig. 1.1 Classical illustration of electron spin as a small magnet with north pole pointing to up or down.

In normal materials, such as Cu, Ag, etc., spin-up and -down electrons are equally populated and randomly distributed in an equilibrium state. However, in some solids due to the quantum mechanical exchange interaction, electron spins are aligned spontaneously, resulting in unequal numbers of spin-up and -down electrons, therefore ferromagnetic materials are formed, such as Co, Fe, Ni, and many of their alloys. In these ferromagnetic materials, spin-resolved electronic structures show the band

difference between the spin-up and -down electrons, as illustrated in Fig. 1.2, and the asymmetry in density of states (DOS) at Fermi energy gives rise to most of the spin related transport phenomena. When an unpolarized flow of electrons pass through a normal metal, because of the identity between the bands for spin-up and -down electrons, they experience the same scattering rate regardless of the spin, and the emergent current still remains unpolarized. However, when they flow through a ferromagnetic material, spin-up electrons may encounter less scattering, or may have smaller effective mass, compared to spin-down electrons, so the conductivity due to the majority spin channel would be higher. Then, a spin polarized current would emerge from the ferromagnetic material[1].

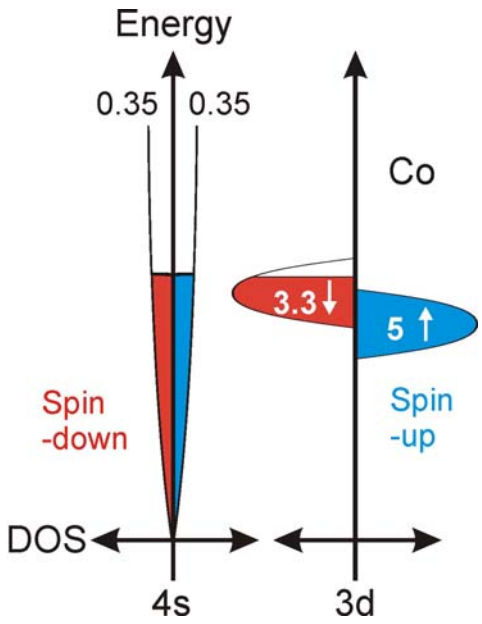

Fig. 1.2 Diagram of the spin-resolved electronic structures for 4s and 3d bands in Co. Red (or blue) is for spin-down (or spin-up). Numbers denote how many electrons per Co atom are in the corresponding band.

Such a spin polarized current is of significant importance both scientifically and technologically because it can be manipulated either via electron charge or spin, instead of electron charge only in conventional electronics[2]. Since the discovery of the giant magnetoresistance (GMR) effect in 1980's[3-5], spin-electronics (spintronics) using electron spin to control the current, has stimulated great interest in both the academic and industrial fields. Astonishing achievements have been obtained, especially in data storage applications. A few years later, due to the advances in the thin film growth and

device fabrication, an even more significant effect, called the tunneling magnetoresistance (TMR) effect, was observed at room temperature in magnetic tunneling junctions (MTJs)[6-9]. Because of their huge TMR and high resistance, MTJs promise attractive applications in magnetic field sensor and magnetic random access memory (MRAM) in very small scale of solid-state circuitry[2]. Read heads with MTJs in hard disk are commercially available, and there are many ongoing efforts to realize MRAM. This new type of memory has all the key desirable attributes required by the ever growing demand for storing and processing the explosive amount of information, such as fast access times, non-volatility, lower power-consumption, and high density. Moreover, from the perspective of physics, the quantum mechanical tunneling process in MTJs is not only very interesting but also extremely complicated, and many issues about it remain poorly understood[10].

The focus of the research in this dissertation is to deepen the understanding of the spin dependent tunneling effect in MTJs. A brief background in MTJs is provided in Chapter 2. It is first shown in Chapter 3 that the normally crystalline CoFe can be made amorphous when sandwiched between two amorphous layers, and when this amorphous CoFe is incorporated as an electrode in MTJs it gives rise to an enhanced TMR compared to its crystalline counterpart. The tunneling anisotropic magnetoresistance (TAMR) effect is investigated in conventional MTJs in Chapter 4, and it is found that the angular dependence of the TAMR effect shows complex two-fold and four-fold symmetry evolution with bias voltage. Chapter 5 is devoted to the studies of the current induced switching and microwave emission from MTJs due to the spin transfer torque effect. Chapter 6 provides a summary of the dissertation and some suggestions for future research.

REFERENCES:

[1] R. C. O'Handley, "Modern Magnetic Materials: Principles and Applications," (John Wiley & Sons, 2000).

[2] S. Parkin, X. Jiang, C. Kaiser, A. Panchula, K. Roche, and M. Samant, "Magnetically Engineered Spintronic Sensors and Memory," Proc. IEEE **91**, 661 (2003).

[3] M. N. Baibich, J. M. Broto, A. Fert, F. N. Van Dau, F. Petroff, P. Etienne, G. Creuzet, A. Friederich, and J. Chazelas, "Giant Magnetoresistance of (001)Fe/(001)Cr Magnetic Superlattices," Phys. Rev. Lett. **61** (21), 2472 (1988).

[4] G. Binasch, P. Grunberg, F. Saurenbach, and W. Zinn, "Enhanced magnetoresistance in layered magnetic structures with antiferromagnetic interlayer exchange," Phys. Rev. B **39** (7), 4828 (1989).

[5] S. S. P. Parkin, N. More, and K. P. Roche, "Oscillations in exchange coupling and magnetoresistance in metallic superlattice structures: Co/Ru, Co/Cr, and Fe/Cr," Phys. Rev. Lett. **64** (19), 2304 (1990).

[6] M. Julliere, "Tunneling between ferromagnetic films," Phys. Lett. A **54**, 225 (1975).

[7] J. S. Moodera, L. R. Kinder, T. M. Wong, and R. Meservey, "Large Magnetoresistance at Room Temperature in Ferromagnetic Thin Film Tunnel Junctions," Phys. Rev. Lett. **74**, 3273 (1995).

[8] S. S. P. Parkin, C. Kaiser, A. F. Panchula, P. Rice, M. G. Samant, S.-H. Yang, and B. Hughes, "Giant tunneling magnetoresistance at room temperature with MgO (100) tunnel barriers," Nature Materials **3**, 862 (2004).

[9] S. Yuasa, T. Nagahama, A. Fukushima, Y. Suzuki, and K. Ando, "Giant room-temperature magnetoresistance in single-crystal Fe/MgO/Fe magnetic tunnel junctions," Nature Materials **3**, 868 (2004).

[10] E. Y. Tsymbal, O. N. Mryasov, and P. R. LeClair, "Spin-dependent tunnelling in magnetic tunnel junctions," J. Phys. C: Condens. Matter **15**, R109 (2003).

Chapter 2

EXPERIMENTAL BACKGROUND

2.1 SPIN POLARIZED CURRENT IN MAGNETIC TUNNEL JUNCTIONS

Magnetic tunnel junctions (MTJs) are sandwiched heterostructures, composed of two ferromagnetic electrodes and an ultrathin insulator barrier in between, and present many interesting phenomena that are important for both the exploration of underlying physics and the applications in technology[1]. When electrons flow through a MTJ, they become spin-polarized by the first magnetic electrode. Thereafter, the interplay between the spin-polarized current and the second magnetic layer manifests itself via two effects, i.e. tunneling magnetoresistance effect and spin transfer torque effect. In the current section of this chapter, brief reviews will be given on these two interesting effects.

2.1.1 Tunneling Magnetoresistance

The resistance of a MTJ depends on the relative alignment of the magnetic moments in the ferromagnetic electrodes. Usually, when the moments are parallel the tunneling resistance is low; when anti-parallel, the resistance is high, thus giving rise to a tunneling magnetoresistance (TMR) effect,

$$TMR = \frac{R_{AP} - R_P}{R_P} \times 100\% ,$$

where R_{AP} and R_P are the resistances for the parallel and anti-parallel configurations. A typical magnetoresistance loop (Fig. 2.1) shows that, by cleverly engineering the multilayered structure, e.g. growing an antiferromagnetic material as an exchange bias layer, it is possible to control how the two magnetic electrodes respond to the external field and therefore to obtain distinct states of different resistance values[1]. The first successful observation of TMR in MTJs was made by Jullière about thirty years ago, when Co and Fe were used as electrodes and Ge as insulator and a TMR of ~14% at 4.2 K was reported[2]. After that many other tunnel barriers were explored (e.g. NiO and Gd_2O_3)[3,4], but only a small effect was observed even at a low temperature. It was not until 1995 when the first observation of reproducible large TMR (~18%) at room temperature was achieved in MTJs with an amorphous Al_2O_3 barrier[5,6]. Ever since

then, MTJs have aroused considerable interest due to their potential applications in spintronic devices, such as high-performance solid-state magnetic random access memories (MRAM) and magnetic sensors[1].

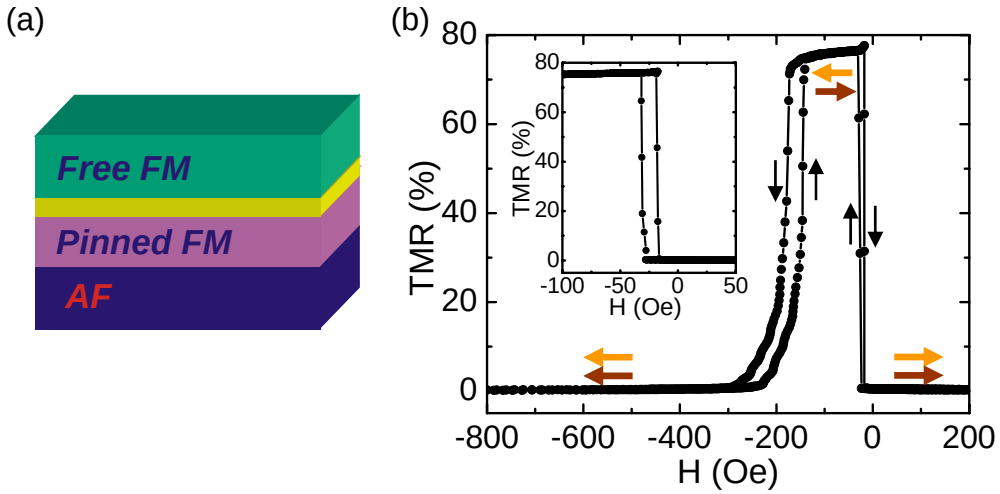

Fig. 2.1 (a) Diagrammatic structure of a MTJ with an antiferromagnetic (AF) layer grown underneath to provide exchange bias; (b) Typical magnetoresistance loop of a MTJ device, the inset is the minor loop. The horizontal arrows show the magnetic moments' directions in the two electrodes, and the vertical arrows denote the field sweeping directions.

Over the past ten years, most of the research in spin dependent tunneling has focused on MTJs with an Al_2O_3 tunnel barrier[7-9]. Although intensive efforts have been made in such MTJs, the maximum TMR only reached about 70%[10,11]. Meanwhile, extensive theoretical and experimental work has been carried out to increase the TMR by incorporating exotic oxide or half-metal layers into MTJs[12-15], and studying crystalline tunneling barriers[16,17]. Butler *et al.* carried out first-principles calculations of tunneling conductance and magnetoresistance in epitaxial Fe/MgO/Fe sandwiches[16]. They revealed that tunneling conductance depends strongly on the symmetry of the Bloch states in the electrodes and of the evanescent states in the barrier, thus Bloch states of different symmetry decay at different rates within the barrier. The Δ_1 state, due to its "s-character", decays slowest among all the states and can make a significant contribution to the tunneling conductance. Because the Δ_1 state only occurs at the Fermi level for the majority band, it behaves much like a "half-metal". Giant TMR was expected in *bcc* Fe/MgO/Fe, CoFe/MgO/CoFe, and Co/MgO/Co tunneling junctions. Experimental results of TMR above ~200% were first

reported by Parkin *et al.* and Yuasa *et al.* respectively[18,19]. Room temperature TMR results of about 600% in MgO based tunnel junctions have also been obtained recently[20].

For high-quality Al_2O_3 tunnel junctions, the magnitude of the TMR at low bias can be well understood within the framework of Jullière's model, $TMR = \frac{2P_1P_2}{1-P_1P_2}$, where P_1, P_2 are the spin polarization of the two electrode materials and they can be well derived from the ferromagnet/insulator/superconducting tunnel junctions first introduced by Meservy and Tedrow[21]. In this model, it is assumed that during the tunneling process, spin is conserved, namely no spin-flipping occurs. The conductance in each channel is thus proportional to the tunneling probability, which is determined by Fermi's golden rule (Fig. 2.2). However, such a quantitative comparison is not always straightforward. For example, TMR is extremely sensitive to the interface between the electrode and barrier in realistic systems[22,23]. In MgO based MTJs, due to coherent tunneling effect, the physics of the spin dependent tunneling effect is far beyond this oversimplified model. Given the simplicity of the model, Slonczewski calculated an approximate expression of the TMR of free electrons tunneling through a square barrier based on the Landauer-Büttiker formalism[24]. Tsymbal *et al.* studied the interface dependence of the tunneling conductance[23]. For the coherent tunneling through a crystalline system many theoretical studies emerged together with the experimental achievements in MgO based tunnel junctions[16-19].

In conventional MTJs, TMR always decreases with applied bias voltage. The voltage at which the magnitude decreases to half of the low bias value is called $V_{1/2}$, usually around 0.5 V for high quality Al_2O_3 or MgO based MTJs with transition metal electrodes[11,19]. The TMR decrease mainly comes from the much greater resistance drop in the anti-parallel (AP) state with bias voltage compared to the parallel (P) state. One mechanism for the decrease in TMR as a function of bias is the interface magnon excitation[25]. Another is the presence of defect states within the tunnel barrier, which may allow an increase amount of defect-state-assisted tunneling and dilute the spin polarization of the tunneling current at elevated bias voltage[26,27].

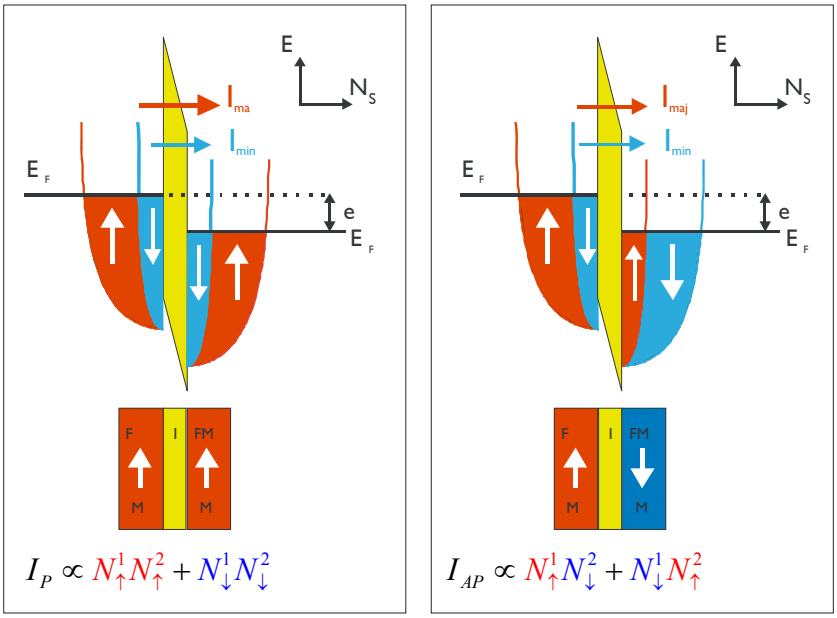

Fig. 2.2 Illustration of the Jullière's model in a magnetic tunnel junction for parallel configuration (left) and antiparallel configuration (right). The current is determined by the product of the density of filled states in one electrode and the density of empty states in the other electrode. Parallel configuration usually has lower resistance than that of antiparallel configuration, thus resulting in a positive TMR effect.

2.1.2 Spin Transfer Torque

Spin transfer torque (STT) effect was first theoretically studied by Slonczewski and Berger in 1996[28,29]. When a spin-polarized current pass through a non-collinear thin magnetic layer, due to the conservation of the spin momentum via exchange interaction, the transverse component of the spin in the flowing electrons can be transferred to the conduction electrons in the small magnet. Depending on the direction of electron flow and the magnetic configuration, this spin-polarized current favors either the P state or AP state (Fig. 2.3). The electrode of smaller thickness, which can be switched, is called the free layer (FL); in contrast, the other electrode, which is usually thicker and exchange biased, is called pinned layer (PL). Such a STT induced magnetization reversal is a relatively new phenomenon, and it is observable only in magnetic structures smaller than 100-200 nm[30-32]. A macro-spin model treats a nanomagnet with the assumption that its internal magnetic degrees of freedom are frozen, so that the

dynamics of macro-spin can be phenomenologically described by the following Landau-Lifshitz-Gilbert (LLG) equation with an extra STT term[33,34]:

$$\partial_t \vec{m} = \gamma\left(\vec{m}\times\vec{H}_{\text{eff}}\right) - \alpha\left(\vec{m}\times\partial_t\vec{m}\right) + \beta J\left(\vec{m}\times\vec{m}\times\vec{M}\right)$$

where γ is the gyromagnetic ratio, α the damping coefficient, β the coefficient for the STT which depends on both the spin polarization and the geometric configuration between the incoming spin and the local moments in the FL, and J the current density.

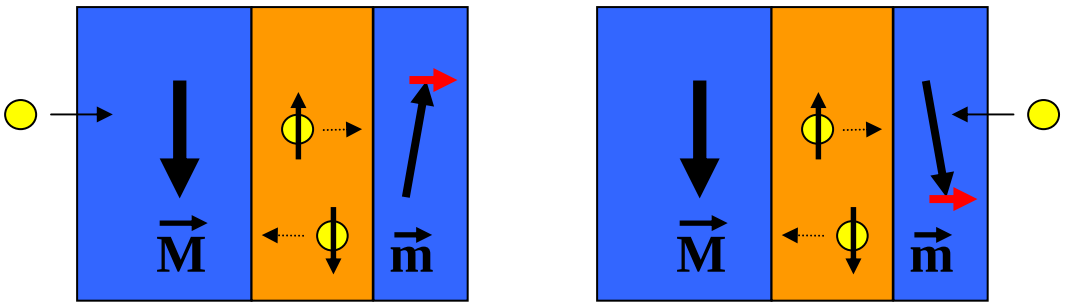

Fig. 2.3 The thick electrode is pinned layer (PL), and the thin one is free layer (FL). When electrons flow from PL to FL, due to spin transfer torque effect, it favors parallel state (left); on the other hand, when electrons flow from FL to PL, it favors antiparallel state.

The competition between the damping term and the spin torque term is illustrated in Fig. 2.4. When J is small and the spin torque term less than the damping term, the dynamics damp out into an equilibrium state. When the spin torque is large enough that it overcomes the intrinsic damping, effective damping coefficient becomes negative, the deviation from the equilibrium state is amplified and the magnetic moments are switched, which can be detected by a resistance change in the magnetic sandwiched structure, e.g. MTJs or spin-valves[30,35,36]. When J and H satisfy certain conditions, persistent precession of the magnetization can be obtained at a frequency of several GHz. When the precession occurs, the angle between the magnetic moments in the FL and PL changes rapidly. Due to the magnetoresistance effect, it gives rise to a resistance change at high frequency; therefore a dc current/voltage induced rf microwave emission can be observed in the device[32,37-42].

Since the STT can change the magnetic state of a small magnet by locally injecting a spin polarized current, it promises a better writing scheme than that used in conventional magnetic random access memory (MRAM). The STT-RAM has excellent

write selectivity since the current passing through a storage cell can directly change the state of that cell, i.e. write "0" or "1" there. The minimum current density needed to write one bit scales down with the device size, which means that STT-RAM has much higher scalability. Besides, STT-RAM also promises lower power consumption and much simpler architecture. A side-by-side comparison between them in terms of circuit design is shown in Fig. 2.5. STT-induced persistent precession can emit rf microwaves with reasonable power, however, their frequencies can be tuned by the applied voltage or current alone, which makes STT-nano-oscillator very promising.

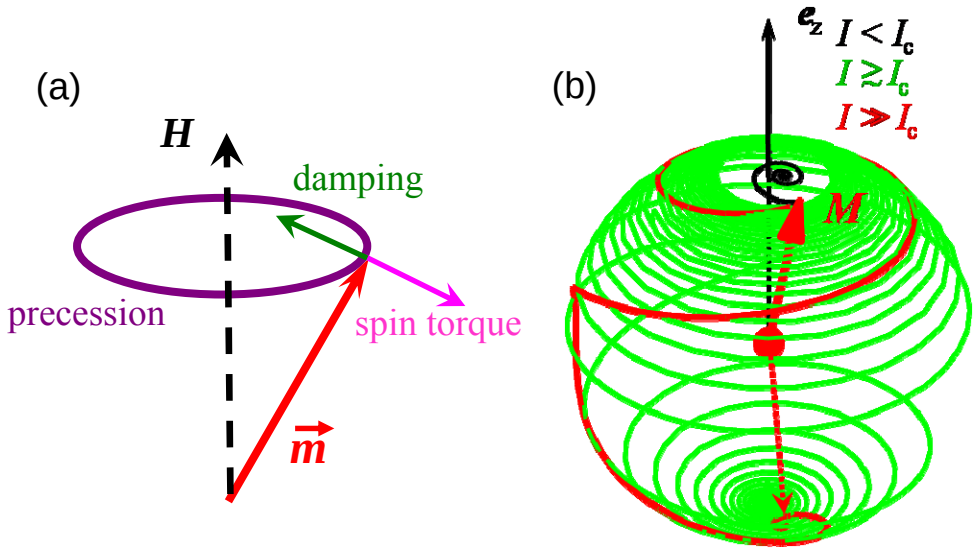

Fig. 2.4 (a) Geometric illustration of Landau-Lifshitz-Gilbert (LLG) equation with a spin transfer torque term; (b) Dynamics of the magnetic moments in the free layer (FL) when the damping term is larger, comparable, or smaller than the spin-torque term with various magnitudes of spin polarized current.

With these new phenomena in physics and potential applications in technology, the STT effect has been stimulating great interest in both academics and industry since the beginning of its discovery. Physicists first observed the STT-induced spin-wave excitation in extended magnetic films with either a point contact or membrane structure[30-32]. Later, full switching of a thin magnetic layer was achieved in ebeam patterned nano-pillars[30], where the size of the device is well defined, making possible the quantitative study of the STT effect. Initially, most of the work about the STT effect only focused on metallic structures, e.g. spin-valves, due to the relative ease in the fabrication of these nano-pillars compared to those with MTJs. However, MTJs are

more attractive to use in devices because they have inherently higher resistance. This is useful in the very small scale solid-state circuitry, and successful switching of magnetization in MgO based MTJs has been observed[35,36]. Besides, due to their much higher magnetoresistance effect, they are more desirable as memory storage cells which can tolerate greater error margins. They are also promising candidates for nano-oscillator because they can emit higher power due to their larger resistance change[39,43,44].

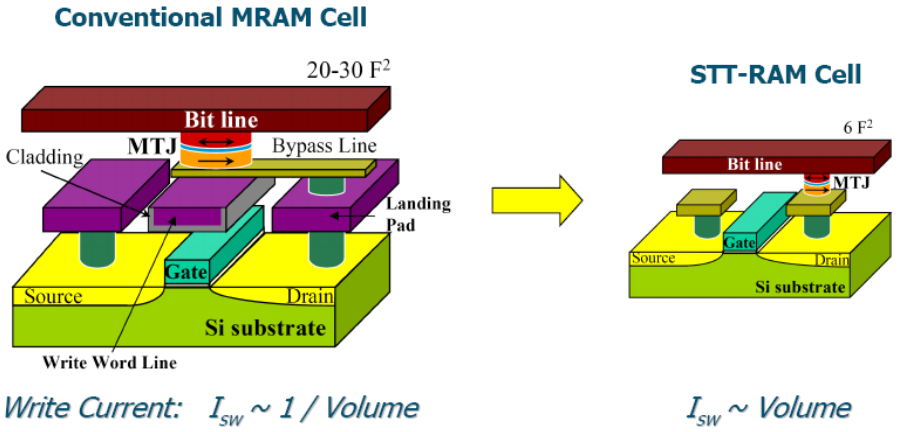

Fig. 2.5 Comparison between the conventional MRAM (left) and STT-RAM (right). Clearly, much simpler electronic architecture is proposed for STT-RAM than the conventional MRAM.

2.2 EXPERIMENTAL TECHNIQUES

A number of thin film characterization techniques have been used in this research dissertation, such as vibrating sample magnetometry (VSM), superconducting quantum interference device (SQUID), x-ray diffraction (XRD), x-ray photoelectron spectroscopy (XPS), x-ray emission spectroscopy (XES), Rutherford backscattering spectroscopy (RBS), transmission electron microscopy (TEM), scanning electron microscopy (SEM), and atomic force microscopy (AFM). Interested readers can find references somewhere else. Most of the electrical transport results were simply based on four-point measurements so as to exclude the influence of electrical contact resistance on the measured device resistance. AC lock-in technique was also used to detect small signal, or to probe the fine electronic structure in MTJs. Specific

experimental setups for the different experiments will be discussed later in the respective chapters. However, one special technique, i.e. superconducting tunneling spectroscopy, will be described in details in this section due to its theoretical and experimental complexities.

2.2.1 Superconducting Tunneling Spectroscopy

Spin polarization is a crucial metric for all spin related phenomena. It can be probed by a variety of techniques, such as photoemission[45], point contact Andreev reflection[46], and superconducting tunneling spectroscopy (STS)[21]. Regarding the spin dependent tunneling effect in MTJs, STS is the most reliable and relevant technique to determine the tunneling spin polarization (TSP). In this technique, TSP is measured from a tunnel junction with an electrode of the interested material and a counter electrode of a superconducting material. Slightly doped aluminum with copper or silicon is commonly used as the superconducting electrode, where the doping can increase the critical temperature T_c of the superconductor. With a large field applied in the film plane, the superconducting electrode works as an analyzer for the spin-polarized current. This technique was first developed by Meservey and Tedow, and has been used to measure many ferromagnetic and ferromagnetic materials including *3d* transition metals and their alloys and some rare-earth metal based alloys[21,47,48].

When a bias voltage is applied across the tunnel junction, the initially aligned Fermi levels in the two electrodes are shifted, therefore giving rise to a tunneling current. According to Fermi's golden rule, the current that is directly correlated with the tunneling probability, is determined by the product of the density of filled states of a given energy in one electrode and the density of empty states at the same energy in the other electrode. By this rule, the currents of tunneling electrons from left electrode to right electrode at energy E and vice versus are,

$$I_{+}(V,E) \sim N_1(E+eV)\,N_2(E)\,f(E+eV)\left[1-f(E)\right]$$
$$I_{-}(V,E) \sim N_1(E+eV)\,N_2(E)\left[1-f(E+eV)\right]f(E)$$

respectively, where V is the applied voltage, $N_{1,2}$ are the density of states of the two electrodes, and f is the Fermi function. Thus the total current I, given by $\int_{-\infty}^{+\infty} I_+(V,E) - I_-(V,E)\,dE$, is equal to,

$$I(V) \sim \int_{-\infty}^{+\infty} N_1(E+eV)\,N_2(E)\left[f(E+eV) - f(E)\right]dE$$

For a non-magnetic metal, we can assume the density of sates around the Fermi energy within a small range is constant; however, a superconductor behaves differently. Therefore, the integration must be carried out over it, and the differential conductance can be easily derived,

$$\frac{dI(V)}{dV} \sim N_n \int_{-\infty}^{+\infty} N_s(E)\, f'(E+eV)\,dE$$

For the case of tunneling from a magnetic material, when we calculate the conductance we must consider both the spin-up and spin-down channels.

$$\frac{dI(V)}{dV} \sim N_\uparrow \int_{-\infty}^{+\infty} N_{s\uparrow}(E)\, f'(E+eV)\,dE + N_\downarrow \int_{-\infty}^{+\infty} N_{s\downarrow}(E)\, f'(E+eV)\,dE$$

Where the spin conservation is assumed during the tunneling process, and $N_{\uparrow(\downarrow)}$ and $N_{s\uparrow(s\downarrow)}$ are the spin-up (spin-down) density of states in the magnetic materials and in the superconductor. Experimentally it was found that with a magnetic field applied in the superconductor plane, the BCS density of states of quasiparticles, $N_s^{\uparrow\downarrow}(E) = \frac{E}{\sqrt{E^2-\Delta^2}}$, are Zeeman-split into $N_s^{\uparrow\downarrow}(E) = \frac{E \pm g\mu_B H/2}{\sqrt{(E \pm g\mu_B H/2)^2 - \Delta^2}}$, as shown in Fig. 2.6 (a). At low temperature, the derivative of the Fermi function f' approaches that of a δ function. Consequently, four asymmetric peaks are obtained in the $\frac{dI(V)}{dV} \sim V$ curves, with each spin channel contributing to two peaks and spin density of states asymmetry determining the height asymmetry among these peaks (Fig. 2.6 (c)). Approximately, the TSP can be estimated by $P = \frac{(\sigma_4 - \sigma_2) - (\sigma_1 - \sigma_3)}{(\sigma_4 - \sigma_2) + (\sigma_1 - \sigma_3)}$.

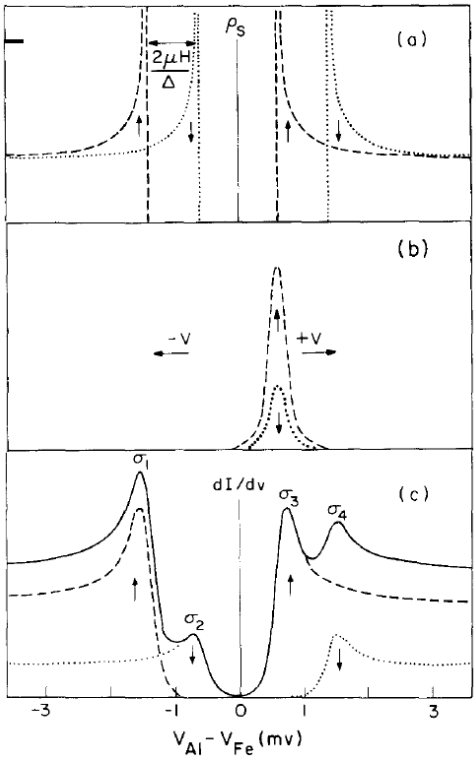

Fig. 2.6 Superconducting-ferromagnetic-metal tunneling[21]. *(a) BCS density of states of a superconductor as a function of voltage in a magnetic field; (b) Temperature-dependent kernels for each spin channel in the integral expression for differential conductance; (c) Theoretical normalized conductance for each spin channel (dotted and dashed curves) and the total conductance (solid line).*

In the simple BCS theory, neither the orbital depairing due to the applied field nor spin-flip scattering due to the spin-orbit coupling (SOC) is included. A more complicated DOS calculation was completed by Maki after taking these factors into account[49,50],

$$N_s^{\uparrow\downarrow}(E) = \frac{N_s(0)}{2}\mathrm{sgn}(E)\,\mathrm{Re}\left(\frac{u_\pm}{\left(u_\pm^2-1\right)^{1/2}}\right)$$

where u_+ and u_- are implicitly defined by $u_\pm = \dfrac{E \mp \mu_B H}{\Delta} + \dfrac{\varsigma u_\pm}{\left(1-u_\pm^2\right)^{1/2}} + b\left(\dfrac{u_\mp - u_\pm}{\left(1-u_\mp^2\right)^{1/2}}\right)$,

Δ is the energy gap of the superconductor, $N_s(0)$ is the normal density of states, ς is the orbital depairing parameter, and b is the spin-orbit scattering parameter[51], In each experiment with applied field and temperature known, the conductance curve is fit

by Maki's theory with Δ, ς, b and *TSP* as fitting parameters. The TSP results can be derived with high accuracy[52]. One of our typical TSP measurements and analysis are shown in Fig. 3.7.

2.3 DEVICE PREPARATION

All the films grown for the research are deposited on thermally oxidized 1-inch Si wafers. The deposition system is equipped with several dc magnetron sputtering guns, a plasma oxidation source, and an ion beam sputter source with a five target turret and an electron-beam evaporation source shown in Fig. 2.7. Every time after opening the chamber and loading cleaned Si substrates, the system is usually baked for 8~10 hours at 120 °C, and the chamber thereafter reaches a base pressure of better than 10^{-8} *Torr*. With the capacity of 24 substrates, any gas mixture among Ar, O_2 and N_2, and more than 11 targets, the system allows to explore materials intensively and to optimize structures efficiently.

The deposition conditions vary depending on the desired materials. Metallic films are usually deposited with an Ar atmosphere at a pressure of 3 m*Torr*, and oxide barriers are normally grown by reactive sputtering in an Ar/O_2 mixture with an optimal ratio between 97/3 and 95/5. Small permanent magnets with a field about 100 Oe are placed above the substrate to set the moments direction in magnetic layer, especially to establish the exchange bias.

There are two ways to make the final measurable devices: one is directly patterning the film with *in situ* shadow masks; the other is patterning the devices from uniformly deposited films using optical or ebeam lithography in a clean room. (Fig. 2.7)

2.3.1 Shadow Masked Devices

The film deposition and device patterning process is fully automated by computer. By controlling a motor inside the chamber, both the substrate platter and the mask platter

can rotate independently, therefore it is easy to move the selected substrate and desired mask to the desired target. By remotely turning the power on and opening the shutter afterwards, we can control the time for both pre-sputtering the target and film growth onto the substrate. With up to 8 copper-beryllium masks of different design in the system, we can easily *in situ* pattern films in to devices down to 20 μm, although for MTJs, usually 3 masks are enough, i.e. one each for the bottom electrode, for the barrier and for the top electrode.

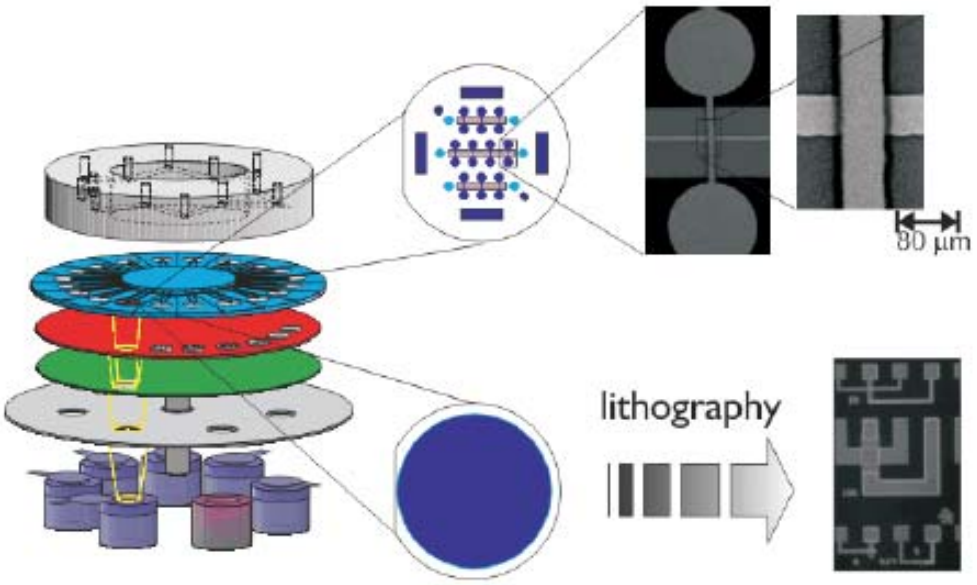

Fig. 2.7 Schematic of the sputtering system (left); Shadow masking is used to define the electrodes and barriers (upper middle), and blank film is grown for lithography (lower middle); Scanning electron microscopy (SEM) images for some devices, respectively (right).

During film growth, all the times and deposition rates are recorded in a log file from quartz-crystal monitors to insure the film is grown at a right rate. More accurate rate for one material at a defined power is determined by calibration films with a nominal 500 Å thickness grown with a specially designed calibration mask. After measuring the actual thickness by profilometer, accurate deposition rates are derived, which are typically on the order of 1 Å/s. Furthermore, the calibration films can be analyzed with other tools to characterize the quality of the deposited films, such as, Rutherford backscattering spectroscopy which gives the composition of alloy films as well as impurity concentrations and thicknesses of the film, and vibrating sample magnetometer which reveals the magnetic properties of the film.

2.3.2 Nano-Pillar Devices

Devices used for the STT studies are fabricated by ebeam lithography and standard optical lithography. Films were grown with the same technique, however, without use of any shadow masks. Before being brought into the clean room, samples are usually annealed at an optimal condition, which is determined by the thermal stability and TMR of the shadow-masked larger devices with identical multilayered structures. It takes four major steps to fabricate the devices with a size of ~100 nm.

(i). Alignment Mark. Bilayers of photoresist (SPR670 600nm/PMGI-SFG 50nm) are used in this step to make an undercut for ease of later liftoff. After the resists spin and bake, they are exposed with an alignment mark mask for 1.5 seconds with 1000 W in a contact printer. Develop the exposed resist in Optiyield developer for 45 seconds, and deposit Ta 5 nm/Au 65 nm metal layers where thin Ta is used to increase the adhesion. Finally, dissolve the resist with NMP and liftoff the metal, which generates four alignment marks with size of 10×10 μm^2 at each of the four corners across the wafer.

(ii). Device Region and Bottom Electrode. Device fabrication regions with full stack of the film are defined by ebeam lithography. After resist spinning, exposing and developing, resist islands with bottom electrode shape remain on the wafer. Using the resist as a hard mask, the rest of the metal layers are ion-milled to etch through the whole film stack, thus a matrix of separated regions for later device fabrication is formed. This process is precisely monitored by secondary ion mass spectroscopy (SIMS). After a complete etching, Al_2O_3 of the same thickness as the totally etched layers is deposited *in situ* by ion beam deposition (IBD). Liftoff with swabbing and ultrasonic agitation in N-Methyl-2-Pyrrolidone (NMP), the device fabrication regions and bottom electrodes are defined.

(iii). Tunnel Junction. Small junctions of sizes from 50×100 to 90×270 nm^2 are fabricated by ebeam lithography. Bialyers of ebeam resist (HSQ 85 nm/Duramide 40 nm) are spun onto the substrate, with each of them baked at 100 °C and 175 °C for 30 seconds. After developing, HSQ resist islands with the desired tunnel junction shape and size remain on the wafer. Oxygen reactive ion etching treatment transfers the HSQ

pattern onto Duramide, which also creates a slight undercut there. With HSQ/Duramide as a hard mask, an ion-mill is used to etch through the film to the pinned ferromagnetic layer. The ion beam starts with an incident angle between 0 to 10 degrees from perpendicular to the surface, followed by a sidewall cleaning roughly with 2× time of the etching. The un-etched bottom layers beneath tunneling barrier serve as bottom electrode, and small pillars defined by the resist islands are the active tunnel junctions. Al_2O_3 is then deposited with the same thickness as the etched depth. After liftoff, small holes on top of the pillars, namely tunnel junctions, are opened for making top electrodes.

(iv). Electrical Contact. The surface is first de-scummed with O_2 plasma for 40 seconds with a pressure of 500 *Torr*, and then the contact metal (Ta 5 nm/Au 180 nm) is deposited. After resist spinning, exposing, and developing, the patterns of both the top and bottom contacts are defined. Ion-mill is used to etch away the rest of the Ta/Au stack, and the electrical contacts are generated. Finally, resist is removed by swabbing and ultrasonic agitation with NMP.

REFERENCES:

[1] S. Parkin, X. Jiang, C. Kaiser, A. Panchula, K. Roche, and M. Samant, "Magnetically Engineered Spintronic Sensors and Memory," Proc. IEEE **91**, 661 (2003).

[2] M. Julliere, "Tunneling between ferromagnetic films," Phys. Lett. A **54**, 225 (1975).

[3] S. Maekawa and U. Gafvert, "Electron tunneling between ferromagnetic films," IEEE Trans. Magn. **18**, 707 (1982).

[4] J. Nowak and J. Rauluszkiewicz, "Spin dependent electron tunneling between ferromagnetic films," J. Magn. Magn. Mater. **109**, 79 (1992).

[5] T. Miyazaki and N. Tezuka, "Giant magnetic tunneling effect in Fe/Al_2O_3/Fe junction," J. Magn. Magn. Mater. **139**, L231 (1995).

[6] J. S. Moodera, L. R. Kinder, T. M. Wong, and R. Meservey, "Large Magnetoresistance at Room Temperature in Ferromagnetic Thin Film Tunnel Junctions," Phys. Rev. Lett. **74**, 3273 (1995).

[7] P. LeClair, J. T. Kohlhepp, C. H. van de Vin, H. Wieldraaijer, H. J. M. Swagten, W. J. M. de Jonge, A. H. Davis, J. M. MacLaren, J. S. Moodera, and R. Jansen, "Band Structure and Density of States Effects in Co-Based Magnetic Tunnel Junctions," Phys. Rev. Lett. **88**, 107201 (2002).

[8] J. S. Moodera, J. Nowak, and R. J. M. van de Veerdonk, "Interface Magnetism and Spin Wave Scattering in Ferromagnet-Insulator-Ferromagnet Tunnel Junctions," Phys. Rev. Lett. **80**, 2941 (1998).

[9] S. Yuasa, T. Nagahama, and Y. Suzuki, "Spin-Polarized Resonant Tunneling in Magnetic Tunnel Junctions," Science **297**, 234 (2002).

[10] D. Wang, C. Nordman, J. M. Daughton, Z. Qian, and J. Fink, "70% TMR at Room Temperature for SDT Sandwich Junctions With CoFeB as Free and Reference Layers," IEEE Trans. Magn. **40**, 2269 (2004).

[11] J. J. Yang, C. Ji, Y. A. Chang, X. Ke, and M. S. Rzchowski, "Over 70% tunneling magnetoresistance at room temperature for a CoFe and AlOx based magnetic tunnel junction," Appl. Phys. Lett. **89**, 202502 (2006).

[12] A. M. Bratkovsky, "Tunneling of electrons in conventional and half-metallic systems: Towards very large magnetoresistance," Phys. Rev. B **56**, 2344 (1997).

[13] A. M. Bratkovsky, "Assisted tunneling in ferromagnetic junctions and half-metallic oxides," Appl. Phys. Lett. **72**, 2334 (1998).

[14] J. M. De Teresa, Barth, eacute, A. my, egrave, A. Fert, J. P. Contour, F. Montaigne, ccedil, ois, and P. Seneor, "Role of Metal-Oxide Interface in Determining the Spin Polarization of Magnetic Tunnel Junctions," Science **286**, 507 (1999).

[15] C. T. Tanaka, J. Nowak, and J. S. Moodera, "Spin-polarized tunneling in a half-metallic ferromagnet," J. Appl. Phys. **86**, 6239 (1999).

[16] W. H. Butler, X.-G. Zhang, T. C. Schulthess, and J. M. MacLaren, "Spin-dependent tunneling conductance of Fe|MgO|Fe sandwiches," Phys. Rev. B **63**, 054416 (2001).

[17] J. Mathon and A. Umerski, "Theory of tunneling magnetoresistance of an epitaxial Fe/MgO/Fe(001) junction," Phys. Rev. B **63**, 220403 (2001).

[18] S. S. P. Parkin, C. Kaiser, A. F. Panchula, P. Rice, M. G. Samant, S.-H. Yang, and B. Hughes, "Giant tunneling magnetoresistance at room temperature with MgO (100) tunnel barriers," Nature Materials **3**, 862 (2004).

[19] S. Yuasa, T. Nagahama, A. Fukushima, Y. Suzuki, and K. Ando, "Giant room-temperature magnetoresistance in single-crystal Fe/MgO/Fe magnetic tunnel junctions," Nature Materials **3**, 868 (2004).

[20] S. Ikeda, J. Hayakawa, Y. Ashizawa, Y. M. Lee, K. Miura, H. Hasegawa, M. Tsunoda, F. Matsukura, and H. Ohno, "Tunnel magnetoresistance of 604% at 300K by suppression of Ta diffusion in CoFeB/MgO/CoFeB pseudo-spin-valves annealed at high temperature," Appl. Phys. Lett. **93**, 082508 (2008).

[21] R. Meservey and P. M. Tedrow, "Spin-polarized electron tunneling," Phys. Rep. **238**, 173 (1994).

[22] C. Kaiser, S. van Dijken, S.-H. Yang, H. Yang, and S. S. P. Parkin, "Role of Tunneling Matrix Elements in Determining the Magnitude of the Tunneling Spin Polarization of 3d Transition Metal Ferromagnetic Alloys," Phys. Rev. Lett. **94**, 247203 (2005).

[23] E. Y. Tsymbal, K. D. Belashchenko, J. P. Velev, S. S. Jaswal, M. v. Schilfgaarde, I. I. Oleynik, and D. A. Stewart, "Interface effects in spin-dependent tunneling," Prog. Mater. Sci. **52**, 401 (2007).

[24] J. C. Slonczewski, "Conductance and exchange coupling of two ferromagnets separated by a tunneling barrier," Phys. Rev. B **39**, 6995 (1989).

[25] S. Zhang, P. M. Levy, A. C. Marley, and S. S. P. Parkin, "Quenching of Magnetoresistance by Hot Electrons in Magnetic Tunnel Junctions," Phys. Rev. Lett. **79**, 3744 (1997).

[26] J. Klein, C. Hofener, S. Uhlenbruck, L. Alff, B. Buchner, and R. Gross, "On the nature of grain boundaries in the colossal magnetoresistance manganites," Europhys. Lett. **47**, 371 (1999).

[27] J. Zhang and R. M. White, "Voltage dependence of magnetoresistance in spin dependent tunneling junctions," J. Appl. Phys. **83**, 6512 (1998).

[28] L. Berger, "Emission of spin waves by a magnetic multilayer traversed by a current," Phys. Rev. B **54** (13), 9353 (1996).

[29] J. C. Slonczewski, "Current-driven excitation of magnetic multilayers," J. Magn. Magn. Mater. **159**, L1-L7 (1996).

[30] J. A. Katine, F. J. Albert, R. A. Buhrman, E. B. Myers, and D. C. Ralph, "Current-Driven Magnetization Reversal and Spin-Wave Excitations in Co/Cu/Co Pillars," Phys. Rev. Lett. **84** (14), 3149-3152 (2000).

[31] E. B. Myers, D. C. Ralph, J. A. Katine, R. N. Louie, and R. A. Buhrman, "Current-Induced Switching of Domains in Magnetic Multilayer Devices," Science **285**, 867-870 (1999).

[32] M. Tsoi, A. G. M. Jansen, J. Bass, W.-C. Chiang, V. Tsoi, and P. Wyder, "Generation and detection of phase-coherent current-driven magnons in magnetic multilayers," Nature **406**, 46 (2000).

[33] J. Z. Sun, "Spin-current interaction with a monodomain magnetic body: A model study," Phys. Rev. B **62** (1), 570 (2000).

[34] J. Xiao, A. Zangwill, and M. D. Stiles, "Macrospin models of spin transfer dynamics," Phys. Rev. B **72** (1), 014446 (2005).

[35] J. Hayakawa, S. Ikeda, Y. M. Lee, R. SasaKi, T. Meguro, F. Matsukura, H. Takahashi, and H. Ohno, "Current-Driven Magnetization Switching in CoFeB/MgO/CoFeB Magnetic Tunnel Junctions," Jpn. J. Appl. Phys. **44** (41), L1267-L1270 (2005).

[36] H. Kubota, A. Fukushima, Y. Ootani, S. Yuasa, K. Ando, H. Maehara, K. Tsunekawa, D. D. Djayaprawira, N. Watanabe, and Y. Suzuki, "Evaluation of Spin-Transfer Switching in CoFeB/MgO/CoFeB Magnetic Tunnel Junctions," Jpn. J. Appl. Phys. **44** (40), L1237-L1240 (2005).

[37] G. Bertotti, C. Serpico, I. D. Mayergoyz, A. Magni, M. d'Aquino, and R. Bonin, "Magnetization Switching and Microwave Oscillations in Nanomagnets Driven by Spin-Polarized Currents," Phys. Rev. Lett. **94**, 127206- (2005).

[38] O. Boulle, V. Cros, J. Grollier, L. G. Pereira, C. Deranlot, F. Petroff, G. Faini, J. Barnas, and A. Fert, "Shaped angular dependence of the spin-transfer torque and microwave generation without magnetic field," Nat. Phys. **3**, 492 (2007).

[39] A. M. Deac, A. Fukushima, H. Kubota, H. Maehara, Y. Suzuki, S. Yuasa, Y. Nagamine, K. Tsunekawa, D. D. Djayaprawira, and N. Watanabe, "Bias-driven high-power microwave emission from MgO-based tunnel magnetoresistance devices," Nat. Phys. **4**, 803 (2008).

[40] S. Kaka, M. R. Pufall, W. H. Rippard, T. J. Silva, S. E. Russek, and J. A. Katine, "Mutual phase-locking of microwave spin torque nano-oscillators," Nature **437**, 389 (2005).

[41] S. I. Kiselev, J. C. Sankey, I. N. Krivorotov, N. C. Emley, R. J. Schoelkopf, R. A. Buhrman, and D. C. Ralph, "Microwave oscillations of a nanomagnet driven by a spin-polarized current," Nature **425**, 380 (2003).

[42] S. M. Rezende, F. M. de Aguiar, R. L. Rodriguez-Suarez, and A. Azevedo, "Mode Locking of Spin Waves Excited by Direct Currents in Microwave Nano-oscillators," Phys. Rev. Lett. **98**, 087202 (2007).

[43] D. Houssameddine, U. Ebels, B. Delaet, B. Rodmacq, I. Firastrau, F. Ponthenier, M. Brunet, C. Thirion, J. P. Michel, L. Prejbeanu-Buda, M. C. Cyrille, O. Redon, and B. Dieny, "Spin-torque oscillator using a perpendicular polarizer and a planar free layer," Nat. Mater. **6**, 447 (2007).

[44] A. V. Nazarov, H. M. Olson, H. Cho, K. Nikolaev, Z. Gao, S. Stokes, and B. B. Pant, "Spin transfer stimulated microwave emission in MgO magnetic tunnel junctions," Appl. Phys. Lett. **88**, 162504 (2006).

[45] Y. S. Dedkov, U. Rudiger, and G. Guntherodt, "Evidence for the half-metallic ferromagnetic state of Fe3O4 by spin-resolved photoelectron spectroscopy," Phys. Rev. B **65**, 064417 (2002).

[46] R. J. Soulen, Jr., J. M. Byers, M. S. Osofsky, B. Nadgorny, T. Ambrose, S. F. Cheng, P. R. Broussard, C. T. Tanaka, J. Nowak, J. S. Moodera, A. Barry, J. M. Coey, nbsp, and D, "Measuring the Spin Polarization of a Metal with a Superconducting Point Contact," Science **282**, 85 (1998).

[47] C. Kaiser, A. F. Panchula, and S. S. P. Parkin, "Finite Tunneling Spin Polarization at the Compensation Point of Rare-Earth-Metal--Transition-Metal Alloys," Phys. Rev. Lett. **95**, 047202 (2005).

[48] C. Kaiser and S. S. P. Parkin, "Spin polarization in ferromagnet/insulator/superconductor structures with the superconductor on top of the barrier," Appl. Phys. Lett. **84**, 3582 (2004).

[49] K. Maki, "Pauli paramagnetism and superconducting state II," Prog. Theor. Phys. **32**, 29 (1964).

[50] R. Meservey, P. M. Tedrow, and R. C. Bruno, "Tunneling measurements on spin-paired superconductors with spin-orbit scattering," Phys. Rev. B **11**, 4224 (1975).

[51] P. Fulde, "High field superconductivity in thin films," Adv. Phys. **22**, 667 (1973).

[52] D. C. Worledge and T. H. Geballe, "Maki analysis of spin-polarized tunneling in an oxide ferromagnet," Phys. Rev. B **62**, 447 (2000).

Chapter 3

ENHANCED TUNNELING MAGNETORESISTANCE FROM AMORPHOUS COFE ALLOY

3.1 INTRODUCTION

As discussed in Chapter 2, the tunneling magnetoresistance (TMR) effect[1-4] in magnetic tunnel junctions (MTJs) is of great importance both scientifically and technologically. The MTJ not only provides an excellent platform to study the fundamental physics of spin dependent tunneling, but also plays a central role in many of the most useful spintronic devices including high-performance solid-state magnetic random access memories (MRAM) and magnetic sensors[5]. It is now generally accepted that TMR is very sensitive to the electronic structures of the electrodes and the tunnel barrier, and to interfacial bonding between them[6,7]. Spin polarization can be obtained from first-principle calculations, and it can be dependent on the tunneling direction. Experiments showing the influence of crystalline anisotropy of spin polarization on TMR have been reported[8]. A clear relationship between electrode crystal structure and junction magnetotransport properties was also presented utilizing Al_2O_3 based MTJs with Co electrodes of different crystalline phases[9]. However, in all these work, changing the orientation of the electrodes is usually made by engineering the buffer layers on which both the electrodes and barrier were grown. This compromises the results of the TMR and spin polarization comparison among different crystal structures and makes them inconclusive because TMR can also be significantly influenced by underlayers, especially when the MTJs are annealed at elevated temperatures.

Of particular interest technologically are amorphous ferromagnetic electrodes which may allow for more uniform magnetic switching of devices fabricated at sub-100-nm dimensions. Recently, ferromagnetic CoFe alloys made amorphous by the addition of boron have become of special interest because MTJs incorporating them show the highest TMR values at room temperature of any magnetic electrode. This is found for MTJs formed with either amorphous Al_2O_3[10] or crystalline MgO tunnel barriers[3,11-13]. Whether boron plays a direct role in increasing the TMR is however unclear. Previous studies have also considered the effect of crystallization of CoFeB alloys via annealing on tunneling spin polarization and TMR[14,15], but they are complicated by the diffusion of B within the structures.

A common method to make a normally crystalline metallic material amorphous or glassy is by quenching it from its liquid state[16,17]. However, most simple metals will crystallize at room temperature even at the very highest cooling rates. It is possible, in many cases, to prevent crystallization by the incorporation of small amounts of solute atoms which are either much smaller (e.g. B, C, Si) or much larger (e.g. Mo, Hf, Zr) than the host elements[17]. Here it is shown that normally crystalline *bcc* CoFe alloys can be made amorphous without the use of any additives and that the spin polarization of the tunneling current and the associated TMR are correspondingly increased. The observation of amorphous and crystalline CoFe without changing any other film-growth conditions except its thickness provides a suitable platform to compare the TSP of one material in two different structures. The TMR enhancement resulting from the amorphization of a crystalline electrode emphasizes the crucial role of the electrode and barrier interface in determining the spin dependent tunneling.

3.2 MATERIALS AND METHODS

The films were prepared using a combination of ion beam and magnetron sputtering at ambient temperature. The structure of the thin $Co_{70}Fe_{30}$ layer was studied with high resolution cross-section transmission electron microscopy (TEM) on multilayered films composed of five repetitions of the sequence [44 Al_2O_3/t_{SCF} SCF/100 CFB] where the numbers are nominal thicknesses in ångström. The thin sandwiched $Co_{70}Fe_{30}$ (SCF) layer's thickness t_{SCF} is 15, 20, 30, 40, and 50 Å (bottom to top), and the CFB denotes an amorphous CoFeB layer. The repetitions are capped with 50 Ta/50 Ru and are deposited on 100 Ta/250 $Ir_{22}Mn_{78}$/4 $Co_{49}Fe_{21}B_{30}$/35 $Co_{70}Fe_{30}$. Several different compositions of the CFB layer were used. In particular, $Co_{63}Fe_{27}B_{10}$ (CFB10) and $Co_{49}Fe_{21}B_{30}$ (CFB30) were chosen to have lower and higher crystallization temperatures, respectively, than the maximum anneal temperature T_A used in these studies (300 °C). As can be seen clearly in Fig. 3.1(a, b) the SCF layer is amorphous when its thickness is ≤20 Å but is crystalline when ≥30 Å. The amorphous to crystallization transition as a function of the SCF layer thickness, which is one of the

main points of this chapter, can also be unambiguously revealed by electron diffraction images. These images clearly show the difference between the crystalline and amorphous phases of the SCF layer, even though the diffraction spots in the images are inevitably broadened by finite size effects due to the small volume used to obtain these images (2 nm × 2 nm × thickness-of-sample (~10 nm)). Selected area electron diffraction shows that when the SCF layer is crystalline it exhibits a *bcc* structure.

Electron energy loss spectroscopy (EELS)[18] was carried out using high resolution scanning TEM to check whether B might have diffused into the SCF layer, thereby stabilizing an amorphous state. No evidence for this was found within the spatial resolution of the EELS (~5 Å). In any case, an added complication is that the SCF does not wet the Al_2O_3 layer on which it is deposited[19,20]. Thus the SCF grows initially as a discontinuous islanded layer, forming a continuous film only when it reaches a thickness of ~20 Å. In cross-section, EELS will therefore see through portions of both the SCF and CFB layers at the boundary between these layers. However, on annealing EELS showed no change in the B profile (at 300 °C), making diffusion of B into the SCF layer during deposition at ambient temperatures unlikely.

To check whether the morphology of the SCF layer deposited on Al_2O_3 plays a role in stabilizing its amorphous structure, multilayered structures were grown in which the SCF layers are sandwiched on either side by amorphous CFB30 layers without any Al_2O_3 layers, such as, 100 Ta/250 $Ir_{20}Mn_{80}$/100 CFB30/[t_{CoFe}=5, 10, …, and 40 SCF/100 CFB30]$_8$/50 Ta/50 Ru. The SCF layers wet well on metals and are unlikely to form islands, even in the thickness of just several ångstroms. TEM image (Fig. 3.2) indicates that the SCF layers are amorphous for thicknesses up to 20 Å and crystalline for layers above 25 Å thick, a strikingly similar dependence to that for SCF layers deposited directly on Al_2O_3. This confirms that the amorphous nature of the thin SCF layers comes from being sandwiched between two amorphous layers, not islands formation in amorphous hosts.

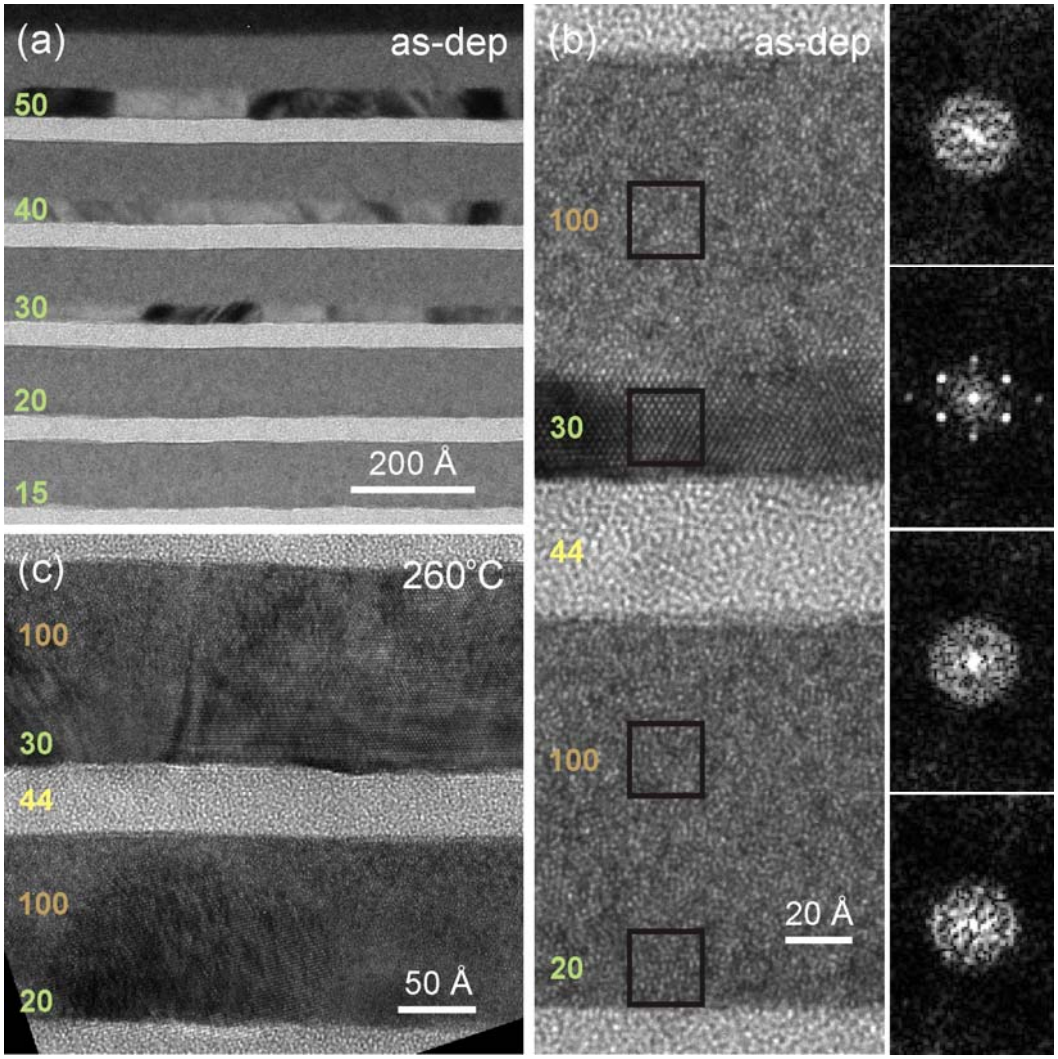

Fig. 3.1 High-resolution cross-section transmission electron microscopy images of 100 Ta/250 $Ir_{22}Mn_{78}$/4 $Co_{49}Fe_{21}B_{30}$/35 $Co_{70}Fe_{30}$/[44 Al_2O_3/t_{SCF} SCF/100 CFB]$_5$/50 Ta/50 Ru with t_{SCF} of 15, 20, 30, 40, and 50 Å; (a) CFB=CFB30, as deposited; (b) high magnification of a portion of (a), together with diffractograms of the four regions indicated by black square outlines in the figure. These regions are taken from (bottom to top) 20 Å SCF, 100 Å CFB30, 30 Å SCF, and 100 Å CFB30: the amorphous to crystalline transition as a function of thickness of the SCF layer is clearly revealed; (c) CFB=CFB10 annealed at 260 ℃. The thicknesses (in Å) of the SCF, Al_2O_3, and CFB layers are labeled in green, yellow, and orange, respectively.

Interestingly, the CFB10 alloy has a much lower crystallization temperature than CFB30 so allowing its crystallization at modest temperatures. Indeed, the TEM in Fig. 3.1(c) shows that the CFB10 has become crystalline after an anneal treatment at 260 °C. Moreover, this induces crystallization of the SCF layers which were previously amorphous. By contrast the CFB30 alloys remains amorphous even to 300 °C, and the thin SCF layers remain amorphous.

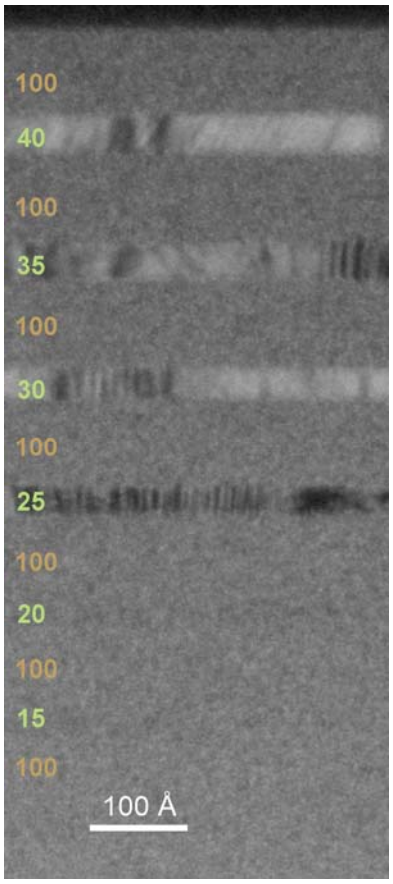

Fig. 3.2 As-deposited all-metal sample, 100 Ta/250 $Ir_{20}Mn_{80}$/100 CFB30/[t_{SCF}=5, 10, 15, …, and 40 SCF/100 CFB30]$_8$/50 Ta/50 Ru. The thicknesses (in Å) of the SCF, Al_2O_3, and CFB30 layers are labeled in green, yellow, and orange, respectively.

Thus, it is concluded that thin CoFe layers can be stabilized in an amorphous state by sandwiching them on either side with various amorphous layers, whether insulating or metallic, and that they display an amorphous to crystalline transition above a critical thickness of ~25 Å. Similar results have previously been found that thin Fe films grown on suitable substrates (eg. Y, Gd, Zr, etc.) at room temperature or below initially form an amorphous phase up to a critical thickness of ~23 Å, and a rapid transformation to a nanocrystalline structure throughout the total Fe layer occurs on further increasing its thickness[21-23]. According to thermodynamic models, the amorphous-to-crystalline transition of CoFe results from a competition between changes in the free energy of the volume and the interfaces of the respective structures. Due to an interfacial-interaction-induced strain relaxation, the amorphous/amorphous interface generally has a lower

energy than the amorphous/crystalline interface. Therefore, thin CoFe layers which have high surface to volume ratio become amorphous at room temperature.

3.3 EXPERIMENTAL RESULTS

3.3.1 Enhanced TMR from Amorphous CoFe

The structure of the SCF layer has an important influence on the magnetotransport properties of MTJs in which they are incorporated. The MTJs were patterned using *in-situ* shadow masks, and they have a lower electrode of an exchange biased crystalline CoFe layer, 100 Ta/250 $Ir_{22}Mn_{78}$/4 $Co_{49}Fe_{21}B_{30}$/35 $Co_{70}Fe_{30}$, an upper electrode formed from a thin SCF layer of thickness t_{SCF} inserted between a top CFB layer, 100 Å thick, and the tunnel barrier. Typical TMR loops are compared in Fig. 3.3 for SCF layers 10 Å and 60 Å thick. The TMR is much higher for the thinner SCF layer (~74% vs. 56%). Moreover, on annealing at 300 °C, its TMR is substantially decreased and H_c is increased nearly five-fold (from ~11 Oe to 54 Oe). By contrast, the sample with the thicker SCF layer shows no significant change in either TMR or H_c for the same anneal.

The detailed anneal temperature dependence of TMR on t_{SCF} is shown in Fig. 3.4 for both CFB10 and CFB30 samples. The results are quite distinct. Let's first consider the case of the CFB10 alloy. The TMR shows a stepwise change from a high value for thin SCF layers to a significantly lower value for thicker layers. This transition takes place at t_{SCF}>20 Å at the lowest anneal temperature of 220 °C, but with increasing T_A the transition moves to thinner SCF layers and disappears at T_A= 300 °C so that the TMR is no longer dependent on t_{SCF}. As discussed above, TEM shows that the SCF layers, more than 15 Å thick, have become crystalline after annealing at 260 °C. Thus, the change in TMR with t_{SCF} is associated with an amorphous to crystalline transition of the SCF layer. It is reasonable to assume that the crystallization temperature depends on t_{SCF} and that thinner layers have higher crystallization temperatures, thereby accounting for the variation in the dependence of TMR with t_{SCF} on anneal temperature.

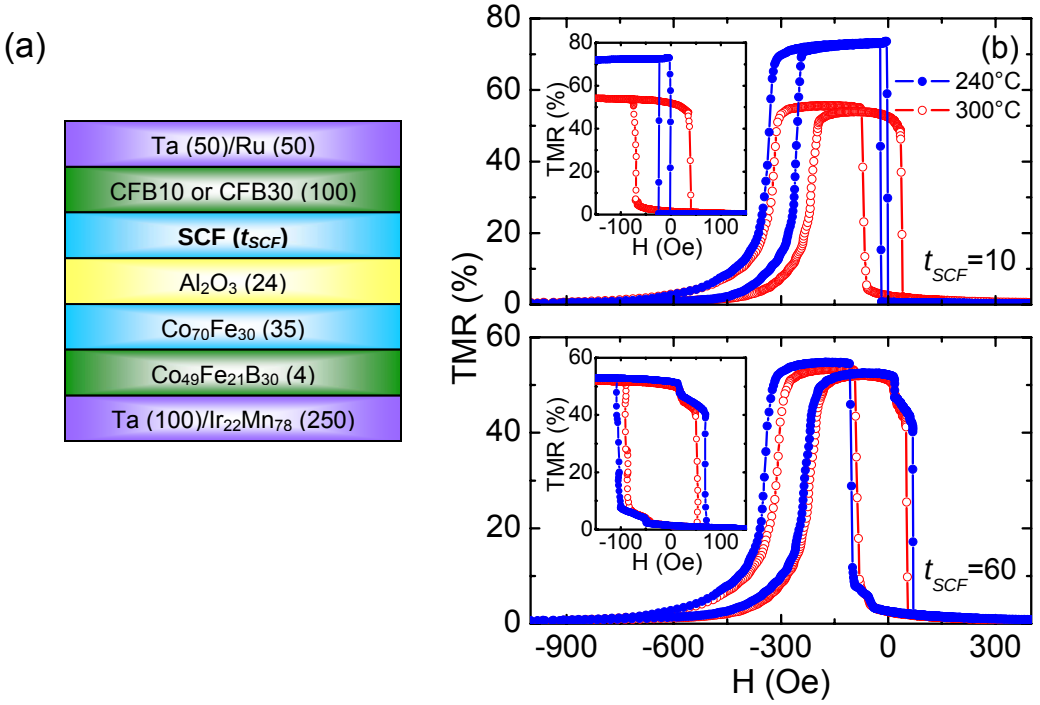

Fig. 3.3 (a) Schematic of the magnetic tunnel junction structure; (b) Major and minor (inset) TMR loops for CFB10 samples with t_{SCF} = 10 and 60 Å. Blue solid and red open circles denote results after the samples are annealed at 240 ℃ and 300 ℃, respectively.

In contrast, the dependence of TMR on t_{SCF} for the CFB30 samples varies little with T_A (Fig. 3.4). At each anneal temperature the TMR displays a peak at t_{SCF}~25 Å, and then decreases to a constant value for thicker SCF layers. This is consistent with the TEM results where the crystallinity of the SCF layer is not affected by annealing due to the high crystallization temperature of CFB30. Note that the initial increase in TMR with t_{SCF} is due to the low spin polarization of the high boron content CFB30 alloy and the initial islanded growth of the metal SCF layer on the alumina layer[24].

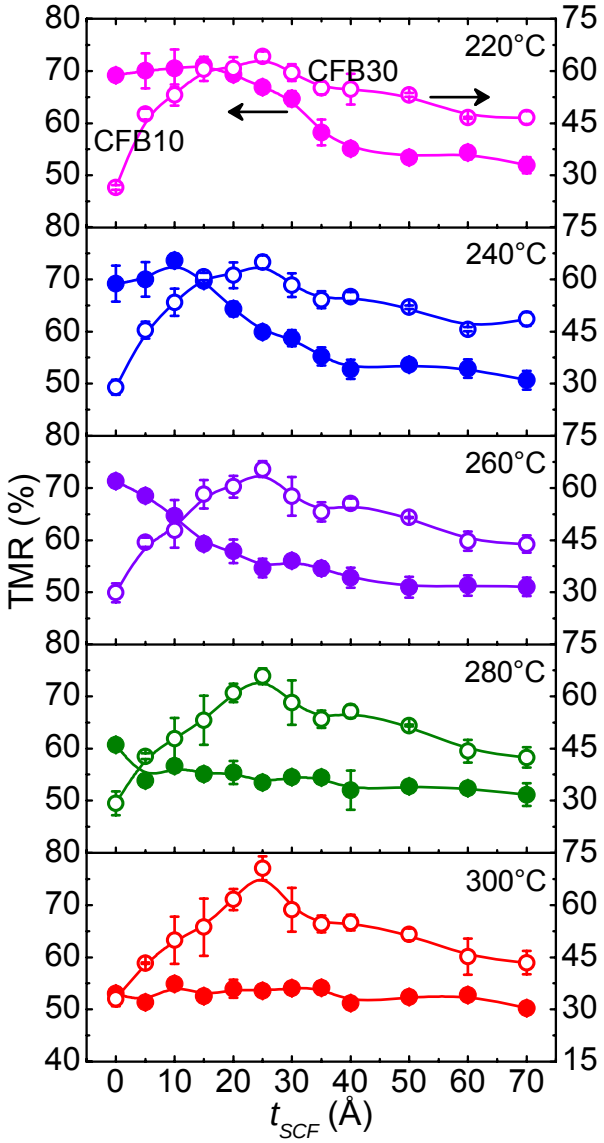

Fig. 3.4 Dependence of TMR on the SCF thickness at various anneal temperatures for CFB10 (solid circle) and CFB30 (open circle) samples.

The amorphous to crystalline transition of the SCF layer is manifested as a dramatic variation in H_c of CFB10 based MTJs, as shown in Fig. 3.5. When the SCF layer is thin and amorphous H_c is small and independent of its thickness (see data for T_A=220 °C). However, when thin SCF layers are made crystalline by thermal annealing, H_c is increased by almost an order of magnitude (after annealing at 300 °C) and becomes similar to that of very thick SCF layers, which are crystalline as deposited. It is well known that amorphous ferromagnetic materials are magnetically soft[25]. It is also well

established that H_c of thin ferromagnetic layers increases strongly with the diameter D of the crystalline grains (as ~D^6)[26-28]. Thus, the dependence of H_c on t_{SCF} and on T_A is readily understood from an amorphous to crystalline transition of the SCF layer and

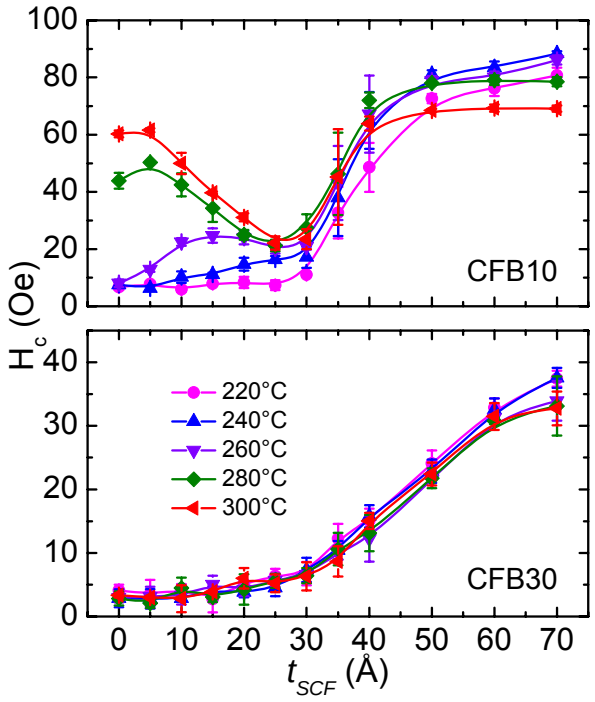

Fig. 3.5 Dependence of H_c on the SCF thickness at various anneal temperatures for CFB10 (upper) and CFB30 (lower) samples.

CFB10 layer. When the SCF layer is thin, and amorphous as deposited, the entire free layer crystallizes all at the same time leading to large grains whose size will be determined by nucleation and grain growth processes within the combination of the SCF and CFB10 layers. The underlying alumina layer will play no significant role since it is amorphous. As the SCF layer is increased in thickness and crystallizes, the grain size of the as-deposited SCF layer will be limited by its comparatively small thickness (20-30 Å). (Note that the grain size of thin film layers typically varies as the layer thickness). On annealing the CFB10 layer will crystallize but its grain size will be templated by that of the underlying crystalline SCF layer. As t_{SCF} is increased, its grain size and thus the grain size of the overlying CFB10 layer on crystallization will increase and thereby increase H_c.

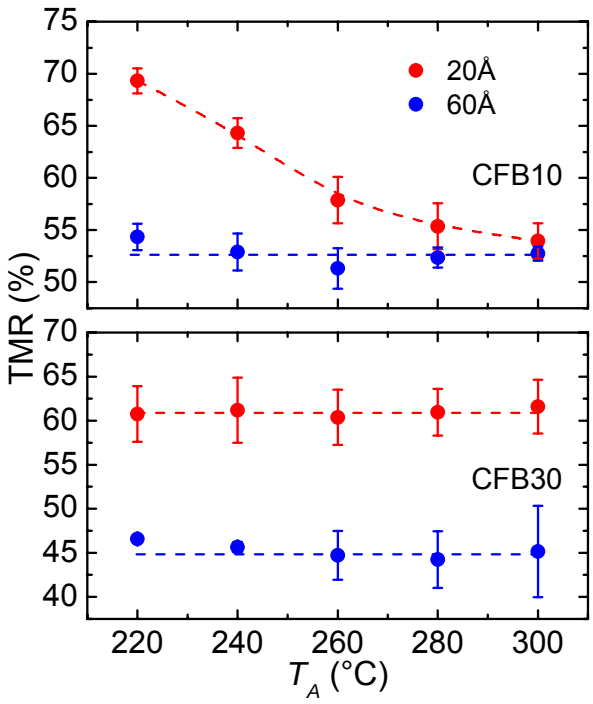

Fig. 3.6 Dependence of TMR on anneal temperature for CFB10 (upper) and CFB30 (lower) samples with t_{SCF} = 20 Å (red circle) and 60 Å (blue circle). The dashed lines are guides to the eye.

The dependence of H_c on t_{SCF} for MTJs with CFB30 layers is quite similar to that with CFB10 layers annealed at the lowest anneal temperature considered (220 °C) (Fig. 3.5). However, there is almost no change in the dependence of H_c on t_{SCF} on annealing up to 300 °C since the CFB30 alloy remains amorphous at these anneal temperatures. Thus, it can be concluded that the dependence of H_c on t_{SCF} is largely determined by the structure and grain size of the SCF layer, and that, at these comparatively low anneal temperatures, there is little grain growth during annealing.

An important question is whether the thickness of the SCF layer $t_{A\text{-}C}$ at which the amorphous to crystalline transition takes place is correlated with the thickness t_c at which the SCF layer becomes continuous[29]. t_c can be estimated from the SCF thickness at which the TMR reaches its maximum value (assuming that $t_c<t_{A\text{-}C}$). Thus, it can be estimated that t_c~20-25 Å for growth of SCF on Al_2O_3 but only ~10-15 Å for growth on $Co_{40}Fe_{40}B_{20}$ (see Section 3.3.3). Since $t_{A\text{-}C}$ is similar for SCF layers grown on insulating Al_2O_3 and metallic CFB layers, it can be concluded that $t_{A\text{-}C}$ is not simply related to t_c.

The dependence of TMR on T_A is summarized in Fig. 3.6 for free layers with representative thicknesses of 20 and 60 Å thick SCF layers for the CFB10 and CFB30 alloys, respectively. For both CFB alloys the TMR is much higher for the 20 Å amorphous as compared to the 60 Å crystalline SCF layer. Only for the thinner CFB10 alloy is any significant variation in TMR with T_A observed. In this case, the TMR decreases on annealing to the value found for thick SCF layers, which are crystalline as deposited.

3.3.2 Increased TSP from Amorphous CoFe

It has been discussed that when amorphous SCF layers are integrated into MTJs with amorphous alumina tunnel barriers, significantly higher TMR is observed compared to when these layers are crystalline. In this section, tunneling spin polarization (TSP) will be directly compared for both amorphous and crystalline CoFe alloys using superconducting tunneling spectroscopy (STS). It is well established that the magnetoresistance effect in MTJs derives from spin dependent tunneling, and is largely determined by TSP. The magnitude of TMR can be formulated in terms of the TSP for the two corresponding ferromagnetic (FM) electrodes, P_1 and P_2, as $TMR = 2P_1P_2/(1-P_1P_2)$ [30]. The TSP can be obtained by measuring the STS from superconductor/insulator/FM structures[31,32]. Indeed, it is found that the TSP is significantly enhanced for amorphous CoFe compared to its crystalline counterpart, consistent with the previous measurements of TMR.

Two sets of STS samples were deposited with the basic structure: thermally oxidized Si substrate/45 $Al_{95}Si_5$/32 Al_2O_3/t_{SCF} SCF /100 CFB10, or CFB30/50 Ta/50 Ru. The thickness t_{SCF} of the SCF layer varies from 0 to 70 Å. The superconducting layer was formed from 45-Å-thick $Al_{95}Si_5$, where a small amount of Si is added to increase the Al superconducting transition temperature[31]. The STS measurements were conducted at ~0.250 K in a magnetic field of 2 T applied in the film plane for as-deposited samples, and after annealing the samples at a series of temperatures from 220 °C to 300 °C. The annealing was carried out in vacuum (~5×10^{-8} *Torr*) in a 1 T

magnetic field applied along the easy axis which was set by a small in-plane magnetic field during film deposition.

In the STS measurement, the quasi-particle density of states (DOS) in the superconducting $Al_{95}Si_5$ is Zeeman-split into spin-polarized states in the presence of a large magnetic field, thereby serving as an analyzer for the spin-polarized current. By detailed fitting of the conductance versus voltage curves, the TSP can be extracted with high precision[33]. Typical STS data of the tunnel junctions, 45 $Al_{95}Si_5$/32 Al_2O_3/t_{SCF} SCF/100 CFB10/50 Ta/50 Ru, are shown in Fig. 3.7 for t_{SCF} = 25 and 70 Å. Four pronounced peaks, labeled as σ_1, σ_2, σ_3, and σ_4, are observed in each curve, which originate from contributions of the spin-up (σ_1, σ_3) and spin-down (σ_2, σ_4) states respectively. A rough estimate of the TSP value can be derived from the following equation[32], $P = \frac{(\sigma_4 - \sigma_2) - (\sigma_1 - \sigma_3)}{(\sigma_4 - \sigma_2) + (\sigma_1 - \sigma_3)}$. Thus, from the relative magnitudes of σ_1, σ_2, σ_3, and σ_4, it can be clearly seen that: (i) for the as-deposited samples, a 25 Å thick SCF layer gives significantly higher TSP than that of a 70 Å thickness, i.e. the amorphous SCF has enhanced TSP compared to the crystalline SCF; (ii) upon annealing at 300 °C, the TSP values of both samples decrease and become similar to each other. More accurate TSP values can be obtained by fitting the data, taking into account orbital depairing and spin-orbit scattering in the $Al_{95}Si_5$ superconductor. As shown by the solid lines in Fig. 3.7, excellent agreement with experiments is achieved using Maki's theory[34], The TSP of the amorphous 25 Å SCF is 55.2% whereas the TSP of the crystalline 70 Å SCF is only 48.0%, for the as-deposited samples. By contrast, the TSP values of the two samples become comparable after annealing at 300 °C, namely, 39.1% and 36.2%, respectively.

The detailed dependence of TSP on t_{SCF} at various anneal temperatures for both the CFB10 and CFB30 samples are depicted in Fig. 3.8. For the CFB10 samples, the TSP of the as-deposited devices shows a peak around t_{SCF} ~25 Å, and decreases to a significantly lower value for thicker layers. After annealing at elevated temperatures, the position of the peak moves to thinner SCF layers, and almost disappears after the 300 °C anneal, resulting in a slight dependence of TSP on t_{SCF}. The t_{SCF} dependence of

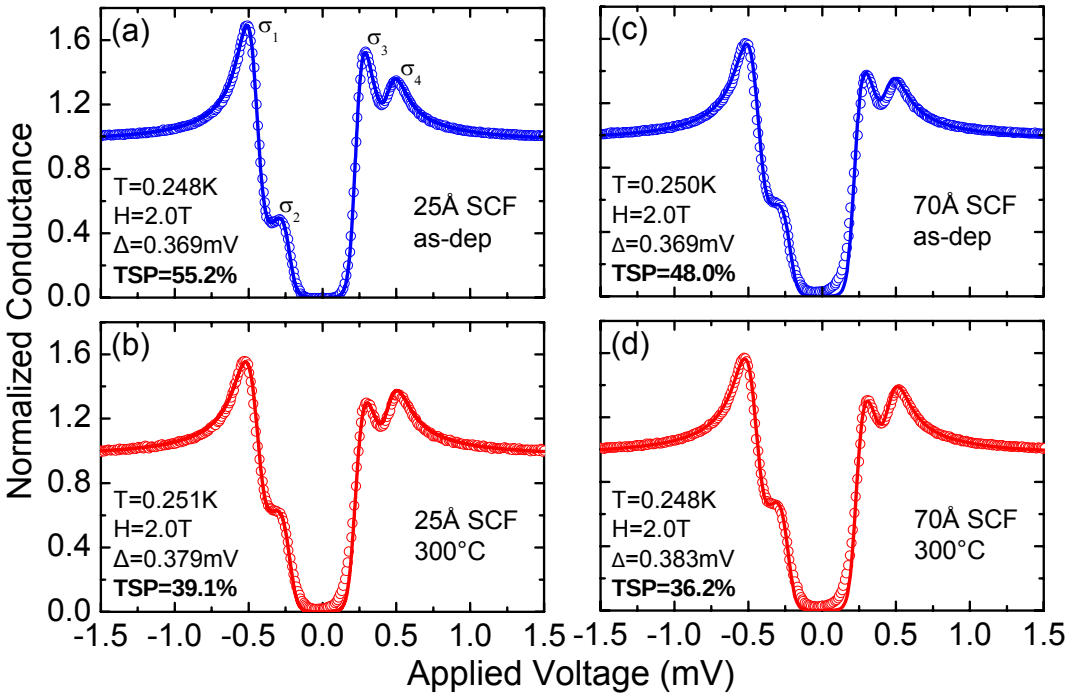

Fig. 3.7 Typical experimental data from superconducting-tunneling-spectroscopy from the tunnel junctions with structure, 45 $Al_{95}Si_5$/32 Al_2O_3/t_{SCF} SCF/100 CFB10/50 Ta/50 Ru, at T ~ 0.250 K and H = 2.0 T; (a) t_{SCF} = 25 Å, as-deposited; (b) t_{SCF} = 25 Å, annealed at 300 ℃; (c) t_{SCF} = 70 Å, as-deposited; (d) t_{SCF} = 70 Å, annealed at 300 ℃. Open circles are experimental data and solid lines are fits. Δ is the fitted $Al_{95}Si_5$ superconducting energy gap.

the TSP of the as-deposited CFB30 samples shows a similar peak as that of the as-deposited CFB10 samples. However, their anneal temperature dependences are distinctly different from each other: the t_{SCF} dependence of the TSP hardly changes for the CFB30 samples, even after annealing at 300 °C. This is related to the different crystallization temperatures of the CFB10 and CFB30 layers same as the case in the TMR results, although the magnitude of the TSP is diminished. Similarly, the variation of the t_{SCF} dependence of TSP with anneal temperature is associated with an amorphous to crystalline transition of the SCF layer and the CFB10 layer. On the other hand, CFB30 has a crystalline temperature higher than 300 °C. As a result, the SCF layers remain in their as-deposited states for the anneal temperature range in the experiments. Consequently, the overall dependence of the TSP on t_{SCF} for the CFB30 samples varies little with anneal temperature. The TSP results are consistent with the TMR observed in MTJs incorporating either amorphous or crystalline SCF layers in the electrodes.

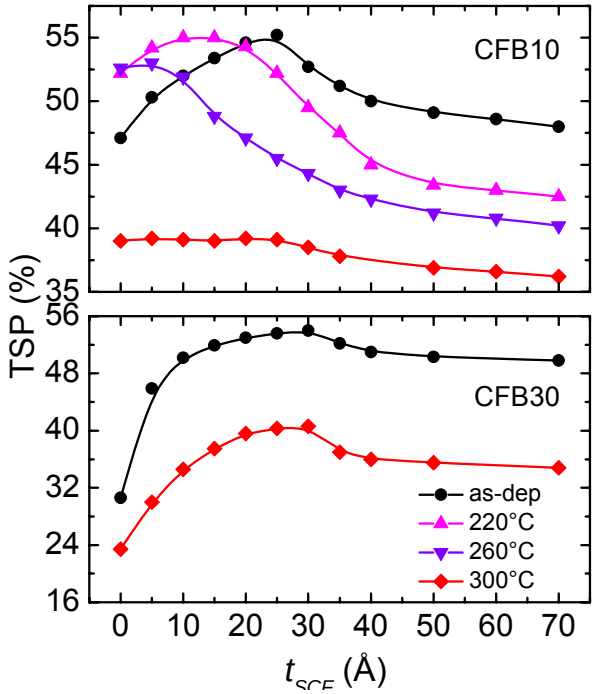

Fig. 3.8 Dependence of TSP on the SCF thickness at various anneal temperatures for both CFB10 and CFB30 samples.

Contrary to an increase in TMR usually observed in annealed MTJs, the TSP decreases upon annealing. The origin of such a decrease was investigated using both normal and inverted STS structures[31], i.e. 45 $Al_{95}Si_5$/32 Al_2O_3/25 SCF/100 CFB30/50 Ta/50 Ru and 100 Ta/250 $Ir_{24}Mn_{76}$/4 $Co_{49}Fe_{21}B_{30}$/35 $Co_{70}Fe_{30}$/28 Al_2O_3/40 $Al_{95}Si_5$/33 MgO, respectively. The alumina barriers were prepared in each case by reactive sputtering from a metallic aluminum target but by using different Ar-O_2 gas mixtures (O_2 concentrations of 7%, 9%, and 11%) and, in some cases, a post-deposition atomic oxygen treatment (for 30 and 60 seconds). The anneal temperature dependence of the STS results is shown in Fig. 3.9. In general, the TSP shows better thermal stability when the $Al_{95}Si_5$ layer is grown on top of ("inverted") than when underneath ("normal") the tunnel barrier. Note that the bottom 35 Å $Co_{70}Fe_{30}$ is crystalline in the inverted structure, giving rise to a lower TSP value than that of the amorphous 25 Å SCF in the normal structure. Treatment with atomic oxygen gives rise to much improved thermal stability for the normal structure, whereby the TSP initially increases upon annealing at modest temperatures. On the other hand, the atomic oxygen treatment hardly affects the thermal stability of the TSP of the inverted structure.

When the barrier is formed by reactive sputtering in argon-oxygen gas mixtures with high oxygen content (9 and 11%), the resistance increases much faster on annealing compared to samples with barriers made with sputtering gases with optimal oxygen content (~7%), by contrast, when the surface of the barrier made with the lower oxygen content sputtering gas is subsequently oxidized by atomic oxygen the resistance increases on annealing at about the same rate as the barrier without the surface atomic oxygen treatment. Thus it can be concluded that excess oxygen contained within the barrier is redistributed on annealing, resulting in a thicker tunnel barrier. The thermal stability of the STS samples is likely related to the interplay between the $Al_{95}Si_5$ electrode and the Al_2O_3 barrier. In the normal structure, the $Al_{95}Si_5$ layer is very rough,

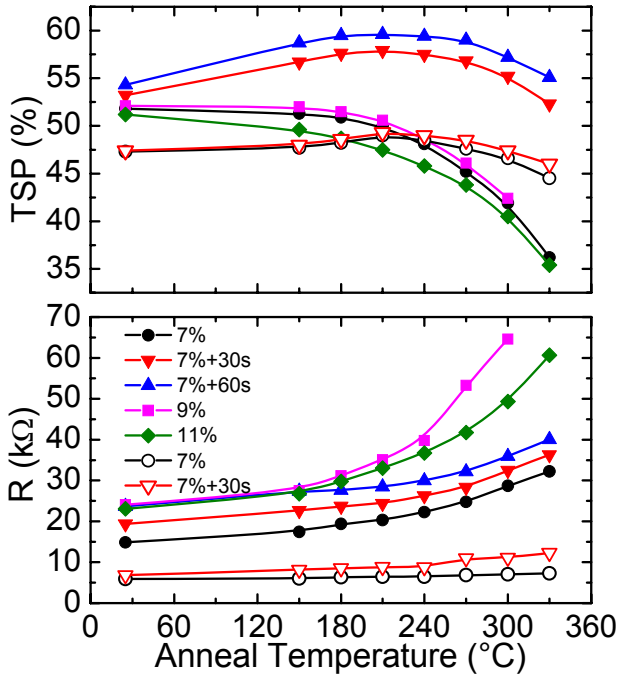

Fig. 3.9 Anneal temperature dependence of TSP and resistance for both normal (solid symbols, 45 $Al_{95}Si_5$/32 Al_2O_3/25 SCF/100 CFB30/50 Ta/50 Ru) and inverted (open symbols, 100 Ta/250 $Ir_{24}Mn_{76}$/4 $Co_{49}Fe_{21}B_{30}$/35 $Co_{70}Fe_{30}$/28 Al_2O_3/40 $Al_{95}Si_5$/33 MgO) STS samples. The tunnel barrier Al_2O_3 was grown by reactive sputtering in an O_2-Ar mixture with (triangles) or without an additional atomic oxygen treatment (30 or 60 seconds) after deposition. Oxygen concentrations in the sputter gas mixture of 7% (circles and triangles), 9% (square), and 11% (diamond) were used.

so that Al_2O_3 barriers grown on this layer are also rough (as shown by atomic force microscopy (AFM) measurements in Fig. 3.10) and tend to have more defects which

can facilitate oxygen redistribution upon annealing. During annealing the bottom $Al_{95}Si_5$ will absorb oxygen from the Al_2O_3 barrier and form a thicker barrier, giving rise to a pronounced increase of the sample resistance upon annealing (Fig. 3.9). The possibility that the resistance increase could be due to the formation of boron oxide from the diffusion of boron on annealing was ruled out by EELS measurements. No significant boron diffusion was observed for anneal treatments up to 300 °C.

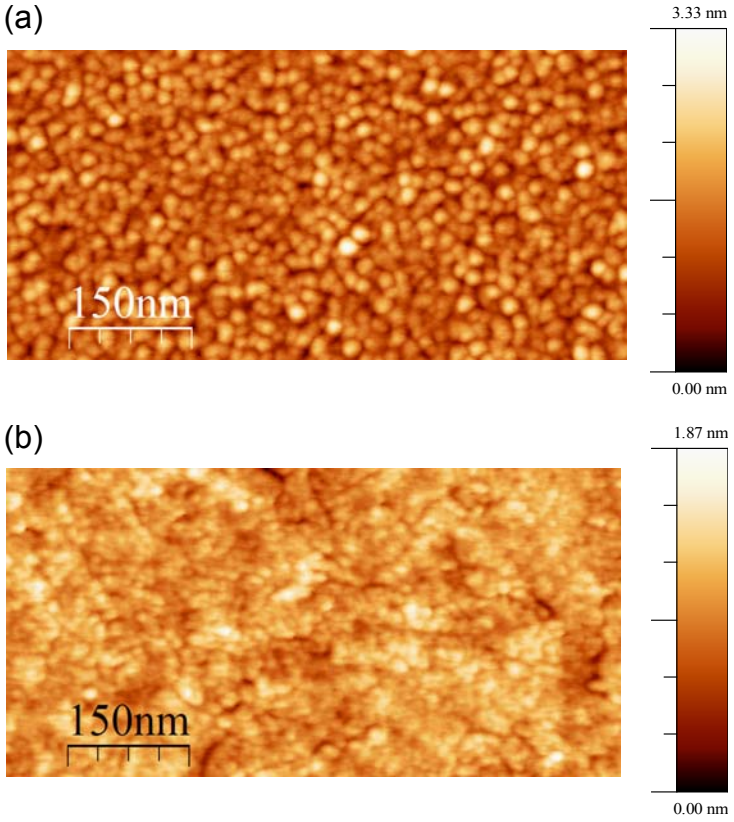

Fig. 3.10 Atomic force microscopy images (AFM) for Al_2O_3 barriers (a) in normal structure, 45 $Al_{95}Si_5$/32 Al_2O_3; (b) in inverted structure, 100 Ta/250 $Ir_{22}Mn_{78}$/6 $Co_{40}Fe_{40}B_{20}$/35 $Co_{70}Fe_{30}$/32 Al_2O_3. Both the barriers were deposited in the optimal condition with an Ar-O_2 (93/7) mixture. Clear grains with RMS ~ 0.395 nm in the normal structure and much smoother surface with RMS ~ 0.190 nm in the inverted structure were observed.

The supposed redistribution of oxygen from the barrier to the AlSi on annealing could lead to a lack of oxygen at the Al_2O_3/CoFe interface and thereby account for the observed decrease of the TSP at high annealing temperatures. Thus, adding extra oxygen at the Al_2O_3/CoFe interface by a post-deposition atomic oxygen treatment would make the TSP more thermally stable. This treatment is not possible in the inverted structure. Rather, adding oxygen at the $Al_2O_3/Al_{95}Si_5$ interface can hardly

affect the TSP but can account for the increase of resistance upon annealing. Moreover, AFM measurements show that the barriers in the inverted structures are considerably smoother than those of the normal structures due to their growth on smooth underlayers (Fig. 3.10). In addition to this, the alumina isolation pads around the tunnel barrier used only in the inverted structures may also help to improve the thermal stability of the TSP of these samples[31].

3.3.3 When CoFe beneath Al_2O_3

So far, the amorphous-to-crystalline transition of SCF layers with their thicknesses was only investigated in structures where the SCF layers were grown on top of the Al_2O_3 oxide layer. The interpretation of this transition and the consequent TMR enhancement from amorphous SCF layer, however, is complicated by the fact that the thin CoFe film does not wet the Al_2O_3 barrier. As a result, the CoFe initially grows as isolated islands on Al_2O_3 and becomes continuous only after its thickness reaches ~20-25 Å, coincident with the critical thickness for the amorphous to crystalline transition. Therefore, it is difficult to conclude whether the observed TMR increase is related to the continuity of the CoFe film or the electronic structure of the CoFe in its amorphous phase.

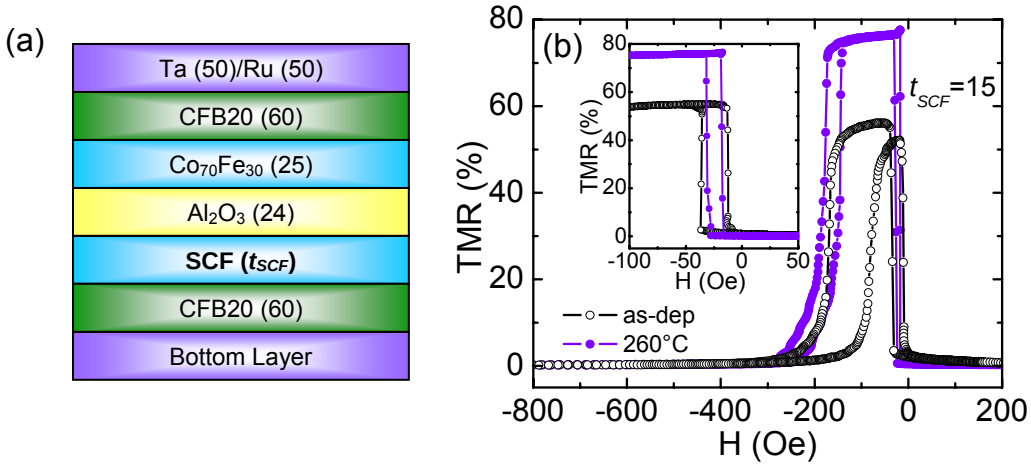

Fig. 3.11 (a) Schematic diagram of the magnetic tunnel junction structure with the SCF layer underneath the tunnel barrier; (b) Major and minor (inset) TMR loops for t_{SCF} = 15 Å. Black open and violet solid circles denote loops for an as-deposited device and for the same device after an anneal at 260 ℃, respectively.

In this section, it is reported that the tunneling magnetoresistance is significantly higher when a thin amorphous CoFe layer is deposited underneath an Al_2O_3 tunnel barrier. This geometry allows for the growth of continuous layers of CoFe even when just a few ångstroms thick. Magnetotransport measurements in combination with cross-sectional transmission electron microscopy indicate that the TMR increase is related to the crystallinity rather than the continuity of the CoFe film.

The thin film structures were deposited with the same techniques as previous work. The fabricated MTJs had the following structures (from bottom to top): 100 Ta/250 $Ir_{22}Mn_{78}$/4 $Co_{49}Fe_{21}B_{30}$/5 $Co_{70}Fe_{30}$/60 CFB20/t_{SCF} SCF/24 Al_2O_3/25 $Co_{70}Fe_{30}$/60 CFB20 /50 Ta/50 Ru (Fig. 3.11), where CFB20 denotes an amorphous $Co_{40}Fe_{40}B_{20}$ layer, and t_{SCF} is the thickness of the SCF layer. The TMR measurements were conducted at room temperature. Typical resistance vs. magnetic field loops are plotted in Fig. 3.11 for the sample with t_{SCF} = 15 Å, both as-deposited and after an anneal at 260 °C. The anneal significantly improves the exchange coupling between the bottom magnetic layers and the IrMn layer, giving rise to a very high TMR of nearly 80%. The detailed SCF thickness dependence of the TMR at various anneal temperatures is shown in Fig. 3.12. A similar stepwise feature is clearly seen in each TMR vs. t_{SCF} curve. The TMR values are considerably higher when t_{SCF} < 20-25 Å than when t_{SCF} > 35-40 Å, with the transition from high to low TMR values occuring at t_{SCF} ~ 30 Å. Note that the slightly lower TMR values at t_{SCF} = 0 result from non-existing coverage of the SCF layer on the bottom CFB20 layer, which has a smaller tunneling spin polarization compared to CoFe. On the other hand, the maximum TMR value obtained at t_{SCF} ~ 15 Å indicates that the SCF layer becomes continuous by at least this thickness. Therefore, the enhanced TMR for t_{SCF} < ~ 20-25 Å cannot be explained by the continuity of the SCF layer.

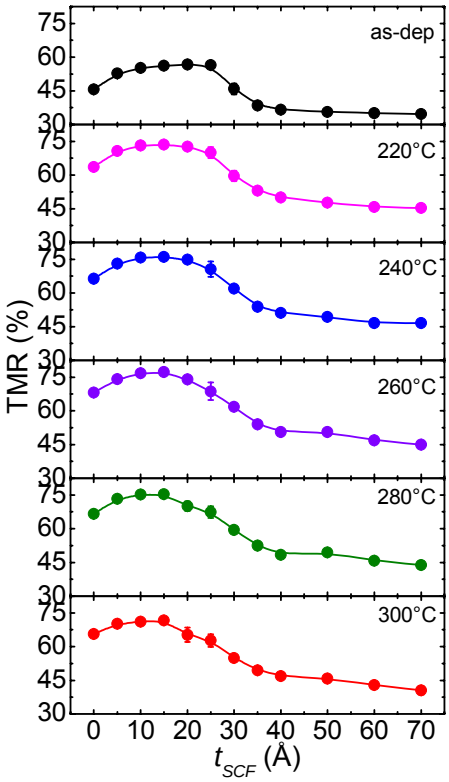

Fig. 3.12 Dependence of TMR on the SCF thickness at various anneal temperatures for the samples with CFB20 beneath Al_2O_3.

High-resolution cross-section TEM was also used to study the structure of the SCF layer as a function of its thickness in a single multilayered sample with a structure of 100 Ta/250 $Ir_{22}Mn_{78}$/4 $Co_{49}Fe_{21}B_{30}$/5 $Co_{70}Fe_{30}$/[60 CFB20/t_{SCF} SCF/44 Al_2O_3]$_6$. The SCF layers had thicknesses of t_{SCF} = 10, 15, 20, 30, 40 and 50 Å. As clearly shown in Fig. 3.13(a), the SCF layer is amorphous when t_{SCF} is smaller than ~20-30 Å and is crystalline for thicker SCF layers. Annealing at 260 °C does not induce any significant change in the crystallinity of the SCF layers (Fig. 3.13(b)). The amorphous to crystalline transition of the SCF layer correlates very well with the thickness dependence of the TMR, implying that the amorphization of the SCF layer is the origin of the higher TMR values.

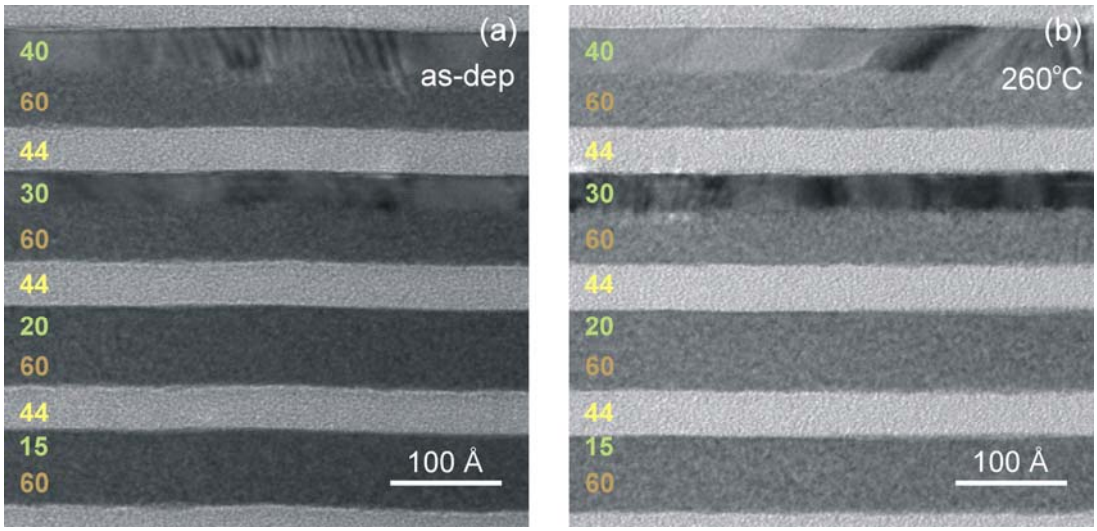

Fig. 3.13 High-resolution cross-section transmission electron microscopy images for (a) 100 Ta/250 $Ir_{22}Mn_{78}$/4 $Co_{49}Fe_{21}B_{30}$/5 $Co_{70}Fe_{30}$/[60 CFB20/t_{SCF} SCF/44 Al_2O_3]$_6$ with t_{SCF} =10, 15, 20, 30,40 and 50 Å (10 and 50 not shown); (b) same sample as in (a) after an anneal at 260 ℃. In both images, the thicknesses of SCF, Al_2O_3, and CFB20 are labeled in green, yellow, and orange, respectively.

3.4 DISCUSSION

3.4.1 X-Ray Emission Spectroscopy

X-ray emission spectroscopy (XES) is a powerful experimental technique for determining detailed electronic structure of materials. It provides a means of probing the partial occupied density of electronic states of a material, which is element-specific and site-specific[35]. Emission spectroscopy can take the form of either resonant inelastic x-ray emission spectroscopy (RIXS) or non-resonant x-ray emission spectroscopy (NXES). Both methods are two-step processes involving the photonic excitation of a core level electron, and the measurement of the fluorescence that occurs as the electron relaxes into a lower-energy state. The differences between resonant and non-resonant excitation arise from the state of the atom before fluorescence occurs or x-ray is emitted. In resonant excitation, the core electron is promoted to a bound state in the conduction band. Non-resonant excitation occurs when the incoming radiation promotes a core electron to the continuum. When a core hole is created in this way, it is

possible for it to be refilled through one of several different decay paths. Because the core hole is refilled from the sample's high-energy free states, the decay and emission processes must be treated as separate dipole transitions. This is in contrast with RIXS, where the events are coupled, and must be treated as a single scattering process. In the experiments, XES spectra were recorded by the use of threshold excitation at Fermi energy (E_F), whose energy was first determined by tuning the incident x-ray energy to the absorption maximum for the Fe and Co L_3 edges, respectively. These $2p_{3/2}$ binding energies are 707 eV for Fe and 778 eV for Co, respectively[36]. Then the intensity versus energy of the emitted photons was measured using an x-ray spectrometer.

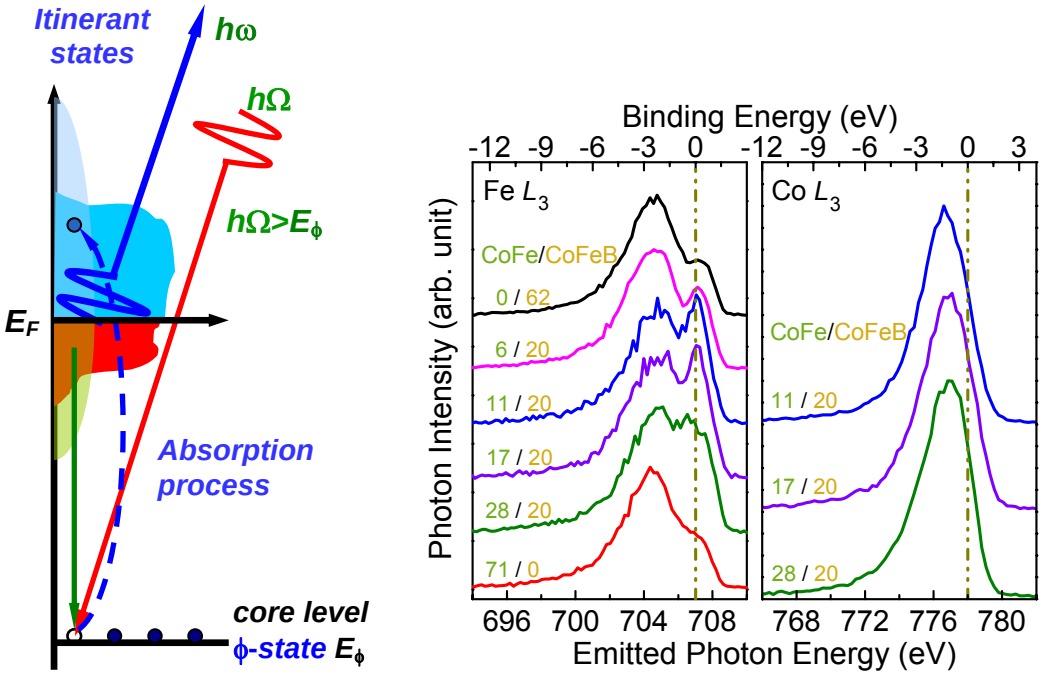

Fig. 3.14 Fe L_3 and Co L_3 XES spectra as a function of the SCF thickness for 50 Ta/18 Al_2O_3/[t_{SCF} SCF/20 CFB20], or 71 $Co_{70}Fe_{30}$, or 62 CFB20/10 Al_2O_3. The thicknesses of CoFe (CoFeB) are shown in green (orange). The Fe and Co $2p_{3/2}$ binding energies relative to the Fermi level are taken to be 707 eV and 778 eV, as indicated by the dark-yellow dashed-dotted lines.

To explore whether the SCF/alumina interface electronic structure might be responsible for the enhanced TMR, XES was used to probe the density of filled electronic states at the buried Al_2O_3/SCF interface[37] in specially prepared structures of the form, 50 Ta/18 Al_2O_3/t_{SCF} SCF/20 CFB20 (=$Co_{56}Fe_{24}B_{20}$)/10 Al_2O_3 in which t_{SCF} was varied across a single wafer. The measured spectra are shown in Fig. 3.14(b),

where the valence band binding energies relative to E_F are indicated. The broad, featureless Co spectra are similar to those previously found in bulk Co and in Co/Cu multilayers[37]. However, the Fe spectra show a feature near E_F whose intensity is significantly increased in the thickness range where the SCF is observed to be amorphous. Moreover, since the intensity of this feature is strongest for the thinnest SCF layers and this feature is weak in thick CFB20 layers, it can be concluded that this feature results from modifications to the electronic structure at the Al_2O_3/SCF interface.

3.4.2 Band Structure Calculations

To understand whether the higher TMR of the amorphous SCF layers arises from changes in the bulk electronic structure of this layer, density functional electronic states were calculated for both crystalline (a *bcc* random solid solution) and amorphous structures of $Co_{70}F_{30}$. These calculations reveal substantial differences in the band structure of crystalline and glassy forms of *bulk* Co-Fe alloys, but a *decreased* spin polarization of the electrons at the Fermi energy, inconsistent with experimental results.

In order to understand the impact of the crystallinity of the CoFe electrode on its electronic structure and consequently its spin polarization, the density functional electronic states of $Co_{70}F_{30}$ in two structures, *bcc* random solid solution and amorphous (i.e. a glass), were calculated using the Projector Augmented Wave[38,39] method as implemented in the Vienna *Ab-initio* Simulation Package (VASP)[40]. The density functional was treated in the Generalized Gradient Approximation (GGA)[41] and all calculations were spin polarized with collinear moments. The *bcc* structure was created by random placement of 29 Fe and 67 Co atoms on *bcc* lattice sites (3×3×3 conventional *fcc* cells with large Bain strain). The atomic positions, cell volume, and cell shape were relaxed to their local meta-stable equilibrium values using a conjugate gradient method. The energy and forces in the relaxation process were computed with a single k-point at Γ point. Construction of the amorphous structure began with random packing of hard spheres with a packing ratio of 0.30. The structure was equilibrated with VASP molecular dynamics (MD) for 2 ps at an expanded volume (about 8% larger than equilibrium) at a temperature of 2000 K. The sample was then homogeneously

compressed to create five samples with higher densities that were then partially equilibrated by MD for 0.4 ps. The energies of these samples were used to determine the equilibrium volume at 2000 K. The sample nearest the equilibrium volume was scaled to the equilibrium volume and equilibrated for another 2 ps. Equilibration was followed by an instantaneous quench to zero temperature. All the coordinates of the quenched sample (cell size, cell shape, and atomic positions) were then relaxed to values that locally minimized the energy. Similar procedures have been shown to yield glass structures for Fe based glasses that compare well to measured partial pair distribution functions[42,43].

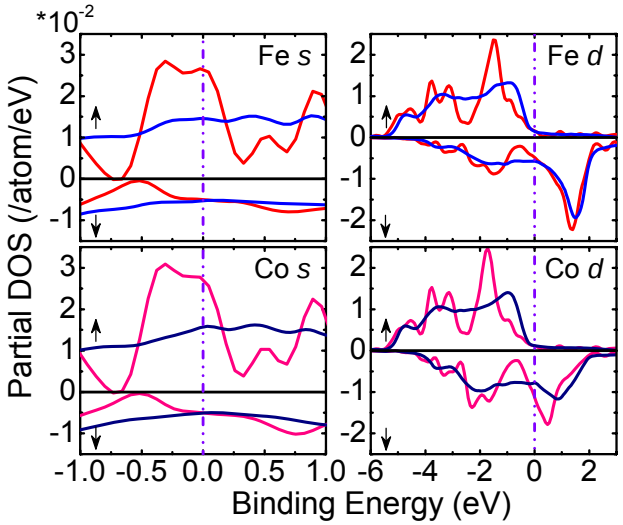

Fig. 3.15 Spin-resolved s- and d- partial density of states for Fe and Co in amorphous (blue and navy) and bcc crystalline (red and pink) $Co_{70}Fe_{30}$ alloy structures.

The k-point-converged densities of electronic states that were projected into angular momentum components on atomic spheres are depicted in Fig. 3.15. Both the *s*- and *d*-states of the CoFe alloy experience significant changes in band structure and partial DOS when it is amorphized. The distinctive features in the energy dependence of the *s*- and *d*- partial DOS for *bcc* CoFe are washed out in the amorphous state[44,45] and the net spin polarization of the DOS at E_F is slightly reduced. Therefore, the observed TMR increase for an amorphous CoFe electrode cannot be accounted for by a larger spin polarization of the *s*-electron DOS at the Fermi level, contrary to what has been reported by Paluskar *et al*. for amorphous CoFeB[15].

As an aside, it is revealed that the fluctuations in the moments of the Fe atoms from site to site are substantially increased in the amorphous structure as compared to the crystalline structure[45], as shown in Fig. 3.16. The Co atom moments, which vary little in the crystalline structure, also show significant site-to-site variations in the amorphous structure but these are smaller than those of the Fe atoms. This demonstrates the greater sensitivity of the Fe moment to its local chemical and structural environment.

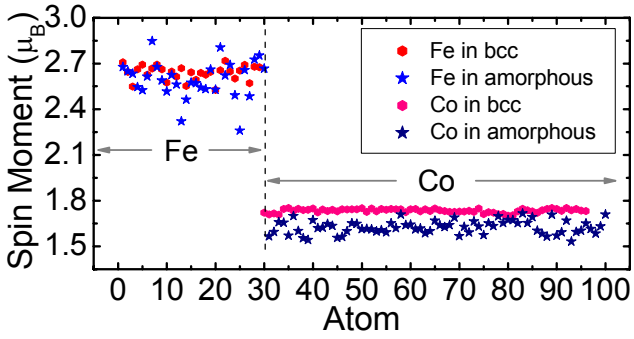

Fig. 3.16 Spin moment of each atom in the computational ensemble for amorphous or bcc crystalline $Co_{70}Fe_{30}$. The horizontal axis indicates the label of the individual Fe and Co atoms in the calculations.

3.4.3 Explanation

Small changes in the atomic structure at the interface between a tunnel barrier and the magnetic electrodes can give rise to significant changes in the interface density of states and hence the spin-dependent tunneling conductance[7]. In a simple tight-binding model, spin dependent tunneling in MTJs is largely determined by the atomic structure and bonding at the interface, via the interplay between the on-site atomic energies and bonding strength[7]. Amorphizing the normally crystalline CoFe alloy can introduce significant changes in both electronic and atomic structures due to atomic relaxation. The hopping integral with nearest-neighbors, on-site potential, and bonding strength with oxygen can all be dramatically modified for interfacial atoms. Therefore, it may not be surprising that the TMR and TSP values are significantly influenced by whether the CoFe is amorphous or crystalline. Moreover, the XES strongly indicates both that the interface electronic structure is significantly altered compared to the bulk and that the Fe states play a dominant role. An additional peak is observed in the Fe spectrum,

whose intensity is maximized for thicknesses at which the SCF layer is amorphous. On the other hand, the Co partial DOS does not show a significant dependence on the SCF thickness. The strong dependence of the partial DOS of the Fe *3d* band on the thickness of the SCF layer is consistent with the notion that Fe is more easily affected by structural changes of the CoFe, as revealed by *ab initio* calculations in Fig. 3.16. Material variations have explored in the composition of the SCF layer from pure Co to pure Fe and it is found that the highest TMR values for amorphous SCF layers with compositions is near $Co_{70}Fe_{30}$. It is believed that the chemical bonding at the SCF interface with alumina is important[6]. Stronger bonding with oxygen is expected for Fe as compared to Co at the alumina interface from bond energy considerations, and stronger bonding with oxygen can also be expected at the interface for amorphous CoFe since atoms are no longer restricted by the crystalline order, which helps spin dependent tunneling and increases the tunneling spin polarization[6]. It is reasonable for us to speculate that this difference could be accentuated when the ferromagnetic electrode is in an amorphous compared to a crystalline state due to atomic relaxation. Therefore, it is proposed that the enhanced TMR may rather be attributed to changes at the SCF/Al_2O_3 interface upon the CoFe amorphization.

3.5 SUMMARY

Using cross-section transmission electron microscopy it is shown that films of CoFe alloys, sandwiched between two conventional amorphous materials, undergo an amorphous-to-crystalline transition at a critical thickness of ~25-30 Å. When these amorphous layers are integrated into magnetic tunnel junctions with amorphous alumina tunnel barriers, significantly higher tunneling magnetoresistance and tunneling spin polarization are found compared to when these layers are made crystalline, e.g. by heating or by thickening them. *Ab initio* electronic structure calculations show substantial differences in the band structure of crystalline and amorphous forms of *bulk* CoFe alloys. However, the calculated spin polarization at the Fermi energy is reduced when CoFe is amorphous, contrary to an explanation of the experimental observation in terms of the bulk electronic states in *bcc* and amorphous CoFe. The calculations also reveal the greater sensitivity of the Fe moment to its local chemical and structural environment. Indeed, x-ray emission spectroscopy shows a significant increase in the Fe, but not the Co, 3*d* density of states at the Fermi energy for thin amorphous CoFe layers. Therefore, it is postulated that the increased tunneling magnetoresistance is likely due to changes in interfacial bonding at the alumina/CoFe interface caused by amorphization induced atomic relaxation.

REFERENCES:

[1] T. Miyazaki and N. Tezuka, "Giant magnetic tunneling effect in Fe/Al_2O_3/Fe junction," J. Magn. Magn. Mater. **139**, L231 (1995).

[2] J. S. Moodera, L. R. Kinder, T. M. Wong, and R. Meservey, "Large Magnetoresistance at Room Temperature in Ferromagnetic Thin Film Tunnel Junctions," Phys. Rev. Lett. **74**, 3273 (1995).

[3] S. S. P. Parkin, C. Kaiser, A. F. Panchula, P. Rice, M. G. Samant, S.-H. Yang, and B. Hughes, "Giant tunneling magnetoresistance at room temperature with MgO (100) tunnel barriers," Nature Materials **3**, 862 (2004).

[4] E. Y. Tsymbal, O. N. Mryasov, and P. R. LeClair, "Spin-dependent tunnelling in magnetic tunnel junctions," J. Phys. C: Condens. Matter **15**, R109 (2003).

[5] S. Parkin, X. Jiang, C. Kaiser, A. Panchula, K. Roche, and M. Samant, "Magnetically Engineered Spintronic Sensors and Memory," Proc. IEEE **91**, 661 (2003).

[6] C. Kaiser, S. van Dijken, S.-H. Yang, H. Yang, and S. S. P. Parkin, "Role of Tunneling Matrix Elements in Determining the Magnitude of the Tunneling Spin Polarization of 3d Transition Metal Ferromagnetic Alloys," Phys. Rev. Lett. **94**, 247203 (2005).

[7] E. Y. Tsymbal, K. D. Belashchenko, J. P. Velev, S. S. Jaswal, M. v. Schilfgaarde, I. I. Oleynik, and D. A. Stewart, "Interface effects in spin-dependent tunneling," Prog. Mater. Sci. **52**, 401 (2007).

[8] S. Yuasa, E. T. T. Sato, Y. Suzuki, H. Yamamori, K. Ando, and T. Katayama, "Magnetic tunnel junctions with single-crystal electrodes: A crystal anisotropy of tunnel magneto-resistance," Europhys. Lett. **52**, 344 (2000).

[9] P. LeClair, J. T. Kohlhepp, C. H. van de Vin, H. Wieldraaijer, H. J. M. Swagten, W. J. M. de Jonge, A. H. Davis, J. M. MacLaren, J. S. Moodera, and R. Jansen, "Band Structure and Density of States Effects in Co-Based Magnetic Tunnel Junctions," Phys. Rev. Lett. **88**, 107201 (2002).

[10] D. Wang, C. Nordman, J. M. Daughton, Z. Qian, and J. Fink, "70% TMR at Room Temperature for SDT Sandwich Junctions With CoFeB as Free and Reference Layers," IEEE Trans. Magn. **40**, 2269 (2004).

[11] D. D. Djayaprawira, K. Tsunekawa, M. Nagai, H. Maehara, S. Yamagata, N. Watanabe, S. Yuasa, Y. Suzuki, and K. Ando, "230% room-temperature magnetoresistance in CoFeB/MgO/CoFeB magnetic tunnel junctions," Appl. Phys. Lett. **86**, 092502 (2005).

[12] S. Ikeda, J. Hayakawa, Y. Ashizawa, Y. M. Lee, K. Miura, H. Hasegawa, M. Tsunoda, F. Matsukura, and H. Ohno, "Tunnel magnetoresistance of 604% at 300K by suppression of Ta diffusion in CoFeB/MgO/CoFeB pseudo-spin-valves annealed at high temperature," Appl. Phys. Lett. **93**, 082508 (2008).

[13] S. Yuasa, T. Nagahama, A. Fukushima, Y. Suzuki, and K. Ando, "Giant room-temperature magnetoresistance in single-crystal Fe/MgO/Fe magnetic tunnel junctions," Nature Materials **3**, 868 (2004).

[14] S. X. Huang, T. Y. Chen, and C. L. Chien, "Spin polarization of amorphous CoFeB determined by point-contact Andreev reflection," Appl. Phys. Lett. **92**, 242509 (2008).

[15] P. V. Paluskar, J. J. Attema, G. A. d. Wijs, S. Fiddy, E. Snoeck, J. T. Kohlhepp, H. J. M. Swagten, R. A. d. Groot, and B. Koopmans, "Spin Tunneling in Junctions with Disordered Ferromagnets," Phys. Rev. Lett. **100**, 057205 (2008).

[16] H. A. Davies and M. R. J. Gibbs, "Amorphous Alloys," Handbook of Magnetism and Advanced Magnetic Materials, Edited by Helmut Kronmuller and Stuart Parkin (Willey, 2007) p. 1861.

[17] A. L. Greer, "Metallic Glasses," Science **267**, 1947 (1995).

[18] EELS studies were carried out using a JEOL 2010F STEM (200 keV field emission electron gun; energy resolution ~1.2 eV) using a high spatial resolution (~5 Å diameter) probe and a Gatan Infina 1000 spectrometer. No evidence for B diffusion into the SCF layer was found.

[19] C. T. Campbell, "Ultrathin metal films and particles on oxide surfaces: structural, electronic and chemisorptive properties," Surf. Sci. Rep. **27**, 1 (1997).

[20] H. Yang, S.-H. Yang, and S. S. P. Parkin, "Crossover from Kondo-Assisted Suppression to Co-Tunneling Enhancement of Tunneling Magnetoresistance via Ferromagnetic Nanodots in MgO Tunnel Barriers," Nano Lett. **8**, 340 (2007).

[21] S. Handschuh, J. Landes, U. Köbler, C. Sauer, G. Kisters, A. Fuss, and W. Zinn, "Magnetic properties of amorphous Fe in Fe/Y layered structures," J. Magn. Magn. Mat. **119**, 254 (1993).

[22] U. Herr, "Metastable phases in interface controlled materials," Contemp. Phys. **41**, 93 (2000).

[23] J. Landes, C. Sauer, B. Kabius, and W. Zinn, "Critical thickness of the amorphous-nanocrystalline transition in Gd/Fe film structures," Phys. Rev. B **44**, 8342 (1991).

[24] C. T. Campbell, "Ultrathin metal films and particles on oxide surfaces: Structural, electronic and chemisorptive properties," Surf. Sci. Rep. **27** (1-3), 1-111 (1997).

[25] G. Herzer, "Anisotropies in soft magnetic nanocrystalline alloys," J. Magn. Magn. Mat. **294**, 99 (2005).

[26] E. Kita, N. Tsukuhara, H. Sato, K. Ota, H. Yangaihara, H. Tanimoto, and N. Ikeda, "Structure and random anisotropy in single-phase Ni nanocrystals," Appl. Phys. Lett. **88**, 152501 (2006).

[27] H. R. Liu, B. J. Qu, T. L. Ren, L. T. Liu, H. L. Xie, C. X. Li, and W. J. Ku, "High-sensitivity GMR with low coercivity in top-IrMn spin-valves," J. Magn. Magn. Mat. **267**, 386 (2003).

[28] J. F. Loffler, H.-B. Braun, and W. Wagner, "Magnetic Correlations in Nanostructured Ferromagnets," Phys. Rev. Lett. **85**, 1990 (2000).

[29] M. Hu, S. Noda, and H. Komiyama, "Amorphous-to-crystalline transition during the early stages of thin film growth of Cr on SiO[sub 2]," J. Appl. Phys. **93**, 9336 (2003).

[30] M. Julliere, "Tunneling between ferromagnetic films," Phys. Lett. A **54**, 225 (1975).

[31] C. Kaiser and S. S. P. Parkin, "Spin polarization in ferromagnet/insulator/superconductor structures with the superconductor on top of the barrier," Appl. Phys. Lett. **84**, 3582 (2004).

[32] R. Meservey and P. M. Tedrow, "Spin-polarized electron tunneling," Phys. Rep. **238**, 173 (1994).

[33] D. J. Monsma and S. S. P. Parkin, "Spin polarization of tunneling current from ferromagnet/Al_2O_3 interfaces using copper-doped aluminum superconducting films," Appl. Phys. Lett. **77**, 720 (2000).

[34] D. C. Worledge and T. H. Geballe, "Maki analysis of spin-polarized tunneling in an oxide ferromagnet," Phys. Rev. B **62**, 447 (2000).

[35] A. Kotani and S. Shin, "Resonant inelastic x-ray scattering spectra for electrons in solids," Rev. Mod. Phys. **73**, 203 (2001).

[36] J. C. Fuggle and N. Martensson, "Core-level binding energies in metals," J. Electron Spectrosc. Relat. Phenom. **21**, 275 (1980).

[37] A. Nilsson, J. Stohr, T. Wiell, M. Alden, P. Bennich, N. Wassdahl, M. G. Samant, S. S. P. Parkin, N. Martensson, J. Nordgren, B. Johansson, and H. L. Skriver, "Determination of the electronic density of states near buried interfaces: Application to Co/Cu multilayers," Phys. Rev. B **54**, 2917 (1996).

[38] P. E. Blochl, "Projector augmented-wave method," Phys. Rev. B **50**, 17953 (1994).

[39] G. Kresse and D. Joubert, "From ultrasoft pseudopotentials to the projector augmented-wave method," Phys. Rev. B **59**, 1758 (1999).

[40] VASP is an ab initio simulation package developed at the University of Vienna in Vienna, Austria. For details see http://cms.mpi.univie.ac.at/vasp/.

[41] J. P. Perdew and Y. Wang, "Accurate and simple analytic representation of the electron-gas correlation energy," Phys. Rev. B **45**, 13244 (1992).

[42] M. Fuentes-Cabrera, D. Nicholson, M. Widom, Y. Wang, and M. Mihalkovic, "Ab-Initio Study of the Diffusion Coefficients in Fe-Based Liquids," Mater. Res. Soc. Symp. Proc. **806**, MM3.8 (2003).

[43] M. Mihalkovic and M. Widom, "Ab initio calculations of cohesive energies of Fe-based glass-forming alloys," Phys. Rev. B **70**, 144107 (2004).

[44] M. Gradhand, C. Heiliger, P. Zahn, and I. Mertig, "Tunneling magnetoresistance with amorphous electrodes," Phys. Rev. B **77**, 134403 (2008).

[45] I. Turek and J. Hafner, "Magnetism of amorphous iron: From ferromagnetism to antiferromagnetism and spin-glass behavior," Phys. Rev. B **46**, 247 (1992).

Chapter 4

TUNNELING ANISOTROPIC MAGNETORESISTANCE IN MAGNETIC TUNNEL JUNCTIONS WITH 3D TRANSITION METALS

4.1 INTRODUCTION

As discussed in previous chapters, magnetic tunnel junctions (MTJs) can exhibit very large changes in resistance when the relative alignment of the electrode moments is switched[1], and this tunneling magnetoresistance (TMR) is largely determined by the spin polarization of the tunneling current, which is a consequence, not simply of the spin polarized density of states (DOS) of the ferromagnetic electrodes, but also of the tunneling matrix elements[2,3], and the spin-dependent decay of the electron wavefunctions across the tunnel barrier[4-7]. It is also well established that the interface between electrode and barrier plays a crucial role in the spin-dependent tunneling process. Although using electrodes formed from the 3d transition metal (TM) ferromagnets, such as Co-Fe alloys, and tunnel barriers formed from Al_2O_3 and MgO, high TMR values of up to ~70% and ~600% are observed at room temperature[8-12], respectively, many aspects of TMR remain poorly understood despite extensive experimental and theoretical efforts. Of particular interest is the influence of the detailed electronic structure of the MTJ on the bias voltage dependence of the spin-polarized tunneling. One way to probe such an effect is to consider the *angular* dependence of the tunneling resistance, or the tunneling anisotropic magnetoresistance (TAMR) when the electrode's moments are rotated in large magnetic fields.

On the other hand, the effect of spin-orbit coupling (SOC) on the tunneling process was usually neglected due to the complexity that it would add to an already complicated problem. SOC was incorporated in the calculations of TMR of GaMnAs/GaAlAs/GaMnAs tunnel junctions by Brey *et al.*[13], and it was found that the junction resistance depends on the angle between the current flow direction and the electrode magnetization direction due to strong SOC. A large TAMR effect was recently observed in distinctly different MTJs formed from semiconductor heterostructures in which the ferromagnetic electrodes are formed from Mn doped GaAs[14-16]. The obtained high TAMR effect in MTJs with only one single ferromagnetic layer shows a rich phenomenology that could open new directions in realizing the sensing and memory functionality. SOC plays an important role in the Ga(Mn,As) so that the TAMR effect could be attributed to a significant anisotropy in

the DOS linked to the magnetization direction along different crystal axes[14-16]. Although SOC is much weaker in TMs, a small TAMR effect has been predicted for tunnel junctions with TM electrodes[17,18]. Calculations by Shick *et al.* predict that the anisotropic DOS in *hcp* Co electrodes can lead to TAMR of ~ 0.3-1.3%[18]. Another important factor that needs to be taken into consideration is the resonant interface states, which can produce sizeable TAMR effect due to SOC induced resonant surface band shift via the Rashba effect when the magnetization direction changes[17]. These calculations did not, however, consider the detailed bias nor angular dependence of the TAMR effect. In this chapter, the TAMR effect is studied in MTJs with CoFe electrodes as the moments are rotated from in-plane to out-of-plane in sufficiently large magnetic fields that the moments are nearly parallel to one another. A complex angular dependence of the tunneling resistance is found with two fold and four fold components which vary strongly with bias voltage. Distinctly different TAMR behaviors are obtained for devices formed from highly textured crystalline MgO(001) and amorphous Al_2O_3. A tight-binding model shows that a four fold angular dependence can be explained by the presence of an interface resonant state which affects the transmission of the contributing tunneling states through a spin-orbit interaction. In addition, the TAMR effect from tunnel junctions with antiferromagnetic CrMo electrode will also be briefly discussed.

4.2 EXPERIMENTS AND RESULTS

4.2.1 Samples and Measurement Setup

As introduced in Chapter 2, MTJs were fabricated on thermally oxidized Si substrates using a combination of ion-beam and magnetron sputtering at ambient temperature. A small in-plane magnetic field was applied during deposition to define the easy axis of the magnetic films. *In situ* shadow masks were used to pattern junctions of $\sim 80 \times 80 \mu m^2$ in area. After deposition, the devices were annealed at $260°C$ for 30 minutes in a 1T field. Two types of MTJs, with CoFe ferromagnetic electrodes and

either a MgO or Al_2O_3 tunnel barrier, were fabricated with the following structures (from bottom to top): 100 MgO/ 50 Ta/ 250 $Ir_{22}Mn_{78}$/ 3 $Co_{49}Fe_{21}B_{30}$/ 60 $Co_{70}Fe_{30}$/ 34 MgO/ 25 $Co_{70}Fe_{30}$/ 150 $Co_{49}Fe_{21}B_{30}$/ 100 Ta, and 100 TaN/ 75 Ta/ 250 $Ir_{24}Mn_{76}$/ 5 $Co_{49}Fe_{21}B_{30}$/ 40 $Co_{70}Fe_{30}$/ 25 Al_2O_3/ 20 $Co_{70}Fe_{30}$/ 100 $Co_{49}Fe_{21}B_{30}$/ 50 Ta/ 75 Ru, where the numbers are nominal layer thicknesses in Å.

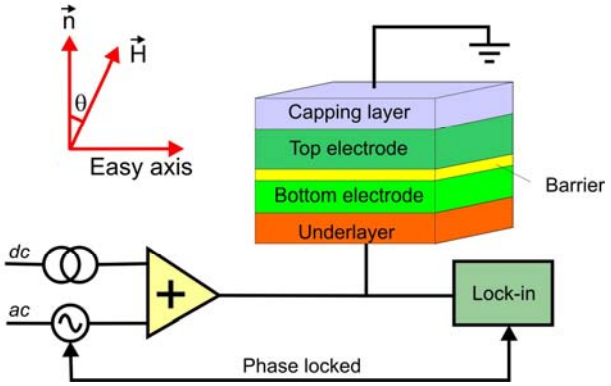

Fig. 4.1 Schematic diagram of the TAMR measurement setup. Mixer adds the dc bias voltage and a small ac voltage together, and applies the total voltage across the tunnel junction. Lock-in amplifier is used to measure the dynamic resistance at various dc bias voltages.

Magnetotransport measurements, both *dc* and *ac*, were carried out at 10 K in a low temperature cryostat equipped with a sample rotator and a superconducting magnet. An *ac* lock-in technique was used to measure the dynamic resistance $R_D = dV/dI$ of the tunnel junctions, with a modulation amplitude of 8 mV rms at 1001 Hz. A *dc* bias voltage was simultaneously applied during the *dV/dI* measurement, with positive bias corresponding to current flowing from bottom to top. The experimental geometry was such that the magnetic field $\vec{H}$, the normal to the film plane $\vec{n}$, and the magnetic easy axis were arranged in the same plane (Fig. 4.1). The field direction was fixed during the experiment and the sample was rotated so that the field direction was rotated from in-plane to out-of-plane. The *dc* and dynamic resistances were measured, using a four-point technique, as a function of the angle θ between $\vec{H}$ and $\vec{n}$. θ values of $0°$, $180°$, and $360°$ correspond to magnetic fields perpendicular to the film plane, while $90°$ and $270°$ correspond to fields along the in-plane easy axis direction.

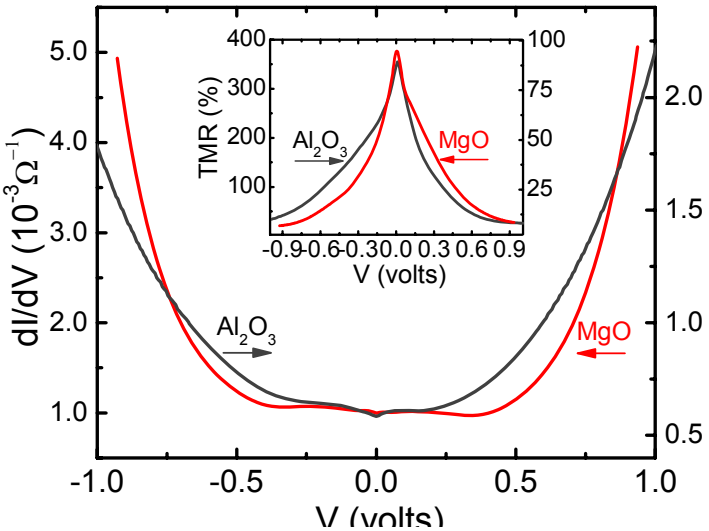

Fig. 4.2 The bias dependence of differential conductance for the MgO (red line) and Al_2O_3 (gray line) MTJs in a perpendicular field of 7 T at 10 K. The inset shows the bias dependence of the differential TMR at 10 K.

Fig. 4.2 depicts the differential conductance, *dI/dV*, as a function of bias voltage at 10 K in a perpendicular field of 7 T ($\theta = 0^\circ$), for MTJs with Al_2O_3 and MgO tunnel barriers, respectively. Data at $\theta = 90^\circ$ closely resemble those at $\theta = 0^\circ$. The inset in Fig. 4.2 shows the corresponding bias dependence of the differential TMR, defined as $\frac{(dI/dV)_P - (dI/dV)_{AP}}{(dI/dV)_{AP}}$. Here *dI/dV* is measured in an in-plane field; P and AP stand for parallel and antiparallel alignment of the CoFe moments, respectively. Zero-bias TMR values of 377% and 89% were obtained for the MTJs with MgO and Al_2O_3 barriers, respectively, indicating the high quality of these devices.

4.2.2 TAMR Results

Distinct TAMR effects were observed for CoFe/MgO/CoFe and CoFe/Al_2O_3/CoFe tunnel junctions; typical data at zero bias voltage are shown in Fig. 4.3, where dynamic resistance *dV/dI* are normalized to their minimum values. For the MgO tunnel junction, the resistance is larger when the field is perpendicular to the film plane than when the field is in the film plane, giving rise to a TAMR ratio of ~ 0.3%. However, for the Al_2O_3 sample, the TAMR effect is smaller than that in the MgO junction, and more

interestingly, its characteristics are significantly different and complex. To check that the observed TAMR results from spin-dependent tunneling, tunnel junctions with non-magnetic aluminum electrodes were fabricated with the following structure: 100 MgO/150 Al/32 MgO/150 Al/100 Ta (layer thicknesses in Å). No TAMR was measured within the experimental noise level for these control samples (black downward triangle in Fig. 4.3). This indicates that the observed TAMR effect results from the CoFe ferromagnetic electrodes and it is very sensitive to the tunneling barrier.

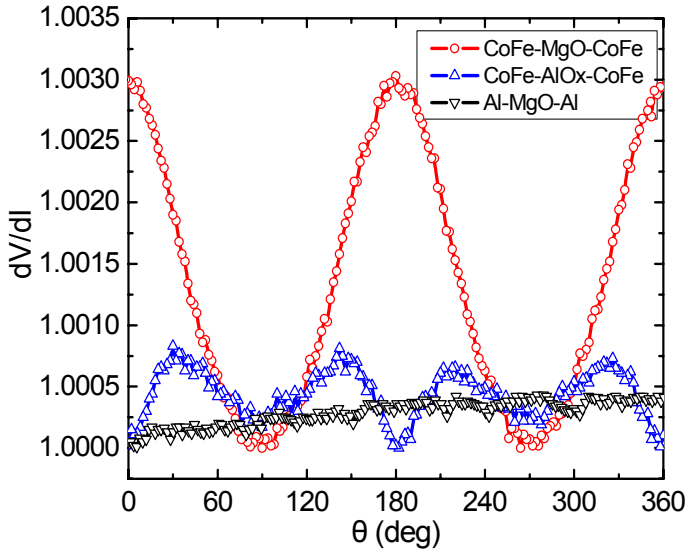

Fig. 4.3 Typical angular dependence of dV/dI curves for CoFe/MgO/CoFe, CoFe/Al_2O_3/CoFe, and Al/MgO/Al at zero bias in a field of 7 T at 10 K.

Detailed results about R_D vs. θ curves at various bias voltages are plotted in Fig. 4.4(a) for the MgO junction. The measurements were taken at 10 K in a field of 7 T which is sufficiently large to almost fully saturate the magnetization of the CoFe electrodes parallel to the field. The junction resistance is normalized to its average value over θ at each bias voltage. At low bias, the R_D vs. θ curves are two-fold symmetric, with peaks at $\theta = 0^\circ$, 180°, 360° and valleys at $\theta = 90^\circ$, 270°. As the bias is increased, the valleys near $\theta = 90^\circ$, 270° broaden and, eventually, a second set of peaks appears for bias voltages exceeding ~ -0.4 V or +0.45 V. This suggests that an additional component with four-fold symmetry contributes to TAMR at high bias. The magnitude of TAMR is fairly symmetric with respect to bias polarity at low bias. At high bias, however, TAMR is much smaller for positive bias.

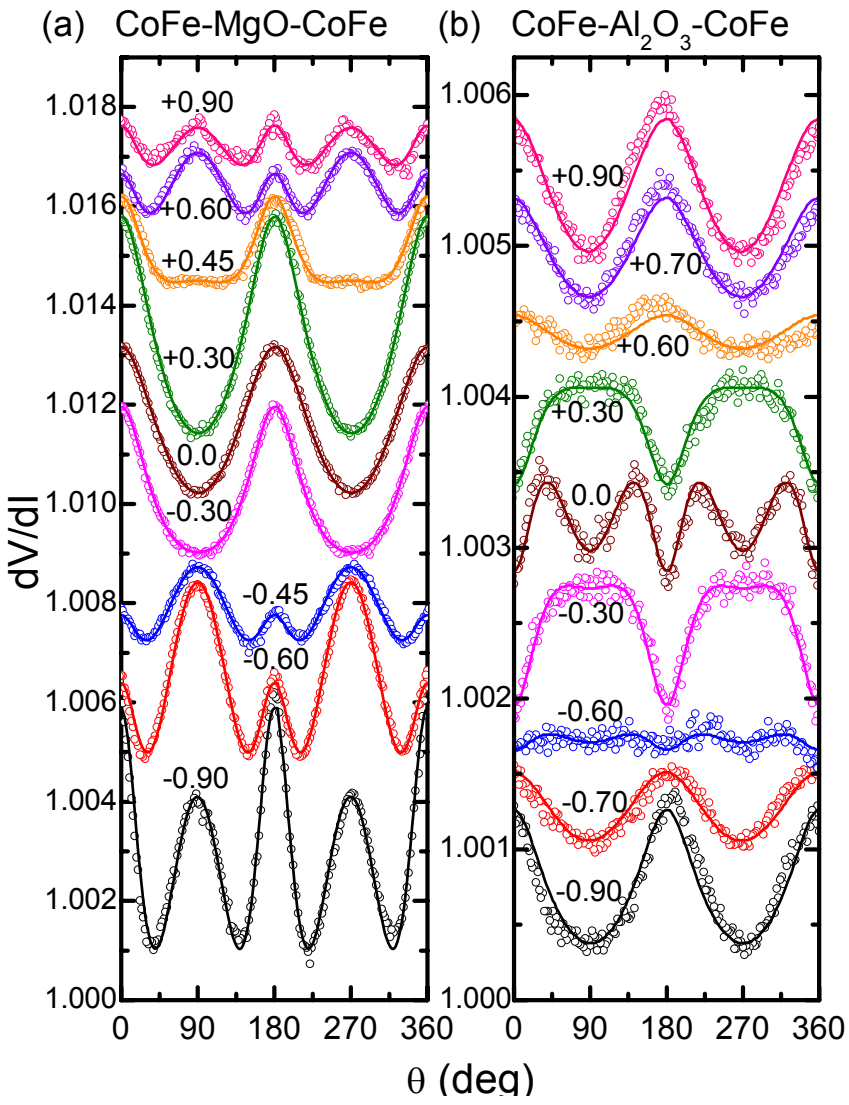

Fig. 4.4 Normalized R_D vs. θ curves (symbols) at various bias voltages for (a) MgO and (b) Al_2O_3 MTJs. The data are displaced vertically for clarity. The solid lines are fits using Eqs. (1) and (2).

In Fig. 4.5(a) and (c), the normalized junction resistance is plotted as a function of bias and angle, for the dynamic and *dc* resistance measurements, respectively. The data were taken, in each case, every 2 degree and every 50 mV (Note that in the dc case no data are possible at zero bias). The contrast in the contour plot represents the magnitude of the normalized junction resistance, in each case. The *dc* and dynamic resistances measure different quantities. The former integrates contributions from electrons distributed over a wide energy range up to the bias voltage, whereas the latter is sensitive to tunneling in a narrow energy range, determined by the modulation

amplitude (here, ~24 mV, peak to peak). The *ac* measurement clearly accentuates the dependence of the TAMR effect on both voltage and angle, as shown in Fig. 4.5. For this reason, the discussion will be focused on the dynamic resistance data.

For the MgO barrier, R_D shows valleys at $\theta = 90^\circ, 270^\circ$ at low bias, which are seen as dark areas in Fig. 4.5(a). The emergence of a second set of peaks can be clearly distinguished above a threshold voltage of ~ -0.4 V and +0.45 V, for negative and positive voltages, respectively. Note that this distinctive change in the angular dependence is obscured in the dc resistance plot. Above this threshold voltage the angular dependence shows clear evidence for some four-fold character.

The TAMR effect of the Al_2O_3 junction has distinctly different characteristics compared with that of the MgO junction, as shown in Fig. 4.4(b) and 4.5(b) and (d). Generally speaking, the TAMR magnitude is much smaller than that of the MgO junction. In the low bias regime, the R_D vs. θ curve contains a four-fold symmetric component with minima at $\theta = 0^\circ$ and 90°. As the bias increases, the curve becomes largely two-fold symmetric. Below ~ ±0.6 V, the curve has a maximum at $\theta = 90^\circ$ and a minimum at $\theta = 0^\circ$. Above ~ ±0.6 V, however, the positions for the resistance extrema are reversed, i.e., the maximum is at $\theta = 0^\circ$ and the minimum is at $\theta = 90^\circ$. These features are clearly seen in Fig. 4.5(b). Note that the basic characteristics of the contour plots shown in Fig. 4.5 do not change with field for the explored range from 5 to 9 T.

The R_D vs. θ curve at a given bias can be fitted using the following equations:

$$R_D(\theta) = \left(A_0 + A_2 \cos 2\phi + A_4 \cos 4\phi\right)^{-1} \qquad (1)$$

$$\frac{\cos\phi}{\sin\phi} = \frac{H\cos\theta - 4\pi M_s \cos\phi}{H\sin\theta} \qquad (2)$$

where ϕ is the angle between the CoFe magnetization direction and the film normal direction $\vec{n}$ after taking into account the demagnetization field; M_s is the saturation magnetization of CoFe; A_0, A_2, and A_4 are fitting parameters. The ratios A_2/A_0 and A_4/A_0 can be understood as half of the TAMR magnitude of the components with two- and four-fold symmetries, respectively. Their signs are related to the positions of the resistance extrema in the R_D vs. θ curves. Assuming $4\pi M_S$ = 1.93 T, excellent agreement between data and fits are obtained (see Fig. 4.4). A_2/A_0 and A_4/A_0 values,

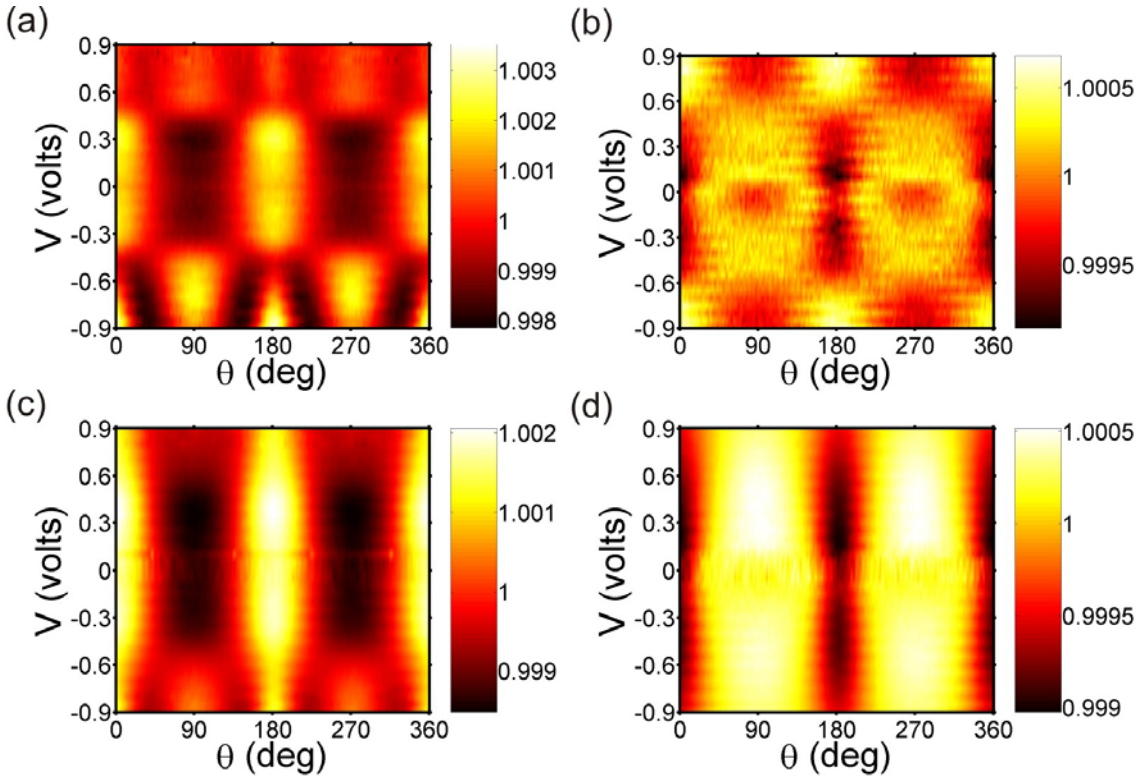

Fig. 4.5 (a) and (b) Contour plots of R_D as a function of bias and angle for the MgO and Al_2O_3 MTJs; (c) and (d) Corresponding contour plots of dc resistance.

obtained from the fits, are plotted in Fig. 4.6, which show very complicated bias dependences for both types of junctions. For the MgO junction, A_2/A_0 depends only weakly on bias below ±0.4 V, whilst A_4/A_0 is nearly zero. Around ±0.4 V, A_2/A_0 increases rapidly from a negative to a positive value and reaches maximum at ~ ±0.60 V. The positive values of A_2/A_0 indicate that the maximum resistance in the R_D vs. θ curve appears at θ = 90º, 270º. A_2/A_0 decreases at even higher bias and becomes negative for the negative bias. On the other hand, A_4/A_0 is negative above ±0.4 V and its magnitude increases with bias before saturating at high bias. For the Al_2O_3 junction, the bias dependence of A_2/A_0 and A_4/A_0 are very different. A_4/A_0 is much larger than A_2/A_0 near zero bias. It decreases monotonically with bias and approaches zero above ±0.6 V.

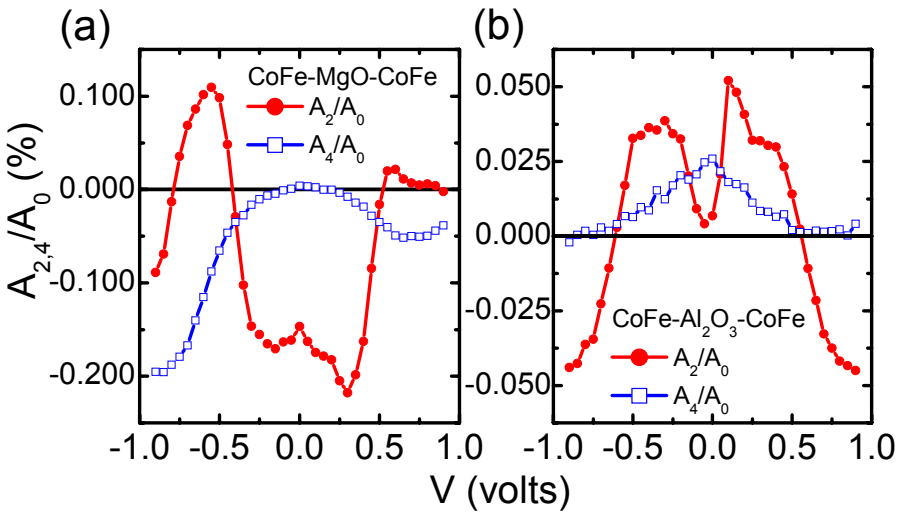

Fig. 4.6 (a) and (b) Fitting parameters A_2/A_0 (solid circles) and A_4/A_0 (open squares) as a function of bias for the MgO and Al_2O_3 MTJs.

In contrast, A_2/A_0 shows a more complex bias dependence. It initially increases with bias up to ±0.2 V. After that it shows a relatively weak bias dependence before starting to decrease for bias exceeding ±0.5 V. A_2/A_0 changes sign at ~ ±0.6 V and becomes negative at high bias. Note that in the low bias regime below ±0.4 V, A_2/A_0 and A_4/A_0 have opposite signs for the MTJs with MgO and Al_2O_3 barriers. This means that the angular dependence of R_D is out of phase for the two types of tunnel junctions.

4.2.3 Inelastic Electron Tunneling Spectroscopy

Inelastic electron tunneling spectroscopy (IETS) was first developed by Jacklevic and Lambe[19]. It is a very powerful technique to study the electronic structure of chemical compounds, as well as the detailed electronic nature of the metal/insulator interfaces between. Spectroscopic studies of defects, impurities, magnons, and phonons have been carried out to investigate the tunneling processes which are extremely sensitive to the characteristics of density of states at barrier/electrode interface in a MTJ[20]. Usually, the number of electrons tunneling inelastically is orders of magnitude smaller than those tunneling elastically which dominate the tunneling conductance and can be well modeled by Simmons' equation[21]. Therefore, it is hard to find any clue about the inelastic tunneling process in the normal *I-V* or conductance-*V* curves because the

background from elastic tunneling is so dominating that it overwhelms any possible spectroscopic signal from inelastic process. However, second order derivatives of the conductance vs. voltage can often reveal peaks at which energies such inelastic tunneling channels open.

Lock-in amplifiers were used to measure the second harmonic of the *ac* current (I_{2f}) flowing through the tunnel junctions. The amplitude (V_{ac}) and frequency of the *ac* modulation are 3-5 mV rms and 1001 Hz, respectively. Applying a *dc* bias voltage superimposed with this small *ac* modulation signal $V_{ac}\cos(\omega t)$ across a MTJ, the flowing current can be written as,

$$\begin{aligned} I(V) &= I(V_{dc} + V_{ac}\cos\omega t) \\ &= I(V_{dc}) + \left.\frac{dI}{dV}\right|_{V_{dc}} V_{ac}\cos\omega t + \frac{1}{2}\left.\frac{d^2I}{dV^2}\right|_{V_{dc}} V_{ac}^2\cos^2\omega t + \ldots \\ &= I(V_{dc}) + \underbrace{\left.\frac{dI}{dV}\right|_{V_{dc}} V_{ac}\cos\omega t}_{I_f} + \frac{1}{4}\left.\frac{d^2I}{dV^2}\right|_{V_{dc}} V_{ac}^2 + \underbrace{\frac{1}{4}\left.\frac{d^2I}{dV^2}\right|_{V_{dc}} V_{ac}^2\cos 2\omega t}_{I_{2f}} \ldots \end{aligned}$$

Therefore, the amplitude of the first harmonics is proportional to the first-derivative term, and the second harmonics is proportional to the second-derivative term which can be easily detected by a lock-in amplifier. The IETS signal d^2I/dV^2, which is measured as I_{2f}/V_{ac}^2, for the two tunnel junctions are plotted in the inset of Fig. 4.7. If the tunneling electrons have a free-electron-like parabolic band, the IETS signal is expected to vary linearly with bias[22]. The deviation from the parabolic band is seen by subtracting a linear background from the IETS data, as shown in Fig. 4.7. The peak structures at low bias around zero are due to magnon and phonon scatterings. For the MgO junction, characteristic structures are observed around ±0.4 V and ±0.6 V, coincident with the threshold voltages where significant changes in A_2/A_0 and/or A_4/A_0 occur. These structures might result from the electronic structure of the interface states in the MgO tunnel junctions. For the Al_2O_3 MTJ, the high bias features are less pronounced, especially at positive bias, the position of the peak moves to lower voltage. These results clearly illustrate the electrode/barrier interface difference between the MgO and Al_2O_3 tunneling junctions.

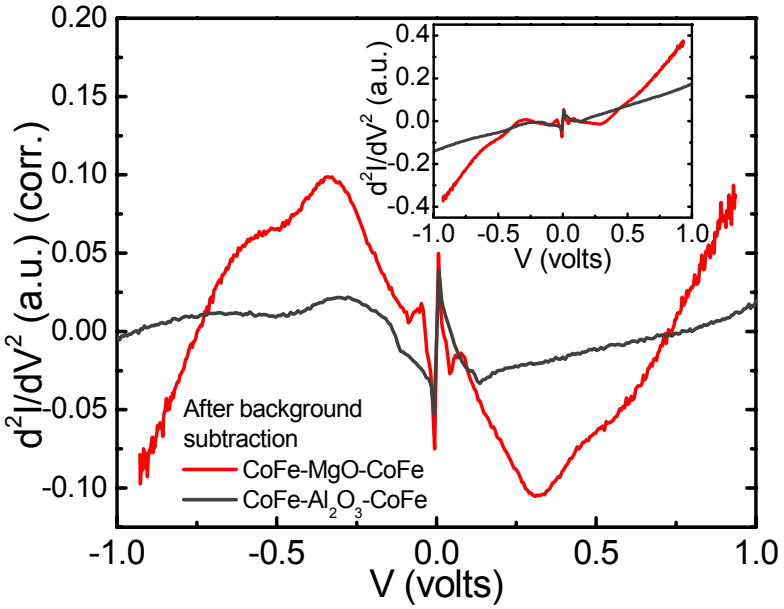

Fig. 4.7 IETS data for the CoFe/MgO/CoFe (red line) and CoFe/Al_2O_3/CoFe (gray line) MTJs after linear background subtraction. The inset shows the original data.

4.3 DISCUSSION

The TAMR effect likely originates from SOC, which gives rise to an anisotropy of the DOS of the bulk electrodes[14,15,18] and that of their interfaces[17] with respect to the magnetization direction. The pronounced difference between the MgO and Al_2O_3 MTJs points to the interface electronic structure as the origin of the TAMR. Using a simple tight-binding model, it is demonstrated that the influence of resonant states on the interface DOS of the majority band can lead to the observed evolution of TAMR from a two-fold to a four-fold angular dependence. Note that calculations have also been carried out to examine the band structure of *bcc* CoFe along the Γ-H ($k_{||} = 0$) direction in the Brillouin zone. Specifically, the lifting of degeneracy in the bulk band structure due to SOC was explored and no four-fold component in the angular dependence of the DOS at any energy sufficient to lead to the observed variation in the experiments was found. This suggests that the four-fold component does not arise from the bulk band structure of CoFe.

In the calculations, the Δ_1 majority-spin band in *bcc* CoFe[4] is modeled by a one-dimensional tight-binding band. Consider the case when this band is coupled to a minority resonant state localized at the interface via SOC described by the parameter λ. The anisotropy in the conductance is determined by the anisotropy of the interface DOS of the majority Δ_1 band, which can be found from the corresponding interface Green's function, *g(E)*. By solving Dyson's equation it is found that

$$g(E) = \frac{g_0(E)}{1 - \lambda^2 g_0(E) g_r(E) \cos^2 \phi} \qquad (3)$$

where $g_0(E)$ is the interface Green's function of the majority band in the absence of SOC[3] and $g_r(E) = (E - E_r + i\gamma_0)^{-1}$ is the Green's function of the resonant level with E_r and γ_0 being the resonance energy and width, respectively.

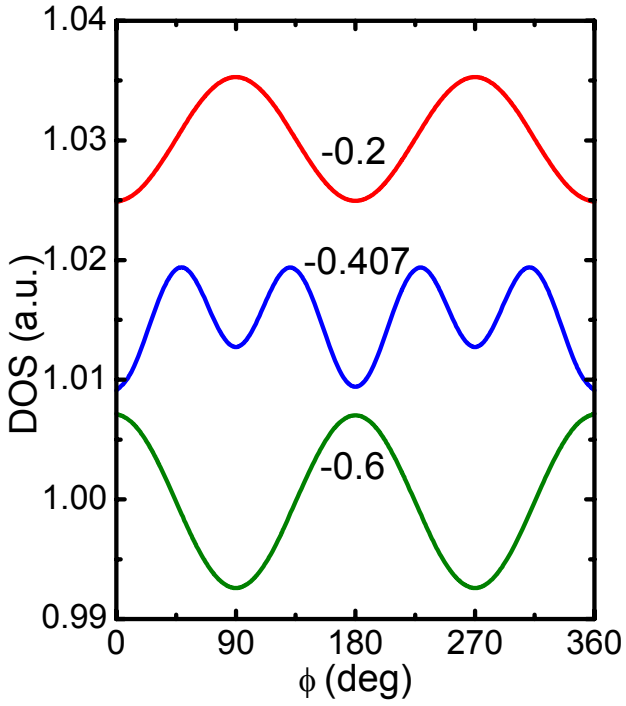

Fig. 4.8 Angular dependence of the interface DOS of the majority band (in arbitrary units) for several energies E near the resonant energy E_r = –0.4 eV. Energies are given in eV. The majority band has width 4 eV and is centered at 0.6 eV. The width of the resonant state γ_0 = 10 meV, and the spin-orbit coupling parameter λ = 50 meV.

Fig. 4.8 shows the interface DOS of the majority band, $\rho = -\mathrm{Im}(g)/\pi$, as a function of ϕ for several energies near the resonant level which is chosen to lie at E_r =

–0.4 eV. Away from the resonance, the angular dependence of the interface DOS has two-fold symmetry. This two-fold angular dependence changes sign near the resonant energy. Associated with this sign change is the onset of a significant four-fold angular variation. Since the tunneling current will largely be determined by the interface DOS of the majority Δ_1 channel, this same variation will appear in the R_D measurement when the window of applied bias passes the resonance.

It is known that the *bcc* Fe(001) surface supports a minority-spin surface state[23]. The relevant interface state is present in Fe(001)/MgO/Fe tunnel junctions, as indicated by theory and experiment[3,4,24]. A similar resonant state is likely present at the *bcc* CoFe(001) surface and the CoFe(001)/MgO interface. Using a rigid band model to estimate the change in the Fermi energy due to the increase in valence of CoFe as compared to Fe it is found that the position of the interface resonant state for $Co_{70}Fe_{30}$(001)/MgO interface is ~0.4 eV below the Fermi energy. This is consistent with the observation of significant four-fold symmetry for bias beyond ~ -0.4 V or +0.45 V for MgO based MTJs, as shown in Fig. 4.4.

Somebody might argue that electron states located at 0.4 eV below the Fermi level cannot contribute to tunneling since the electron transmission through an energy barrier decays exponentially with increasing barrier height. This, however, is a simple picture, which is not in general valid. This picture is applicable only when the electron tunneling can be described within a free-electron, single-band model. In general, the efficiency of tunneling is controlled by evanescent states, arising from the complex band structure of the insulator, and the energy dependence of their decay constant.[25] For the case of Fe and other *bcc* ferromagnetic alloys such as the CoFe alloy used in the experiments with MgO tunnel barriers, it has been shown (see, for example, Fig. 8 of Butler *et al.*) that the electron decay constant does not vary significantly for states near the Fermi energy, and that states at 0.4 eV and at even lower energies below the Fermi level contribute significantly to tunneling. It is correct to point out that the tunneling in the experiments is dominated by the CoFe majority Δ_1 states for the case of CoFe/MgO. It is proposed that these states are mixed with the known minority resonant state due to SOC, and the tight-binding model then produces the angular variation in the DOS shown in Fig. 4.8.

It should be emphasized that the model assumes that the majority spin-polarized states dominate the tunneling conductance, in particular, *g(E)* in Eq. (3) is the interface Green's function component corresponding to the majority band, not the minority resonant states. Therefore, the experiments probe the effect of the resonance states on the transmission of the majority Δ_1 channel, not the transmission directly from the resonant states. The latter contribution could indeed show up in the bias dependence of the TMR although likely only for thin barriers. With increasing barrier thickness, the contribution from resonant transmission through the minority resonant channel was shown by Stroscio *et al.* to decrease quickly[23] and would not therefore be expected to be reflected in the bias dependence of the TMR in the experiments where the barriers are relatively thick. By contrast, the effect of the admixture of the resonant state with the Δ_1 states should be independent of the barrier thickness. Thus, it is reasonable to conclude that the resonant state can influence the TAMR which is a small effect (~0.5%) but not necessarily the bias voltage dependence of the TMR, which in these samples is ~350%. The measured bias voltage dependence of TMR on the sample is consistent with that reported by the groups of Ohno *et al.* and Yuasa *et al.* who also report TMR values consistent with these.

Modeling of the CoFe/Al_2O_3 tunnel junction is not straightforward due to the amorphous nature of the barrier. In this case, the tunneling is not dominated by one conduction channel as in the MgO case. In addition, the electronic structure of the CoFe/Al_2O_3 interface may be much more complex as compared to the CoFe/MgO interface. For Al_2O_3 based MTJs a similar effect may occur due to the possibility of a narrow majority interface resonant band derived from excess oxygen at the interface[3]. It is predicted that this band lies close to the Fermi level and is strongly transmitting. An analysis based on a model similar to that above reveals that an interface resonant DOS also has a significant four-fold angular variation when coupled to a bulk band via SOC. This is consistent with the observation of a strong four-fold dependence of the variation observed in Al_2O_3 at low bias in Fig. 4.4. In the case of CoFe/MgO tunnel junction, since the transmission is dominated by the majority Δ_1 states, the tight-binding model captures the basic physics of the experimental observation; however, in the case

of the CoFe/Al_2O_3 tunnel junction, one has to consider contributions from more than one band, which is beyond the scope of the model.

4.4 OTHER RESULTS

The TAMR effect with other *3d* transition metals, such as antiferromagnetic CrMo alloy, was also investigated in MgO based tunnel junctions. Since the lattice size of this *bcc* alloy is very close to that of *bcc* Fe, epitaxial growth of a multilayered structure with MgO can be obtained. Samples were grown and annealed with the same techniques as discussed before. Four sets of tunnel junctions were fabricated with the following structures (from bottom to top): 100 MgO/50 Ta/250 $Ir_{24}Mn_{76}$/60 X/~32 MgO/100 Y/50 Ta/75 Ru, where the numbers are film thicknesses given in Ångström, and X and Y are either $Co_{70}Fe_{30}$ or $Cr_{85}Mo_{15}$. These four types of X/MgO/Y structures will be referred as CoFe/MgO/CoFe, CrMo/MgO/CoFe, CoFe/MgO/CrMo, and CrMo/MgO/CrMo, for short. The measurement setup was similar to that used in the previous section, except that only *dc* tunneling resistance was studied. The experiments were also carried out at 10 K. A bias voltage was applied across the tunnel junction, giving rise to a current flowing perpendicular to the film plane. For positive bias voltages, the current flows from the bottom electrode to the top electrode. The experimental geometry and the definition of the angle are the same as before, i.e., θ values of 0°, 180°, and 360° correspond to magnetic fields perpendicular to the film plane, whilst θ values of 90° and 270° correspond to fields parallel to the in-plane easy axis.

Fig. 4.9 depicts the differential conductance *dI/dV* as a function of bias at 10 K in a perpendicular field of 7 T. The *dI/dV* curves are reasonably symmetric for CoFe/MgO/CoFe and CrMo/MgO/CrMo tunnel junctions. On the other hand, larger asymmetry in *dI/dV* is obtained for CoFe/MgO/CrMo and CrMo/MgO/CoFe junctions. In these junctions, the conductance is always smaller when the electrons tunnel from the CrMo layer into the CoFe layer. This may be related to the lack of a Δ_1 state near the

Fermi level in the $Cr_{85}Mo_{15}$ electrode[26] since the decay rate of the Δ_1 state is the slowest in MgO barriers and contributes most to the tunneling conductance. The insets of Fig. 4.9 show the *I-V* curves of these devices, and the highly nonlinear curves are the indicators for high quality tunnel junctions.

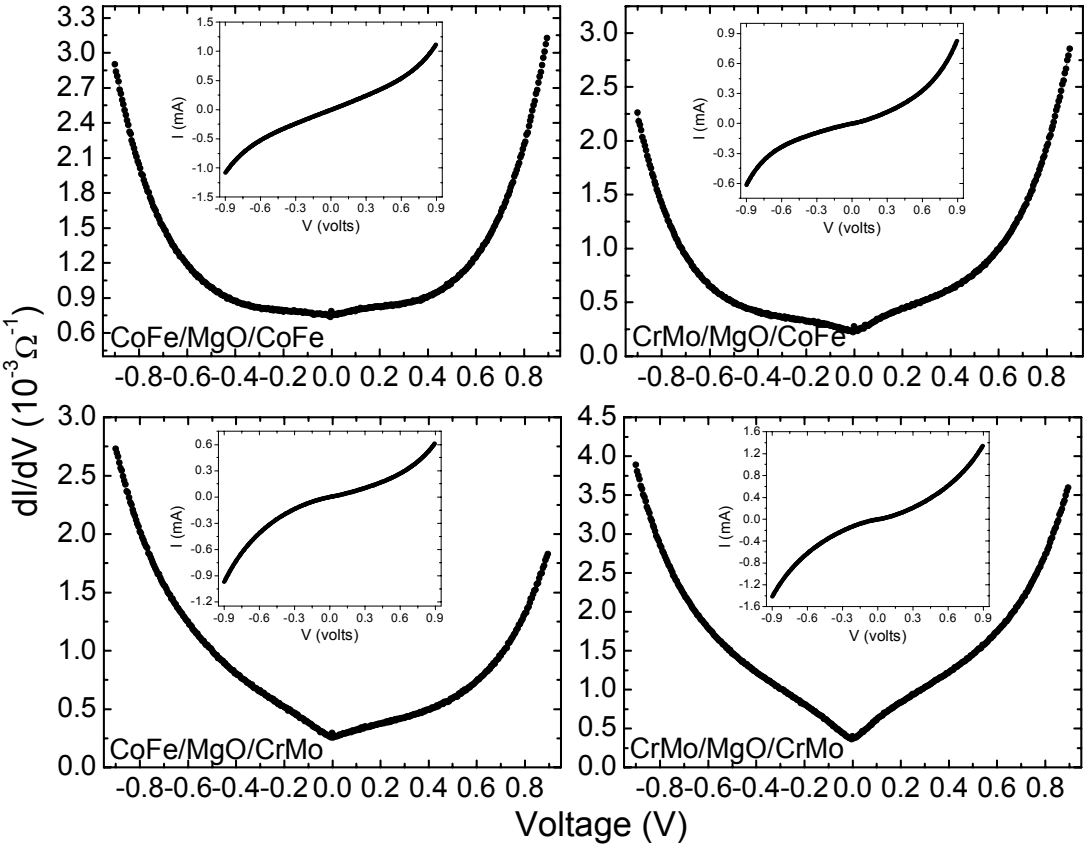

Fig. 4.9 Bias dependence of differential conductance for CoFe/MgO/CoFe, CrMo/MgO/CoFe, CoFe/MgO/CrMo, and CrMo/MgO/CrMo tunnel junctions. The insets show the I-V curves of the tunnel junctions. The measurements were taken at 10 K in a perpendicular field of 7 T.

Distinct TAMR effects were observed at 10 K for the four types of tunnel junctions, as shown in Fig. 4.10. In these measurements, a large (7 T) magnetic field was used to align the moments of both electrodes along the field direction. For the CoFe/MgO/CoFe junctions (Fig. 4.10(a)), the resistance is larger when the field is perpendicular to the film plane than when the field is in-plane, giving rise to a TAMR ratio of ~0.6%. As the bias increases, the valleys in the R-θ curve broadens near $\theta = 90^{\circ}$ and 270º (field in-plane). Eventually, a second set of peaks appears at large bias, same as discussed previously. If both the CoFe electrodes are replaced by CrMo (Fig.

4.10(d)), the basic characteristic of TAMR effect becomes reversed, i.e. maximum peaks occur at $\theta = 90^{\circ}$ and 270º now. Although smaller than that in CoFe/MgO/CoFe, the TAMR effect in CrMo/MgO/CrMo shows fairly symmetric characteristics with respect to bias voltage, and the R-θ curves only display twofold symmetry. In contrast with CoFe/MgO/CoFe, no TAMR effect is discernible in CrMo/MgO/CrMo at the low bias.

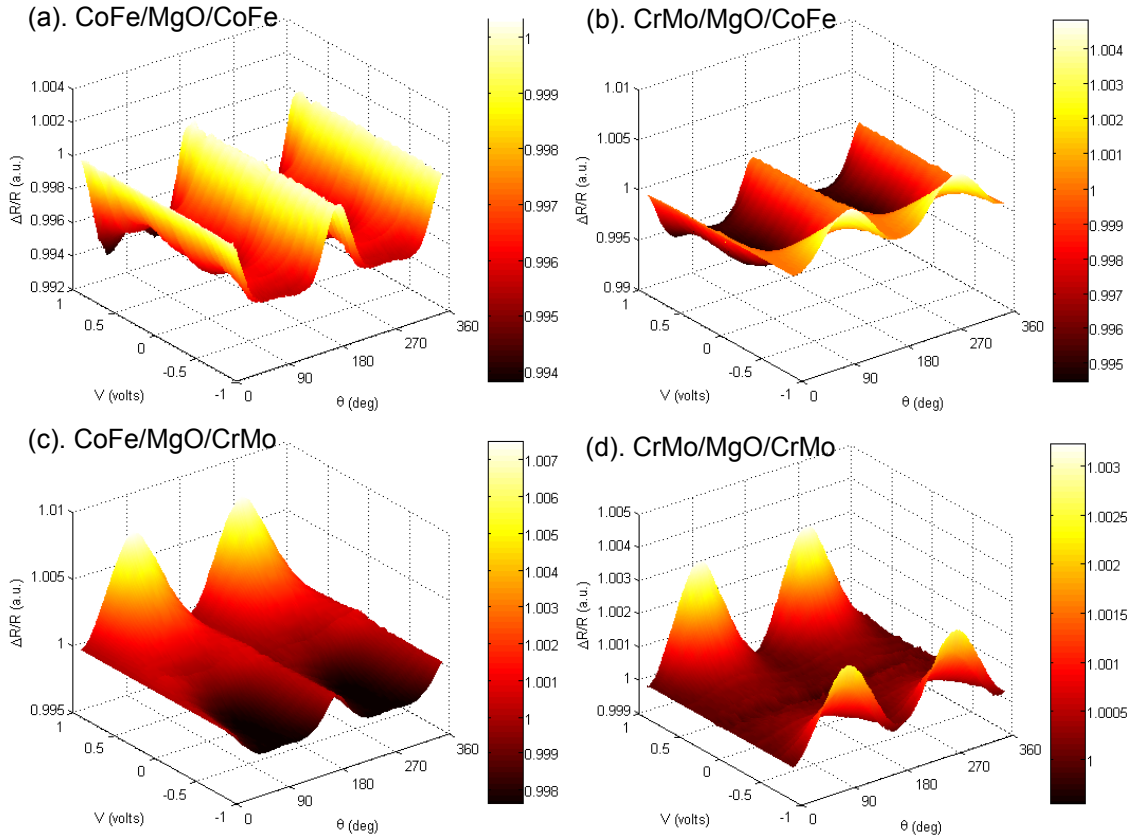

Fig. 4.10 Contour plots for the angular dependence of normalized dc resistance at 10 K in a field of 7 T at various bias voltages for (a) CoFe/MgO/CoFe, (b) CrMo/MgO/CoFe, (c) CoFe/MgO/CrMo, and (d) CrMo/MgO/CrMo tunnel junctions.

If either the bottom or top CoFe electrode is replaced by CrMo (Fig. 4.10(b) and (c)), the bias dependence of the TAMR effect will change sign accordingly. Namely, when electrons emerge from CoFe electrode, the TAMR effect has a peak at θ = 180º, however, when electrons emerge from CrMo, the TAMR effect has a peak at $\theta = 90^{\circ}$. The CrMo caused TAMR effect is somewhat unexpected since CrMo is an antiferromagnetic material[27], which should be not responsive to a field of 7 T.

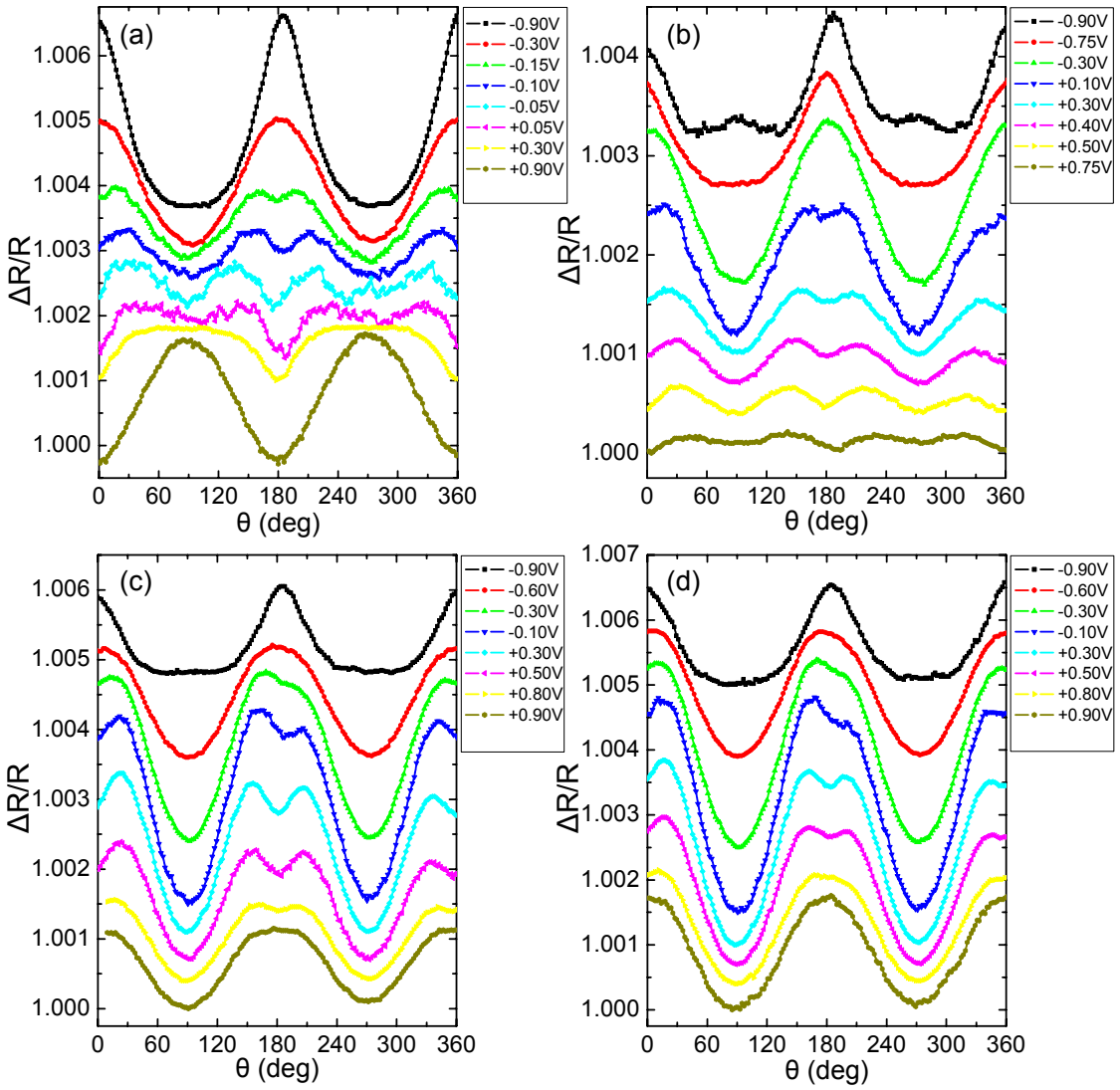

Fig. 4.11 Angular dependence of normalized resistance at 10 K in a field of 7 T at various bias voltages for (a) CoFe/MgO/0 CoFe/CrMo, (b) CoFe/MgO/5 CoFe/CrMo, (c) CoFe/MgO/10 CoFe/CrMo, and (d) CoFe/MgO/15 CoFe/CrMo tunnel junctions. The curves are displaced vertically for clarity.

To make sure this sign reversal of the TAMR is not an artifact, CoFe/MgO/CrMo tunnel junctions with a CoFe interface layer inserted between MgO and CrMo were also fabricated and measured. It was found that an interface layer as thin as 10 Å was sufficient to recover the bias dependence of TAMR, similar to that of CoFe/MgO/CoFe tunnel junctions as shown in Fig. 4.11. This indicates that the observed reversal of the TAMR effect from CrMo is very sensitive to the properties of the interface between the barrier and the CrMo.

The Bloch states in *bcc* CoFe and CrMo can have Δ_1, Δ_5, Δ_2, or $\Delta_{2'}$ symmetry. In a CoFe/MgO/CoFe tunnel junction, the Bloch state with Δ_1 symmetry decays much slower than the other states inside the MgO barrier. As a result, the tunneling conductance is dominated by the Δ_1 state. Therefore, the TAMR observed in these tunnel junctions reflects only the anisotropy of the Δ_1 state which has been fully discussed in the previous section. The observation of a reversed TAMR effect in the CrMo/MgO/CrMo tunnel junctions is interesting, although it is difficult to explain. For *bcc* CrMo, the Bloch state with Δ_1 symmetry is located at energy above the Fermi level from the calculations with an absence of SOC. After considering the spin-orbit interactions, bands with different symmetries mix with each other. As a result, a marginal density of Δ_1 states can exist near the Fermi level. However, the tunneling process is still mainly dominated by other states rather than Δ_1 at various bias voltages. Therefore, in a sense, it is not so surprising that the TAMR effect is reversed in CrMo compared to that in CoFe. Yet it is indeed surprising that the TAMR effect comes from an antiferromagnetic material, since its antiparallel magnetic moments in the bulk film should remain unresponsive to the applied field. To account for this effect, it might be reasonable to assume that there exist some loose spins at the CrMo/MgO interface, when the sample rotates in a magnetic field, these spins will change their orientation. Due to the SOC, the spin orientation change might affect the interface density of states contributing most to the tunneling conductance. Actually, field dependence of the TAMR effect was also studied, and it was found that a field as small as about 1 T can saturate the TAMR signal for each bias voltage, which means that these loose spins at the interface are indeed very soft.

4.5 SUMMARY

A tunneling anisotropic magnetoresistance effect has been observed in magnetic tunnel junctions with 3d transition metal ferromagnetic electrodes for both crystalline and amorphous tunnel barriers, despite the weak spin-orbit coupling in these systems. Complex dependences of the junction resistance on the bias voltage and angle are found, which are distinctly different for MgO and Al_2O_3 tunnel barriers. A tight-binding model suggests that the TAMR effect derives from the anisotropy in the interface density of states of the majority band due to mixing with a resonant state via spin-orbit coupling. In addition, a puzzling reversed TAMR effect from CrMo has also been observed and its mechanism requires further investigation and understanding.

REFERENCES:

[1] S. Parkin, X. Jiang, C. Kaiser, A. Panchula, K. Roche, and M. Samant, "Magnetically Engineered Spintronic Sensors and Memory," Proc. IEEE **91**, 661 (2003).

[2] C. Kaiser, S. van Dijken, S.-H. Yang, H. Yang, and S. S. P. Parkin, "Role of Tunneling Matrix Elements in Determining the Magnitude of the Tunneling Spin Polarization of 3d Transition Metal Ferromagnetic Alloys," Phys. Rev. Lett. **94**, 247203 (2005).

[3] E. Y. Tsymbal, K. D. Belashchenko, J. P. Velev, S. S. Jaswal, M. v. Schilfgaarde, I. I. Oleynik, and D. A. Stewart, "Interface effects in spin-dependent tunneling," Prog. Mater. Sci. **52**, 401 (2007).

[4] W. H. Butler, X.-G. Zhang, T. C. Schulthess, and J. M. MacLaren, "Spin-dependent tunneling conductance of Fe|MgO|Fe sandwiches," Phys. Rev. B **63**, 054416 (2001).

[5] S. S. P. Parkin, C. Kaiser, A. F. Panchula, P. Rice, M. G. Samant, S.-H. Yang, and B. Hughes, "Giant tunneling magnetoresistance at room temperature with MgO (100) tunnel barriers," Nature Materials **3**, 862 (2004).

[6] S. Yuasa, T. Nagahama, A. Fukushima, Y. Suzuki, and K. Ando, "Giant room-temperature magnetoresistance in single-crystal Fe/MgO/Fe magnetic tunnel junctions," Nature Materials **3**, 868 (2004).

[7] J. Mathon and A. Umerski, "Theory of tunneling magnetoresistance of an epitaxial Fe/MgO/Fe(001) junction," Phys. Rev. B **63**, 220403 (2001).

[8] T. Miyazaki and N. Tezuka, "Giant magnetic tunneling effect in Fe/Al_2O_3/Fe junction," J. Magn. Magn. Mater. **139**, L231 (1995).

[9] J. Hayakawa, S. Ikeda, Y. M. Lee, F. Matsukura, and H. Ohno, "Effect of high annealing temperature on giant tunnel magnetoresistance ratio of CoFeB/MgO/CoFeB magnetic tunnel junctions," Appl. Phys. Lett. **89**, 232510 (2006).

[10] J. J. Yang, C. Ji, Y. A. Chang, X. Ke, and M. S. Rzchowski, "Over 70% tunneling magnetoresistance at room temperature for a CoFe and AlOx based magnetic tunnel junction," Appl. Phys. Lett. **89**, 202502 (2006).

[11] S. Ikeda, J. Hayakawa, Y. Ashizawa, Y. M. Lee, K. Miura, H. Hasegawa, M. Tsunoda, F. Matsukura, and H. Ohno, "Tunnel magnetoresistance of 604% at 300K by suppression of Ta diffusion in CoFeB/MgO/CoFeB pseudo-spin-valves annealed at high temperature," Appl. Phys. Lett. **93**, 082508 (2008).

[12] D. Wang, C. Nordman, J. M. Daughton, Z. Qian, and J. Fink, "70% TMR at Room Temperature for SDT Sandwich Junctions With CoFeB as Free and Reference Layers," IEEE Trans. Magn. **40**, 2269 (2004).

[13] L. Brey, C. Tejedor, and J. Fernandez-Rossier, "Tunnel magnetoresistance in GaMnAs: Going beyond Julliere formula," Appl. Phys. Lett. **85**, 1996 (2004).

[14] C. Gould, C. Ruster, T. Jungwirth, E. Girgis, G. M. Schott, R. Giraud, K. Brunner, G. Schmidt, and L. W. Molenkamp1, "Tunneling anisotropic magnetoresistance: A spin-valve-like tunnel magnetoresistance using a single magnetic layer," Phys. Rev. Lett. **93**, 117203 (2004).

[15] C. Ruster, C. Gould, T. Jungwirth, J. Sinova, G. M. Schott, R. Giraud, K. Brunner, G. Schmidt, and L. W. Molenkamp, "Very Large Tunneling Anisotropic Magnetoresistance of a (Ga,Mn)As/GaAs/(Ga,Mn)As Stack," Phys. Rev. Lett. **94**, 027203 (2005).

[16] H. Saito, S. Yuasa, and K. Ando, "Origin of the Tunnel Anisotropic Magnetoresistance in Ga1-xMnxAs/ZnSe/Ga1-xMnxAs Magnetic Tunnel Junctions of II-VI/III-V Heterostructures," Phys. Rev. Lett. **95**, 086604 (2005).

[17] A. N. Chantis, K. D. Belashchenko, E. Y. Tsymbal, and M. van Schilfgaarde, "Tunneling Anisotropic Magnetoresistance Driven by Resonant Surface States: First-Principles Calculations on an Fe(001) Surface," Phys. Rev. Lett. **98**, 046601 (2007).

[18] A. B. Shick, F. Maca, J. Masek, and T. Jungwirth, "Prospect for room temperature tunneling anisotropic magnetoresistance effect: Density of states anisotropies in CoPt systems," Phys. Rev. B **73**, 024418 (2006).

[19] R. C. Jaklevic and J. Lambe, "Molecular Vibration Spectra by Electron Tunneling," Phys. Rev. Lett. **17**, 1139 (1966).

[20] J. S. Moodera, J. Nowak, and R. J. M. van de Veerdonk, "Interface Magnetism and Spin Wave Scattering in Ferromagnet-Insulator-Ferromagnet Tunnel Junctions," Phys. Rev. Lett. **80**, 2941 (1998).

[21] J. G. Simmons, "Generalized Formula for the Electric Tunnel Effect between Similar Electrodes Separated by a Thin Insulating Film," J. Appl. Phys. **34**, 1793 (1963).

[22] Y. Ando, T. Miyakoshi, M. Oogane, T. Miyazaki, H. Kubota, K. Ando, and S. Yuasa, "Spin-dependent tunneling spectroscopy in single-crystal Fe/MgO/Fe tunnel junctions," Appl. Phys. Lett. **87**, 142502 (2005).

[23] J. A. Stroscio, D. T. Pierce, A. Davies, R. J. Celotta, and M. Weinert, "Tunneling Spectroscopy of bcc (001) Surface States," Phys. Rev. Lett. **75**, 2960 (1995).

[24] C. Tiusan, J. Faure-Vincent, C. Bellouard, M. Hehn, E. Jouguelet, and A. Schuhl, "Interfacial Resonance State Probed by Spin-Polarized Tunneling in Epitaxial Fe/MgO/Fe Tunnel Junctions," Phys. Rev. Lett. **93**, 106602 (2004).

[25] P. Mavropoulos, N. Papanikolaou, and P. H. Dederichs, "Complex Band Structure and Tunneling through Ferromagnet /Insulator /Ferromagnet Junctions," Phys. Rev. Lett. **85**, 1088 (2000).

[26] T. Nagahama, S. Yuasa, E. Tamura, and Y. Suzuki, "Spin-Dependent Tunneling in Magnetic Tunnel Junctions with a Layered Antiferromagnetic Cr(001) Spacer: Role of Band Structure and Interface Scattering," Phys. Rev. Lett. **95**, 086602 (2005).

[27] H. Zabel, "Magnetism of chromium at surfaces, at interfaces and in thin films," J. Phys. C: Condens. Matter **11**, 9303 (1999).

Chapter 5

SPIN TRANSFER TORQUE INDUCED MICROWAVE EMISSION FROM MgO BASED TUNNEL JUNCTIONS

5.1 INTRODUCTION

When a *dc* spin-polarized current flows through a thin ferromagnetic layer, due to the spin-transfer torque (STT) effect, it exerts a torque on the local moments[1,2]. STT effects were usually measured in current-perpendicular-to-plane nanopillar samples, as discussed in Chapter 2. In magnetic sandwich structures, such as spin-valves and magnetic tunnel junctions (MTJs), the direction of magnetization of one magnetic layer is fixed either by exchange bias or synthetic antiferromagnetic coupling and is thus called pinned layer (PL); however, the moments in the other electrode of thinner layer can be manipulated via STT, thus it is usually called the free layer (FL). Experimental observations of STT effects include static measurements of the resistance change due to magnetization switching by the spin torque[3-5]. Under certain conditions, STT can induce steady-state precessional excitation modes of the magnetic layer[6-11]. Most importantly, the frequency of these modes changes with the *dc* current, potentially tunable by 1 or 2 orders of magnitude (~1-100 GHz), and can be turned on and off (slew rate) very rapidly (~1-10 ns)[12]. The precession of the free layer moment results in a change in the resistance of the structure. Thus, this unique phenomenon opens the possibility for the development of new classes of radio-frequency (rf) devices, such as frequency-tunable microwave sources and filters. This effect has mostly been studied, to date, in metallic structures. Narrow linewidths Δf have been obtained at low temperature when the FL and PL were at a large angle to each other (Δf=10 MHz at 4.2 K)[13], or the PL consisted of a synthetic antiferromagnet (Δf=3-15 MHz at 150 K)[14]. However, both the resistance and magnetoresistance of spin-valves are small so that the output power is very limited. Power levels of no more than ~1 nW have been observed, which is too small for most practical applications. The recent observation of giant tunneling magnetoresistance (TMR) in MTJs with MgO tunnel barriers[15], which have much higher resistance and TMR than spin-valves, suggests the possibility of correspondingly higher rf power output due to the much larger resistance change in the tunnel junctions during the precession[16-18]. The potential achievement of both narrow bandwidth and high power from the excitations in these MTJs highlights their promising usefulness for controllable microwave generation.

Here, it is demonstrated that high microwave intensity is emitted at room temperature from MgO based MTJs which exhibit TMR values of ~100% and resistance-area products (RA) of ~4~5 $\Omega\times\mu m^2$. The peak amplitude and the peak frequency have a threshold dependence on the *dc* bias voltage. However, it is also found that the spectral features vary significantly from device to device. It is speculated that these variations are due to non-uniform spatial magnetic excitation arising from inhomogeneous current flow through the tunnel barrier.

5.2 SAMPLES AND EXPERIMENTS

The MTJs were deposited on thermally oxidized Si substrates using a combination of ion-beam and magnetron sputtering at ambient temperature. After deposition, the films were annealed at 300 ^oC for 30 minutes in a 1 T in-plane field. Using e-beam lithography, ion milling, and optical lithography as discussed in chapter two, nanopillar devices were patterned into various sizes from 50×100 to 90×270 nm^2 always with an aspect ratio of 1:2 or 1:3. For such small devices, it is crucial to make the tunnel barrier both thin and of high quality, otherwise the device is so resistive that the current density is low and STT effect is significantly reduced. Therefore, a RA of about 1 $\Omega\mu m^2$ is desired. The MTJs are comprised of the following structure, 75 Ta/200 Cu/50 Ta/120 $Ir_{22}Mn_{78}$/6 $Co_{40}Fe_{40}B_{20}$/30 $Co_{70}Fe_{30}$/7 Ru /27 $Co_{70}Fe_{30}$/11 MgO/20 $Co_{40}Fe_{40}B_{20}$/50 Ta/50 Ru, where the numbers are nominal thicknesses in Ångström. The PL, i.e. the bottom electrode below the barrier, is an exchange biased synthetic anti-ferromagnet, and the FL is formed from 2 nm $Co_{40}Fe_{40}B_{20}$. Secondary ion mass spectroscopy was used to monitor the etching process so that milling stops just before IrMn layer; therefore, both the FL and PL are fully patterned. A bottom thin copper layer was used to increase the conductivity. Although dozens of devices from the same wafer were measured, the reported main results are from 80×160 nm^2 elliptical junctions.

The measurement setup has four Helmholtz coils providing an in-plane field up to 1500Oe in any direction. Microwave probes with a bandwidth from *dc* to 40 GHz (GGB Industries PicoProbes GS type) were used to contact the electrodes of each

device. To reduce the microwave emission loss, several special efforts were made during the fabrication process, such as, the bottom electrodes are isolated from each other, the overlap capacitance between the electrodes was minimized by using a single, very small contact finger that extended to the top of the tunnel barrier, and gold contact pads were connected to the MTJ via planar gold contact with negligible resistance. The characteristic impedance, Z_0, of the measured transmission line was 50 Ω. A *dc* bias voltage was applied through a bias tee (5550B Picosecond Pulse Labs), where positive voltage means electrons flow from the PL to the FL which prefers the parallel state. Reversing the voltage and current prefers the anti-parallel state. The rf emission signal was measured using a spectrum analyzer (PSA E4448A Agilent Technologies) and an external low-noise amplifier with a bandwidth of 100 MHz to 18GHz. The microwave emission power will be defined by the voltage spectral density in units of $nV/\sqrt{Hz}$.

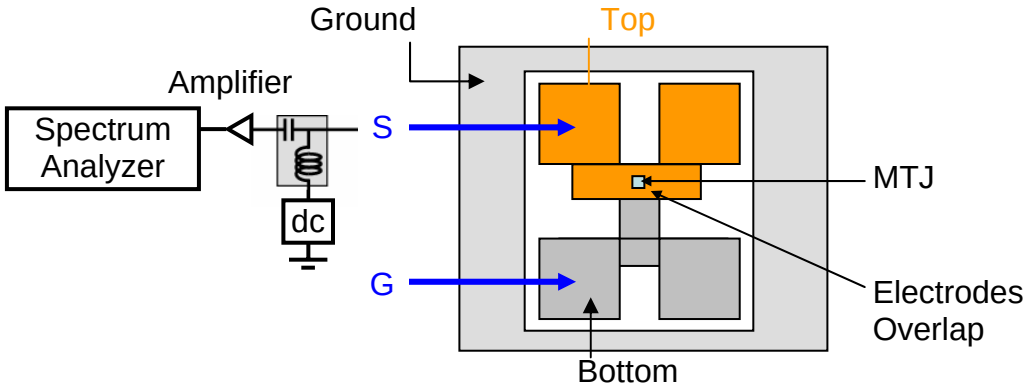

Fig. 5.1 Schematic illustration of the measurement setup for the detection of spin transfer torque induced microware emission.

To approximate the actual microwave emission generated in the MTJs from the detected spectrum in a spectrum analyzer, three issues should be of particular attention. First is the signal loss in the longest transmission line used in the setup, which connects the probes to the bias tee. Using a network analyzer, the transmission coefficient, S_{21}, can be measured up to 40 GHz and is shown in Fig 5.2. Below about 10 GHz, the loss is up to 6-7 dB. Second is the subtraction of environmental noise sources. The subtraction was done by subtracting the noise spectral powers at zero bias from the measured spectrum at each bias voltage. With all the other experimental conditions same, a noise spectrum is measured and recorded at zero bias, and then the desired bias

voltage is applied and another spectrum is measured. Afterwards, the first spectrum is subtracted from the second one, and the result is saved as the spectrum under such experimental conditions. This procedure also removes thermal Johnson noise and the noise from the amplifier. After considering these two factors, the remaining issue is how much microwave emission enters the probes from the MTJs.

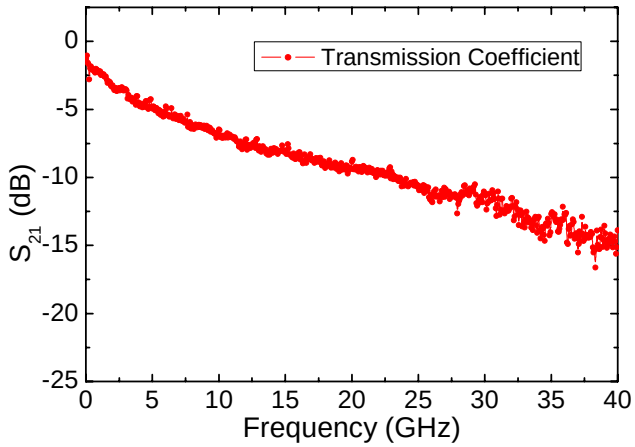

Fig. 5.2 Transmission coefficient of microwave signals at various frequencies in the transmission line used in the setup.

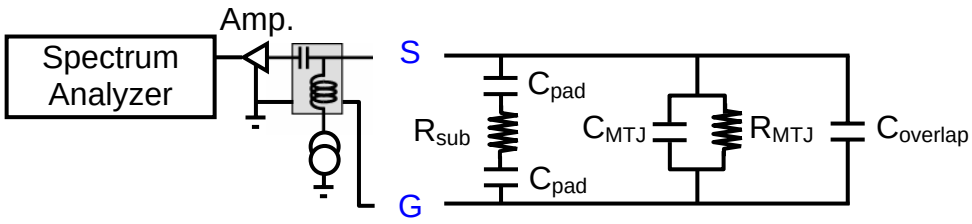

Fig. 5.3 Circuit model of the measurement setup for the detection of spin transfer torque induced microware emission, where R_{sub} is the resistance of Si substrate underneath the electrodes, C_{pad} is the capacitance between electrode and Si substrate, R_{MTJ} is the resistance of MTJ, $C_{overlap}$ is the overlap capacitance between top contact and bottom contact which is minimized by an extended finger.

Due to the impedance mismatch between the probe and the MTJ, it is inevitable that some of the STT induced microwave emission is lost in coupling to the probes. The reduced factor for the input to the probes is mainly determined by the MTJ's resistance and the overlap capacitance of the top and bottom contacts. The circuitry of the measurement setup can be modeled as in Fig. 5.3. Since R_{sub} is very large and the C_{MTJ} is very small due to the tiny size of the nanopillar, they can thus be neglected for

simplicity. Therefore, the relation between the voltage, V_{line}, at the input of the probes and the microwave voltage, V_{MTJ}, at the frequency ω generated at the MTJ can be written as[19],

$$V_{line}(\omega) = V_{MTJ}(\omega)\frac{Z_0}{\sqrt{\left(R_{MTJ}Z_0\omega C_{overlap}\right)^2 + \left(R_{MTJ}+Z_0\right)^2}}$$

where Z_0 is the 50 Ω impedance for transmission line, R_{MTJ} is the resistance of the MTJ, $C_{overlap}$ is the overlap capacitance between top contact and the bottom contact, which is minimized by an extended finger. The overlapping area is about 2×4.5 μm^2, and is filled with ~40nm-thick Al_2O_3, thus $C_{overlap}$ is about 0.018pF. With the MTJ's resistance range from 350-800 Ω, the microwave voltage V_{MTJ} is at least about 10-times larger than the measured voltage, V_{line}. Although the factors causing microwave loss are explained in the current section, the spectrum will not be corrected in the rest of the chapter; i.e. only the total detected power from the spectrum analyzer will be discussed with the environmental noise subtracted and the amplification of ~26 dB corrected.

5.3 EXPERIMENTAL RESULTS

5.3.1 Field and Current Induced Switching

As shown in Fig. 5.4 (a), the resistance when the FL moment is anti-parallel (AP) to the PL moment is almost 111% higher than when these moments are parallel (P). The TMR falls to about half this value at ~±0.50 V, mainly due to a drop in the resistance of the AP state (whereas the resistance of the P state hardly changes). In the nano-pillar studied, the free layer moment is subjected to an ~53 Oe magnetostatic coupling field from the PL, seen as an asymmetry in the resistance versus field hysteresis loop. When this offset field is compensated by an external field of approximately the same magnitude, clear current-induced-switching is found as illustrated in Fig. 5.4 (b). The switching occurs at approximately +0.30 and -0.38 V, corresponding to current densities of 3.7 and 8.0×10^6 A/cm^2 flowing through the junction, respectively, for the AP to P

and P to AP transitions. In much larger fields, no such switching is observed (for |V| < ±0.50 V).

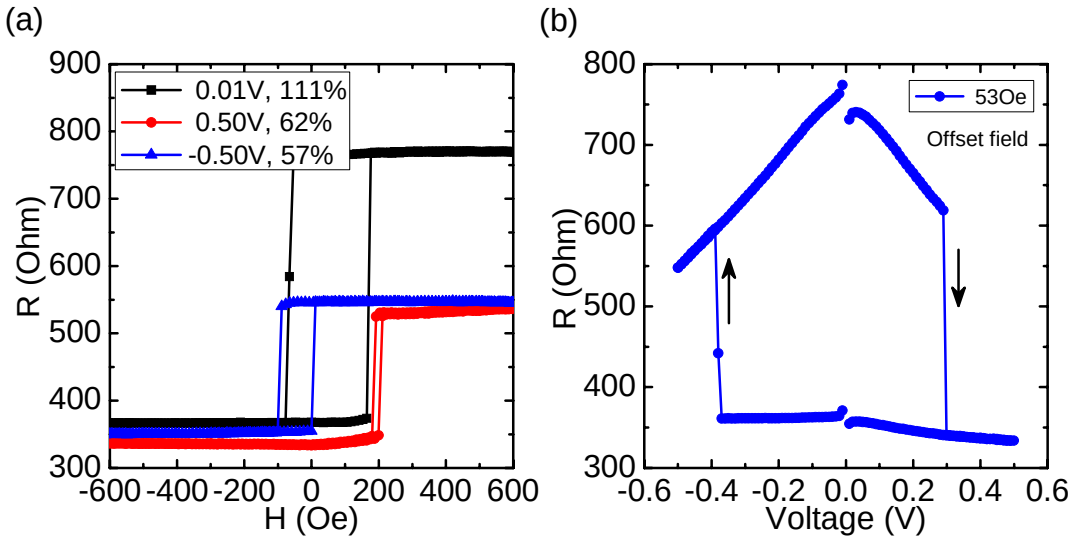

Fig 5.4 (a) R vs. H at bias voltages of 0.01, 0.50, and -0.50 V; (b) R vs. V in a field of 530 Oe. Positive voltage corresponds to electrons flowing from pinned layer to free layer.

5.3.2 STT Induced Microwave Emission

Background environmental noise was eliminated from the measured spectra by subtracting corresponding measurements at zero bias as discussed before, and the amplification factor of ~26 dB was also subtracted from the recorded raw data by spectrum analyzer. Fig. 5.5 shows some typical spectra corresponding to ±0.5 V with various fields applied along the easy axis. The major dynamic excitations with the most pronounced peaks were observed in the AP (P) states for + (-) voltage, consistent with the expected STT induced excitation of the FL, where + voltage, i.e. electrons flowing from the PL to the FL, stabilizes the P state and de-stabilizes the AP state, and vice versa. Moreover, STT induced microwave emission can also occur at opposite polarity, for example, in magnetic field of -440 Oe the MTJ is in P state; however, at 0.5 V when electrons flowing from PL to FL, a clear peak is observed at a frequency around 3.5 GHz. This dynamic is opposed to the STT effect on the FL, and can only be accounted for by precession of the magnetization of the PL. It is speculated that the synthetic antiferromagnetic coupling in the PL deteriorates when the device is made too small,

even though it works excellently in larger devices. Therefore, the so called PL, is no longer ideally fixed but still harder to switch and process than that of the FL.

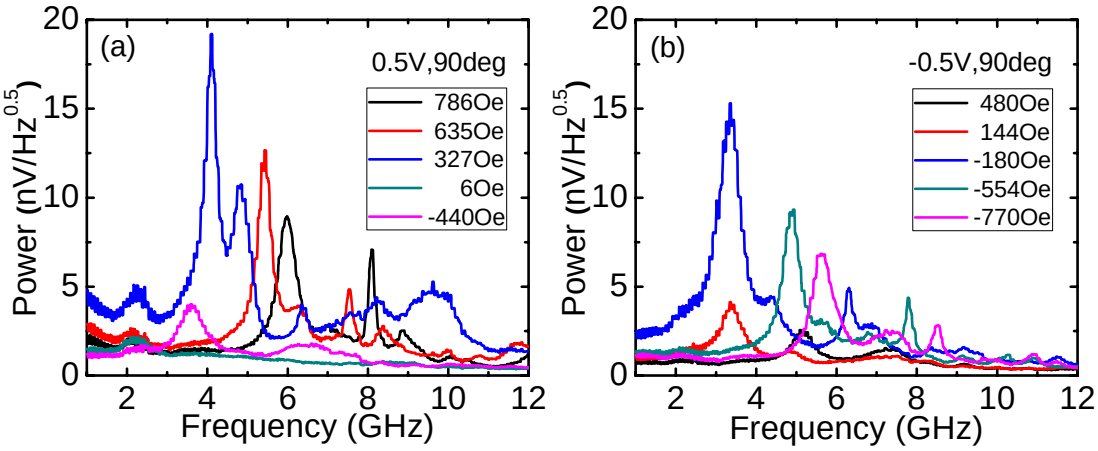

Fig. 5.5 Typical spectra corresponding to ±0.5 V with various fields applied along easy axis. With large positive fields MTJ is in AP state, and with large negative fields in P state as shown by magnetoresistance loop.

Several other striking characteristics can be clearly seen from Fig. 5.5, e.g. there usually exist multiple complex peaks, and bandwidths of these peaks are generally broad. For the highest peak at -0.5 V with a field -180 Oe, the full width at half maximum (FWHM) is about 0.71 GHz. The lowest power level for all the curves is about 0.5 $nV/Hz^{0.5}$ and can be considered as the intrinsic noise of the MTJ which includes magnetic and shot noise contributions. The spectrum can be nicely shown in a contour plot as in Fig. 5.6. Clear emissions occur in the AP state at 0.5 V and in the P state at -0.5 V, which means that they derive from the STT induced precession in the FL. Besides these strong emissions, though weak, there still exist other FL generated emissions. In the opposite polarity, additional weak emissions due to the precession of PL are also noticeable at 0.5 V for P state and -0.5 V for AP state.

By fitting each spectral trace with multiple Lorentzian functions, the peak frequency f, the FWHM linewidth Δf, and the integrated power P of each excitation mode can be derived. Fig 5.7 shows the field dependence of the peak frequency and FWHM at 0.50 V and -0.5 V. In the case of the AP state, two excitation modes are clearly observed and analyzed from the contour plot Fig. 5.6. At constant voltage, all

the peaks' frequency f and FWHM linewidth Δf are tunable with H for both P and AP states. Frequency, f, increases with H according to the Kittel formula[20],

$$f = \frac{\gamma}{2\pi}\sqrt{(H + H_k)(H + H_k + 4\pi M_s)}$$

where γ is the gyromagnetic ratio, H_k the anisotropic field, M_s the magnetization.

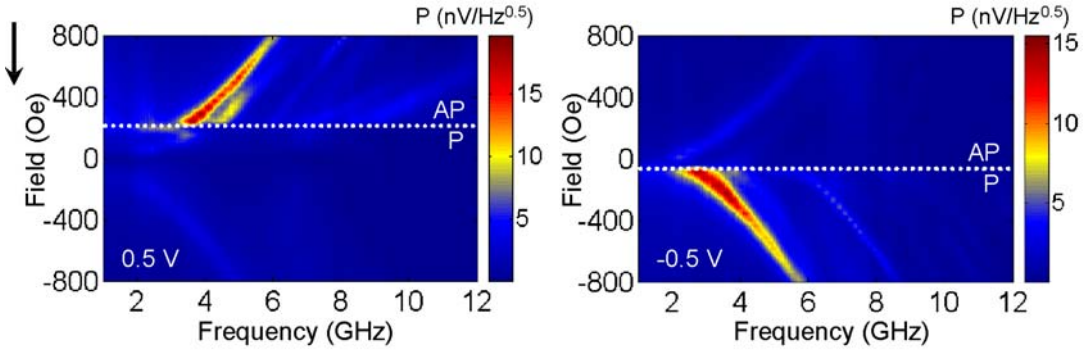

Fig. 5.6 Contour plots of spectra corresponding to ±0.5 V with various fields applied along easy axis. Dotted white lines divide the plots into P and AP state. Black downward arrow on right shows the field sweeping direction. Colorbar shows microwave power level in the unit of nV/Hz$^{0.5}$.

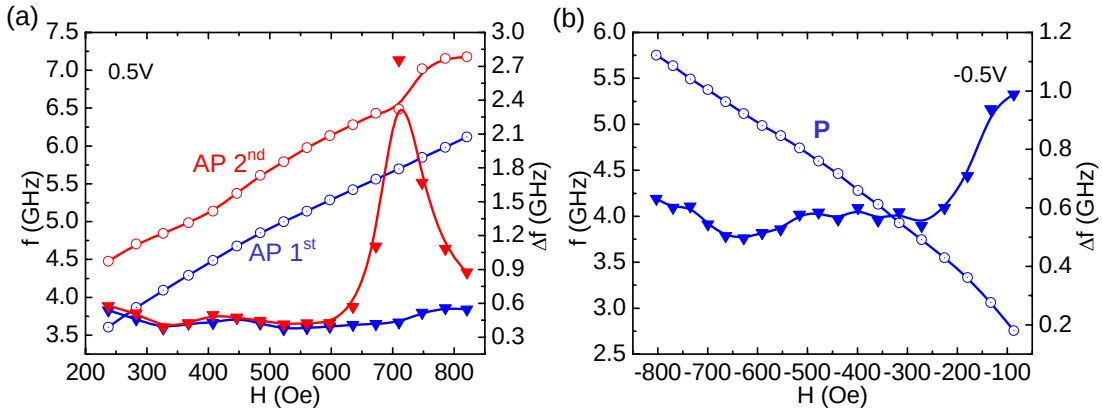

Fig 5.7 Field dependence of peak frequency (open circle) and FWHM (solid triangle) at (a) 0.50 V and (b) -0.5 V.

However, the best fitting results with the Kittel equation always give much smaller values of $4\pi M_s$ than that in bulk $Co_{40}Fe_{40}B_{20}$, which is about 12 kOe. For example, fitting to the peak AP 1st and P give a $4\pi M_s$ of 4.0 kOe and 3.2 kOe respectively. The linewidth of the lower frequency mode (AP 1st) does not change much with field. By contrast, the higher frequency mode (AP 2nd) only shows weak dependence of the linewidth in the low field regime. It becomes much broader in a field around 700 Oe

and the linewidth turns narrower again in the even higher field regime. For the excitation mode in the P state, the linewidth is quite similar to that in AP 1st when the field is larger than 200 Oe and it becomes much larger in a smaller field.

Fig. 5.8 shows the frequency f, FWHM linewidth Δf, and integrated power P as a function of the bias voltage for the two excitation modes in the anti-parallel state with a magnetic field of 236 Oe applied along the easy axis. From the voltage dependence of power (Fig. 5.8(c)), the microwave emission is small when the bias voltage is low. With increasing voltage, once above a threshold voltage around 0.3 V, the emission power starts increasing dramatically. Finally a total power of about 3 nW can be easily obtained even under modest bias conditions. The direction of the field is crucial to the peak's intensity, and a 10° field deviation around easy axis can increase the emission power by a factor of 10, but this does not mean that more deviation always results in larger emission although the largest emission does usually occur when the field is applied along hard axis so that the cone angle of the precession is maximized, thus giving rise to maximal resistance change in the device. Therefore, total power that is delivered to a 50 Ω load can be as high as ~30 nW.

The bias dependence of the emission frequency (Fig. 5.8(a)) shows that the frequency remains almost constant when the voltage is below the threshold value and starts to decrease when the voltage exceeds the threshold, which demonstrates that the frequency of the oscillator can be tuned only by an electrical voltage. The analysis of f versus bias voltage confirms that the microwave emission peaks in Fig. 5.6(a) are indeed steady state excitations above the critical threshold voltage and not thermally excited ferromagnetic resonance modes (T-FMR). According to theory[21,22] and experiment[14], the transition from T-FMR to steady state in-plane precession (IPP) can be inferred from the evolution of the frequency f, linewidth Δf, and the output power P of the microwave emission as a function of increasing bias voltage. The frequency of the T-FMR mode is expected to change little at small voltages, but decrease moderately near the critical voltage V_c, consistent with the spin-wave theory[10,23] and the macrospin simulations[24]. This red-shift in frequency with bias voltage is a characteristic of an IPP mode where the magnetization precesses around the sub-threshold static equilibrium position[21,22]. If the device is driven harder by bias

voltage and the excitation becomes an out-of-pane precession (OPP) mode, a blue-shift in frequency should be observed. To obtain the predicted blue-shift, in-plane-magnetization MTJs with lower threshold voltage and higher breakdown voltage are needed so that the OPP can occur before the MTJs break down; or alternatively, materials with perpendicular anisotropy must be used as the FL to make the magnetization in the free layer directly out-of-plane.

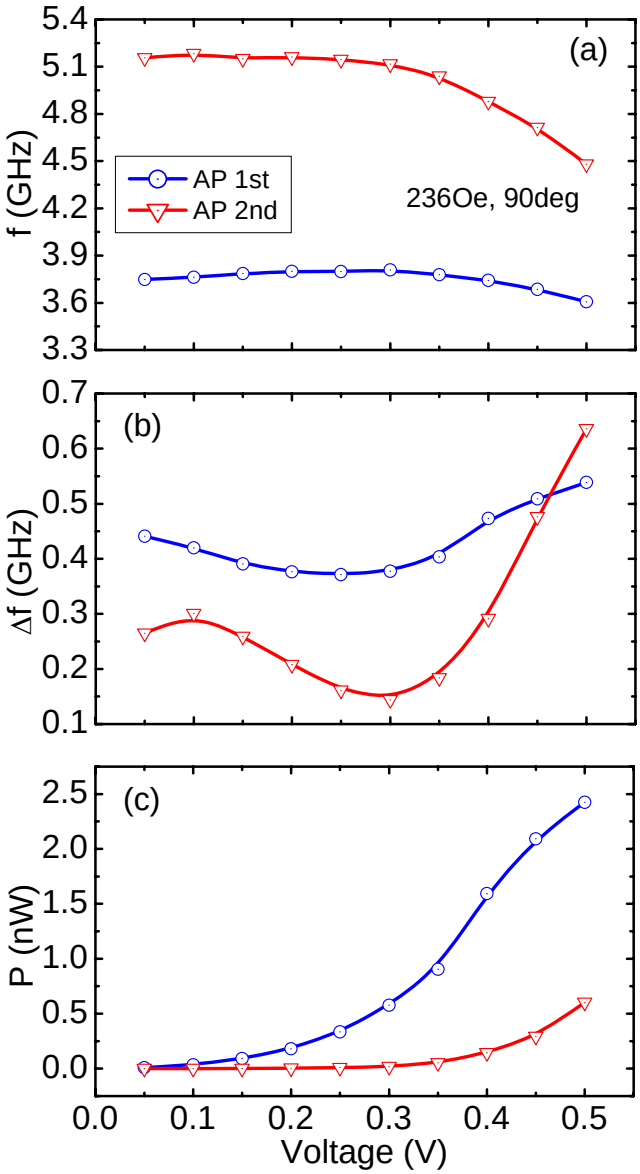

Fig. 5.8 (a) Frequency f, (b) FWHM linewidth Δf, and (c) integrated power P versus bias voltage for the two excitation modes in antiparallel state with a magnetic field of 236 Oe applied along easy axis.

By contrast, linewidth Δf versus bias voltage shows a minimum, and the occurrence of the minimum is accompanied by an abrupt increase in power and a decrease in f, as observed in Fig. 5.8. For the AP 1st mode, a relatively broad linewidth of ~0.45 GHz is observed. The linewidth then narrows as the voltage in increased and reaches a minimum at about 0.3 V, the same as determined from the current-induced-switching in Fig. 5.4. As the voltage is increased further past this minimum point, a dramatic broadening in the linewidth is seen. This characteristic is more pronounced in the AP 2nd mode than that in AP 1st mode (Fig. 5.8(b)). The initial narrowing in linewidth can be understood from stochastic arguments. Below threshold, the dynamical state is dominated by amplitude and phase fluctuations due to thermal noise, which results in the broad spectral traces observed. As the current is increased, the amplitude of precession increases and, as a consequence, the trajectories become more immune to amplitude fluctuations which scale with temperature and not amplitude. In the limit of large amplitude motion, in which only phase noise contributes, the spectral linewidth can be estimated from stochastic spin-wave theory[24]. For the linewidth broadening past the linewidth minimum, it is speculated to result from higher-order nonlinear effects[14].

5.3.3 Sensitive Spectrum

Obtaining a nice microwave spectrum is nontrivial, and it is found that the spectrum can vary dramatically from device to device, even for some identical-looking tunnel junctions. For example, Fig. 5.9 shows both the field and current induced switching for two devices, which are nominally same in both size and structure, and furthermore, they are also close to each other on the same wafer. From these static measurements, the behavior of both devices is almost identical: very similar resistance, TMR, coercivity H_c, dipolar coupling, and even very close threshold voltage for current induced switching. By contrast, their microwave emission spectra are distinctly different. For Device II, a clear STT induced excitation is seen, though it only manifests itself near the boundary between P and AP state where the FL becomes most easily excited by spin-torque with the assistance of the applied field. However, for Device I, no such clear

and nice microwave emission is detected, except some low frequency noise and some non-coherent excitations with very broad linewidth at the AP/P state boundary which might come from STT amplified magnetic noises at this critical point of field switching. Therefore, there exist some non-obvious factors which can strongly influence microwave emission, but field and current switching are not very much sensitive to. The significant influence of the barrier roughness on the microwave emission has been directly investigated using transmission electron microscopy (TEM). Two nominal identical wafers with same multilayered structure are fabricated under same conditions. However, from spectrum measurement, it turned out that the yield of obtaining clear STT induced emission from one sample is far lower that the other one. TEM was carried out on two typical devices, each on one wafer, using focused ion beam to cross-section the active MTJs. The images show that the tunneling barrier of the sample with low yield is much rougher than that of the other sample with high yield.

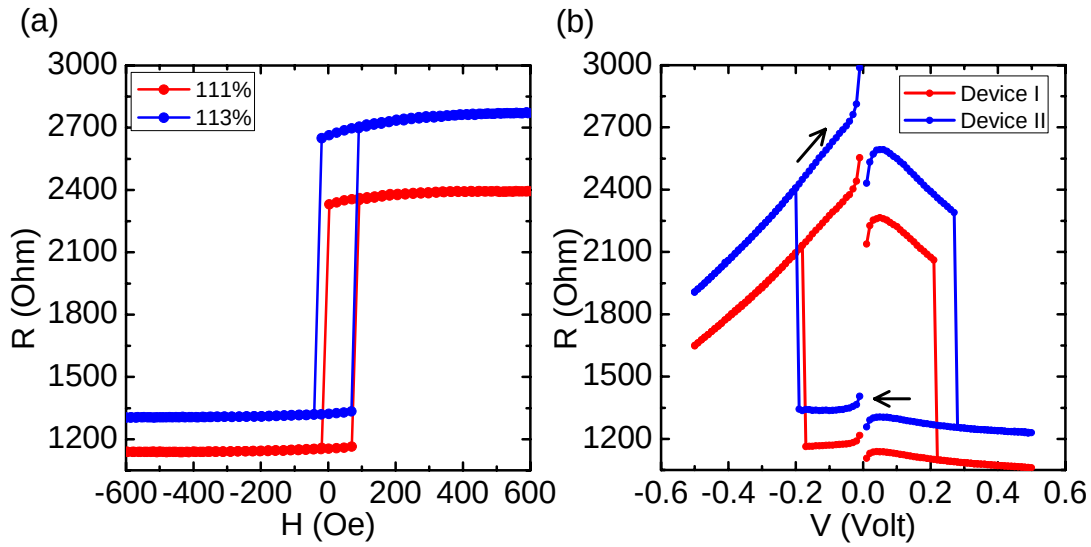

Fig 5.9 (a) Field switching and (b) current induced switching of two nominally identical devices. Magnetoresistance loops are measured at 0.01 V, and voltage switching loops are obtained with magnetic fields applied to cancel the dipolar coupling, or the offset field in (a), respectively. Red (blue) curves are for Device I (II).

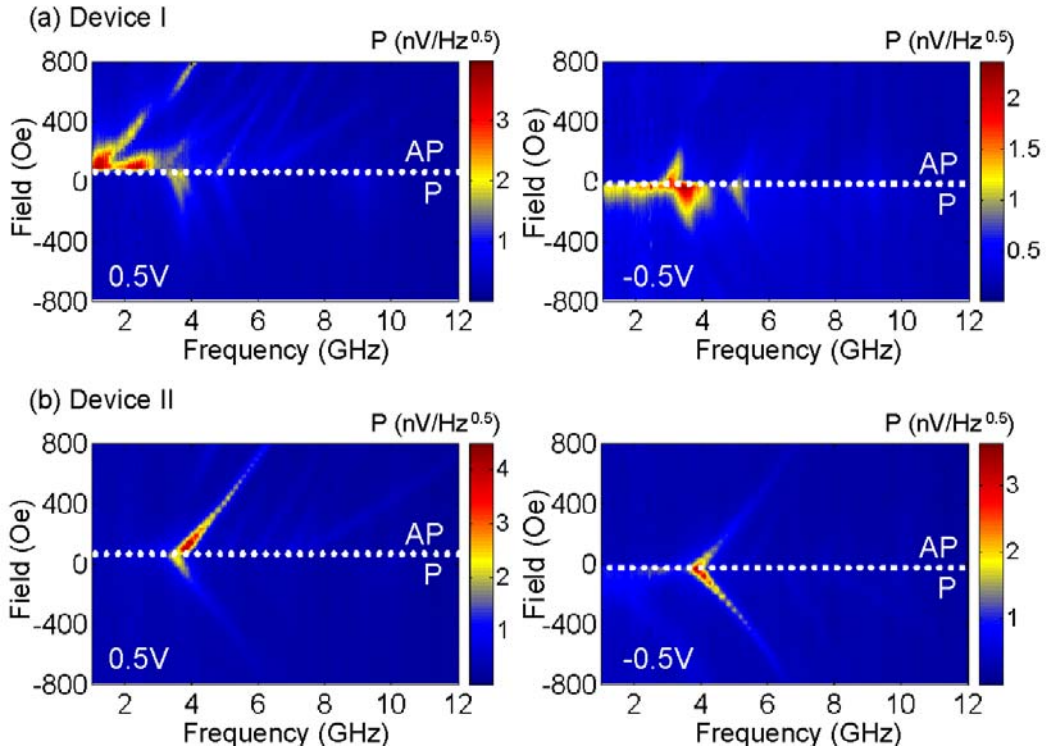

Fig 5.10 Microwave emission spectra for Device I (a) and II (b) at ±0.5 V with various fields applied along easy axis. Dotted white lines divide plots into P and AP state. Colorbar shows microwave power level in the unit of nV/Hz$^{0.5}$. Field sweeping direction is always from positive from negative.

The effect of dipolar coupling from the synthetic antiferromagnetic layers on the free layer was also studied in TMR, coercivity H_c, and offset field in the magnetoresistance loop. Three samples with identical structure were fabricated under the same conditions, except that the etching time for the bottom electrode is different for each. Using secondary ion mass spectroscopy, the milled materials can be detected, i.e. it can define which layer is being etched. Once the Co and Mn signals cross over, it means all the synthetic antiferromagnetic layers are etched away. By over-etching, it mills into the IrMn exchange layer, and more importantly, it removes the long sidewall tail of CoFe in synthetic antiferromagnetic layers, thus reducing the dipolar coupling to FL. As shown in Fig. 5.11, the offset field from this coupling shows a trend of slight decrease with increasing over-etching time. However, the microwave spectrum variations among the devices on these three different types of samples are all severe. Therefore, the sensitivity of the STT induced precession is not from the effect of the dipolar coupling between FL and PL.

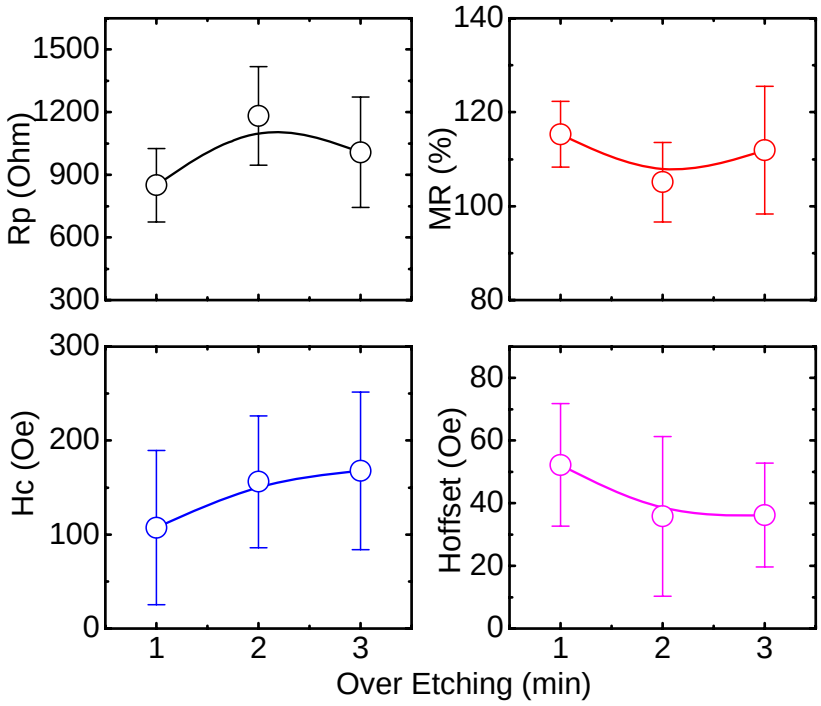

Fig. 5.11 The influence of the over-etching time after Co/Mn crossover in secondary ion mass spectroscopy (SIMS) on resistance R_P, TMR, coercivity H_c, and dipolar coupling field H_{offset}.

5.4 DISCUSSION AND COMMENT

It has been demonstrated that current induced precessional excitations can produce microwaves with power levels one to two orders of magnitude higher than in spin-valve structures. The observation of much higher rf power emission from state of the art MTJs is of high technological interest. Moreover, clear evidence has been found for the STT induced excitation modes whose frequency, linewidth and power vary substantially with applied field and bias voltage. The detailed control and understanding of the frequency, linewidth and emission power is critical. In particular, it is important to identify the factors which broaden the linewidth in MTJs, whether external, i.e. thermal, or intrinsic.

From the experimental observations, the nature of the broad linewidth can be hypothesized and a few comments will be discussed. In all these small nanopillar samples, to control the resistance in a desirable low regime, the tunneling barriers have to be very thin, only of about 1 nm thick. Roughness is inevitable in such ultrathin tunnel barriers. In such a thin barrier, even a weak nonuniformity in barrier thickness would cause strong local variations of the current density across the sample, which could reduce the coherence of the magnetization dynamics and lead to a nonhomogeneous excitation mode profile. The frequency of such a nonhomogeneous mode differs then from a homogeneously excited mode, due to different dipolar and exchange contributions[25]. Therefore, broad linewidth develops in the microwave emission spectrum. The low magnetization values from the frequency fitting with field could possibly be due to the nonhomogeneous excitations, which can not be well accounted for by Kittel equation[23,26]. Studies in micromagnetic simulations might reveal some more details about the nature of the linewidth broadening in these high TMR samples. The complex physical processes behind this behavior are worthy of further investigation. Despite of all the challenges, the experimental results clearly demonstrate the high potential of MgO based MTJs as nano-oscillators for tunable rf emission.

REFERENCES:

[1] L. Berger, "Emission of spin waves by a magnetic multilayer traversed by a current," Phys. Rev. B **54** (13), 9353 (1996).

[2] J. C. Slonczewski, "Current-driven excitation of magnetic multilayers," J. Magn. Magn. Mater. **159**, L1-L7 (1996).

[3] J. A. Katine, F. J. Albert, R. A. Buhrman, E. B. Myers, and D. C. Ralph, "Current-Driven Magnetization Reversal and Spin-Wave Excitations in Co/Cu/Co Pillars," Phys. Rev. Lett. **84** (14), 3149-3152 (2000).

[4] J. Hayakawa, S. Ikeda, Y. M. Lee, R. SasaKi, T. Meguro, F. Matsukura, H. Takahashi, and H. Ohno, "Current-Driven Magnetization Switching in CoFeB/MgO/CoFeB Magnetic Tunnel Junctions," Jpn. J. Appl. Phys. **44** (41), L1267-L1270 (2005).

[5] H. Kubota, A. Fukushima, Y. Ootani, S. Yuasa, K. Ando, H. Maehara, K. Tsunekawa, D. D. Djayaprawira, N. Watanabe, and Y. Suzuki, "Evaluation of Spin-Transfer Switching in CoFeB/MgO/CoFeB Magnetic Tunnel Junctions," Jpn. J. Appl. Phys. **44** (40), L1237-L1240 (2005).

[6] G. Bertotti, C. Serpico, I. D. Mayergoyz, A. Magni, M. d'Aquino, and R. Bonin, "Magnetization Switching and Microwave Oscillations in Nanomagnets Driven by Spin-Polarized Currents," Phys. Rev. Lett. **94**, 127206- (2005).

[7] O. Boulle, V. Cros, J. Grollier, L. G. Pereira, C. Deranlot, F. Petroff, G. Faini, J. Barnas, and A. Fert, "Shaped angular dependence of the spin-transfer torque and microwave generation without magnetic field," Nat. Phys. **3**, 492 (2007).

[8] S. Kaka, M. R. Pufall, W. H. Rippard, T. J. Silva, S. E. Russek, and J. A. Katine, "Mutual phase-locking of microwave spin torque nano-oscillators," Nature **437**, 389 (2005).

[9] S. I. Kiselev, J. C. Sankey, I. N. Krivorotov, N. C. Emley, R. J. Schoelkopf, R. A. Buhrman, and D. C. Ralph, "Microwave oscillations of a nanomagnet driven by a spin-polarized current," Nature **425**, 380 (2003).

[10] S. M. Rezende, F. M. de Aguiar, R. L. Rodriguez-Suarez, and A. Azevedo, "Mode Locking of Spin Waves Excited by Direct Currents in Microwave Nano-oscillators," Phys. Rev. Lett. **98**, 087202 (2007).

[11] M. Tsoi, A. G. M. Jansen, J. Bass, W.-C. Chiang, V. Tsoi, and P. Wyder, "Generation and detection of phase-coherent current-driven magnons in magnetic multilayers," Nature **406**, 46 (2000).

[12] I. N. Krivorotov, N. C. Emley, J. C. Sankey, S. I. Kiselev, D. C. Ralph, and R. A. Buhrman, "Time-Domain Measurements of Nanomagnet Dynamics Driven by Spin-Transfer Torques," Science **307**, 228 (2005).

[13] I. N. Krivorotov, D. V. Berkov, N. L. Gorn, N. C. Emley, J. C. Sankey, D. C. Ralph, and R. A. Buhrman, "Large-amplitude coherent spin waves excited by spin-polarized current in nanoscale spin valves," Phys. Rev. B **76**, 024418 (2007).

[14] Q. Mistral, J.-V. Kim, T. Devolder, P. Crozat, C. Chappert, J. A. Katine, M. J. Carey, and K. Ito, "Current-driven microwave oscillations in current perpendicular-to-plane spin-valve nanopillars," Appl. Phys. Lett. **88**, 192507 (2006).

[15] S. S. P. Parkin, C. Kaiser, A. F. Panchula, P. Rice, M. G. Samant, S.-H. Yang, and B. Hughes, "Giant tunneling magnetoresistance at room temperature with MgO (100) tunnel barriers," Nature Materials **3**, 862 (2004).

[16] A. M. Deac, A. Fukushima, H. Kubota, H. Maehara, Y. Suzuki, S. Yuasa, Y. Nagamine, K. Tsunekawa, D. D. Djayaprawira, and N. Watanabe, "Bias-driven high-power microwave emission from MgO-based tunnel magnetoresistance devices," Nat. Phys. **4**, 803 (2008).

[17] D. Houssameddine, U. Ebels, B. Delaet, B. Rodmacq, I. Firastrau, F. Ponthenier, M. Brunet, C. Thirion, J. P. Michel, L. Prejbeanu-Buda, M. C. Cyrille, O. Redon, and B. Dieny, "Spin-torque oscillator using a perpendicular polarizer and a planar free layer," Nat. Mater. **6**, 447 (2007).

[18] A. V. Nazarov, H. M. Olson, H. Cho, K. Nikolaev, Z. Gao, S. Stokes, and B. B. Pant, "Spin transfer stimulated microwave emission in MgO magnetic tunnel junctions," Appl. Phys. Lett. **88**, 162504 (2006).

[19] A. V. Nazarov, K. Nikolaev, Z. Gao, H. Cho, and D. Song, "Microwave generation in MgO magnetic tunnel junctions due to spin transfer effects (invited)," J. Appl. Phys. **103**, 07A503 (2008).

[20] C. Kittel, "Introduction to Solid State Physics," (John Wiley & Sons, 2005).

[21] J.-V. Kim, Q. Mistral, C. Chappert, V. S. Tiberkevich, and A. N. Slavin, "Line Shape Distortion in a Nonlinear Auto-Oscillator Near Generation Threshold: Application to Spin-Torque Nano-Oscillators," Phys. Rev. Lett. **100**, 167201 (2008).

[22] V. Tiberkevich, A. Slavin, and J.-V. Kim, "Microwave power generated by a spin-torque oscillator in the presence of noise," Appl. Phys. Lett. **91**, 192506 (2007).

[23] A. N. Slavin and P. Kabos, "Approximate theory of microwave generation in a current-driven magnetic nanocontact magnetized in an arbitrary direction," IEEE Trans. Magn. **41**, 1264 (2005).

[24] J.-V. Kim, "Stochastic theory of spin-transfer oscillator linewidths," Phys. Rev. B **73**, 174412 (2006).

[25] B. A. Kalinikos and A. N. Slavin, "Theory of dipole-exchange spin wave spectrum for ferromagnetic films with mixed exchange boundary conditions," J. Phys. C **19**, 7013 (1986).

[26] K.-J. Lee, A. Deac, O. Redon, J.-P. Nozieres, and B. Dieny, "Excitations of incoherent spin-waves due to spin-transfer torque," Nat. Mater. **3**, 877 (2004).

Chapter 6

CONCLUSIONS AND SUGGESTIONS FOR FURTHER RESEARCH

6.1 CONCLUSIONS

The research performed in this dissertation was aimed at deepening the understanding of spin polarized current phenomena in magnetic tunnel junctions, with emphasis on both tunneling magnetoresistance and spin-transfer torque effect. Increased tunneling magnetoresistance from amorphous CoFe was studied. Cross-section transmission electron microscopy revealed that films of CoFe alloys, sandwiched between two conventional amorphous materials, undergo an amorphous-to-crystalline transition at a critical thickness of ~25-30 Å. With these thin amorphous layers as an electrode in Al_2O_3 magnetic tunnel junctions, significant enhancement in tunneling magnetoresistance and tunneling spin polarization was found compared to when crystalline layers were used. To understand this phenomenon, both x-ray emission spectroscopy and *ab initio* calculations were carried out to investigate the electronic structures of both amorphous and crystalline CoFe. Although calculation results of crystalline and amorphous forms of *bulk* CoFe alloys show substantial differences in their band structures, the calculated spin polarization at the Fermi energy is reduced for amorphous, contrary to an explanation of the experimental observation in terms of the bulk electronic states. From the calculations, it is also found that the spin moment of the Fe element is more sensitive to its local chemical and structural environment. Indeed, x-ray emission spectroscopy shows a significant increase in the Fe, but not the Co, 3*d* density of states at the Fermi energy for thin amorphous CoFe layers. Therefore, it is reasonable to postulate that the increased tunneling magnetoresistance is likely due to changes in electronic structure and interfacial bonding at the Al_2O_3/CoFe interface caused by amorphization induced atomic relaxation.

The tunneling anisotropic magnetoresistance of MgO and Al_2O_3 tunnel junctions with *3d* transition metal alloys was investigated. Despite the small effect due to weak spin-orbit coupling in these systems, complex dependences of the junction resistance on the bias voltage and angle were found, which are distinctly different for MgO and Al_2O_3 tunnel barriers. A tight-binding model suggests that the tunneling anisotropic effect derives from the anisotropy in the interface density of states of the majority band due to mixing with a resonant state via spin-orbit coupling. Moreover, a puzzling reversal in

tunneling anisotropic magnetoresistance effect from CrMo has also been observed. Further work will be required to investigate and understand this effect from an antiferromagnetic material.

Besides the studies in tunneling magnetoresistance effect, spin transfer torque induced microwave emission from magnetic tunnel junctions has been explored. It is shown that, compared to spin-valves, much higher microwave power is emitted from nano-fabricated tunnel junctions with MgO tunnel barriers which exhibit high tunneling magnetoresistance at low resistance-area values. However, accompanied with the increased power, it is also found that the linewidth of the emission is usually large, and the spectral features vary sensitively from device to device. Preliminary investigations suggest that both the broad linewidth and the variations in the spectrum are possibly due to non-uniform spatial magnetic excitation arising from inhomogeneous current flow through the tunnel barrier, since the barrier is so thin that any film roughness would cause severe variation in the local resistance and current flow.

The results discussed in this dissertation are of importance in both physics and technology. The studies in the tunneling magnetoresistance deepen the understanding of the complicated spin dependent tunneling process in magnetic tunnel junctions, and the research in spin transfer torque has the potential to be relevant for device applications such as STT-RAM and rf nano-oscillator. Spintronic devices using magnetic tunnel junctions have been successfully incorporated in recording read heads, thus continuing to dramtically lower the price and increase the storage capacity of hard disk drives. The 16Mbit MRAM has been released to the market and a 32Mbit STT-RAM has just been demonstrated and its commercial availability seems imminent. Beyond these, innovative Racetrack Memory has been proposed and is being researched to use spin polarized currents to move magnetic domains along a nanowire, where as current is passed through the domains pass by magnetic read/write heads positioned near the wire so that patterns of bits can be read or written. If it is developed successfully, Racetrack Memory would offer storage density higher than comparable solid-state memory devices like Flash RAM and similar to conventional disk drives, but with much higher read/write performance. All these promising prospects make it,

together with MRAM and STT-RAM, one of a number of new technologies vying to become a universal memory in the future.

6.2 SUGGESTIONS FOR FURTHER RESEARCH

Some unresolved issues in this dissertation are worthy of further investigations. For example, large tunneling anisotropic magnetoresistance is desirable at room temperature for potential applications in information storage and field sensing, especially when only a single ferromagnetic layer is present. To achieve this, materials with strong spin-orbit coupling, e.g. Co/Pt multilayers, should be explored. In Cr based systems, where spin density waves play a very important role in their transport properties, correlating the tunneling anisotropic magnetoresistance with the spin density wave will be an interesting experimental topic. In the area of spin transfer torque, there remain many exploratory topics that are still unresolved. Lowering the critical current density to switch the free layer is of immediate and critical importance, and many materials with perpendicular magnetic anisotropy are being studied. A clever design of the device structure with the commonly used materials may also be a solution. Further increase in the rf emission power is desired, and a complete understanding of the broad emission linewidth is both scientifically and technologically critical to this research field.

Besides the above, many other topics are of great interest. Successful demonstration of spin logic devices will enrich the applications of spintronics. Nonlocal lateral devices and three terminal devices could open a new door to integrate spintronics with conventional CMOS technology. Electrical field control of magnetism is certainly very attractive, such as in multiferroic materials that are both ferroelectric and magnetic. The combination of spintronics with exotic oxides is quite challenging, but extremely stimulating. Research on these topics will establish fundamentally new approaches to understand and control the wealth of electronic, spin, and collective mode excitations associated with complex oxide interfaces.

APPENDIX: LIST OF ACRONYMS

AF (FM)	Antiferromagnetic (Ferromagnetic)
AFM	Atomic Force Microscopy
AP (P)	Antiparallel (Parallel)
CFB	CoFeB Alloy
CFB10	$Co_{63}Fe_{27}B_{10}$
CFB20	$Co_{40}Fe_{40}B_{20}$
CFB30	$Co_{49}Fe_{21}B_{30}$
DOS	Density of States
EELS	Electron Energy Loss Spectroscopy
FL (PL)	Free (Pinned) Layer
FM (AF)	Ferromagnetic (Antiferromagnetic)
FMR	Ferromagnetic Resonance
FWHM	Full Width at Half Maximum
GGA	Generalized Gradient Approximation
GMR	Giant Magnetoresistance
IBD	Ion Beam Deposition
IETS	Inelastic Electron Tunneling Spectroscopy
IPP (OPP)	In-Plane (Out-of-Plane) Procession
LLG	Landau-Lifshitz-Gilbert
MD	Molecular Dynamics
MRAM	Magnetic Random Access Memory
MTJ	Magnetic Tunnel Junction
NMP	N-Methyl-2-Pyrrolidone
NXES	Non-resonant X-ray Emission Spectroscopy
OPP (IPP)	Out-of-Plane (In-Plane) Procession
P (AP)	Parallel (Antiparallel)
PL (FL)	Pinned (Free) Layer
RA	Resistance-Area Product
RBS	Rutherford Backscattering Spectroscopy

RF	Radio-Frequency
RIXS	Resonant Inelastic X-ray Emission Spectroscopy
SCF	Sandwiched CoFe Layer
SEM	Scanning Electron Microscopy
SIMS	Secondary Ion Mass Spectrometry
SOC	Spin Orbit Coupling
SQUID	Superconducting Quantum Interference Device
STS	Superconducting Tunneling Spectroscopy
STT	Spin Transfer Torque
TAMR	Tunneling Anisotropic Magnetoresistance
TEM	Transmission Electron Microscopy
T-FMR	Thermally Excited Ferromagnetic Resonance
TM	Transition Metal
TMR	Tunneling Magnetoresistance
TSP	Tunneling Spin Polarization
VASP	Vienna Ab-initio Simulation Package
VSM	Vibrating Sample Magnetometry
XES	X-ray Emission Spectroscopy
XPS	X-ray Photoelectron Spectroscopy
XRD	X-ray Diffraction